

SPECTRAL RESPONSE MODELLING AND ANALYSIS OF HETEROJUNCTION BIPOLAR PHOTOTRANSISTORS

A thesis submitted to the University of Manchester for the degree of
Doctor of Philosophy
in the Faculty of Engineering and Physical Sciences

2010

HASSAN ABBAS KHAN

**MICROWAVE & COMMUNICATION SYSTEMS
RESEARCH GROUP
SCHOOL OF ELECTRICAL AND ELECTRONIC
ENGINEERING**

Table of contents

Table of contents	1
List of Figures	6
List of tables	10
Abstract.....	11
Declaration.....	12
Copyright	13
Dedication	13
Acknowledgments	15
List of Papers	16
1. Introduction	17
References	23
2. Heterojunction Bipolar Transistors as Photodetectors – An Overview	26
2.1 Semiconductor concepts.....	26
2.1.1 Band Theory.....	26
2.1.1.1 Direct Semiconductors.....	28
2.1.1.2 Indirect Semiconductors	28
2.1.2 Semiconductor Doping	29
2.1.3 Carrier Transport.....	30
2.1.4 Carrier Generation/Recombination	32
2.1.5 p-n Junction.....	32
2.1.5.1 Reverse Biased Junction	33
2.1.5.2 Forward Biased Junction.....	34
2.1.5.3 Intrinsic Capacitances	34
2.1.6 Heterojunction Concepts	35
2.1.7 Bipolar Junction Transistors	37
2.1.7.1 Energy Band Diagram.....	38
2.1.7.2 Small Signal Equivalent Model.....	40
2.1.8 Heterojunction Bipolar Transistors	42
2.1.9 HBT Material Systems	45

2.1.9.1 $\text{Al}_{0.3}\text{Ga}_{0.7}\text{As} / \text{GaAs}$ HBTs	45
2.1.9.2 $\text{In}_{0.5}\text{Ga}_{0.5}\text{P} / \text{GaAs}$ HBTs	46
2.1.9.3 $\text{InP} / \text{In}_{0.53}\text{Ga}_{0.47}\text{As}$ HBTs	46
2.1.9.4 $\text{In}_{0.52}\text{Al}_{0.48}\text{As} / \text{In}_{0.53}\text{Ga}_{0.47}\text{As}$ HBTs	47
2.1.9.5 $\text{In}_{0.5}\text{Al}_{0.5}\text{P} / \text{GaAs}$ HBTs	47
2.1.9.6 Si / SiGe HBTs	47
2.1.10 Wavelength Sensitivity of Various Material Systems	48
2.2 Photodetection	49
2.2.1 Photodiodes	50
2.2.1.1 Factors Limiting the Speed of Photodiodes	52
2.2.1.2 Common Types of Photodiodes	53
2.2.1.2.1 p-i-n Photodiodes	53
2.2.1.2.2 Schottky Photodiodes	54
2.2.1.2.3 Avalanche Photodiodes	54
2.2.2 Heterojunction Phototransistors HPTs	55
2.2.2.1 Two-Terminal HPT	57
2.2.2.2 Three-Terminal HPT	60
2.3 Spectral Response Model for Detection	61
2.3.1 Basic Absorption Mechanism	61
2.3.2 Monolayer Detection for InP and GaAs	64
References	66
3. Device Structures and Experimental Setup	71
3.1 Device Structures	71
3.1.1 AlGaAs/GaAs sHPT	71
3.1.2 InP/InGaAs sHPT	74
3.1.2 InGaP/GaAs DHBT	75
3.2 Laser Operation and Characterisation	78
3.3 Experimental Setup	79
References	82
4. Spectral Response Modelling of HPTs	84
4.1 Methodology	85
4.2 Optical Flux Absorption	86

4.3 Absorption Coefficient	88
4.4 Collection Efficiency, η_c	91
4.5 Spectral Response, SR.....	91
4.2 Modelled and Measured Results	93
4.2.1 Short Wavelength Detection	93
4.2.2 Long Wavelength Detection	100
References	104
 5. Analytical Modelling of the Spectral Response.....	107
5.1 Device Modelling.....	108
5.1.1 Semiconductor Continuity Equation	109
5.1.2 Basic Assumptions	111
5.1.3 Photogeneration.....	111
5.1.4 Carrier Recombination	112
5.1.4.1 Radiative Recombination.....	112
5.1.4.2 SHR Recombination	112
5.1.4.3 Auger Recombination	113
5.1.5 Steady State Continuity Equations.....	114
5.1.5.1 Complementary Function.....	115
5.1.5.2 Particular Integral	115
5.1.5.3 Accurate Boundary Conditions	116
5.1.5.4 Fick's Law.....	119
5.1.6 Depleted Collector Absorption	120
5.1.7 Responsivity.....	121
5.2 Modelled and Measured Results.....	121
5.2.1 AlGaAs/GaAs HPTs.....	121
5.2.2 InP/InGaAs HPTs.....	123
5.2.3 Base Width Variation Consideration.....	125
References	128
 6. Photoresponse modelling of DHPTs.....	132
6.1 Optical Absorption	133
6.2 Photocurrent Generation in a DHPT	136
6.3 Small Signal Model.....	137

6.4 Results and Discussion	139
References	145
7. Conclusions and Further Work.....	148
7.1 Summary and Conclusions	148
7.2 Further Work.....	151
 Appendix A:	 153
Appendix B:.....	157
Appendix C:.....	160
Appendix D:	164
Appendix E:.....	165
Appendix F:	167
Appendix G:	169

Word Count : 32,608

List of Figures

Figure 2-1. Energy arrangement of (a) an isolated atom, (b) atoms in a solid.....	27
Figure 2-2. Energy band arrangement in various materials.	27
Figure 2-3. Energy-momentum curves for (a) a direct band-gap semiconductor (e.g. GaAs), and (b) an indirect band-gap semiconductor (e.g. Si).....	28
Figure 2-4. Schematic energy band representation of extrinsic semiconductors with (a) donor ions and (b) acceptor ions.	30
Figure 2-5. Various distributions for a typical uniformly doped abrupt $p^+ - n$ junction.	33
Figure 2-6. Energy band diagram of a wide band gap N-emitter and narrow band gap p-base abrupt heterojunction at thermal equilibrium (a) before and (b) after formation.	36
Figure 2-7. Schematic diagram of an npn BJT showing current components within for emitter ground configuration.....	37
Figure 2-8. Energy band diagram of npn BJT under bias in forward active mode. ...	39
Figure 2-9. Small-signal π - equivalent circuit for BJT at high frequency in common emitter configuration.	41
Figure 2-10. Energy band diagram of a graded Npn HBT in forward active mode.	43
Figure 2-11. Energy band diagram of an abrupt-junction Npn HBT in forward active mode.....	44
Figure 2-12. Loss Characteristics of a Silica Optical Fiber showing the three wavelengths of interest [23].....	48
Figure 2-13. Absorption coefficient for $In_{0.57}Ga_{0.43}As$ and GaAs as a function of incident wavelength.	50
Figure 2-14. Equivalent circuit of a photodiode.....	51
Figure 2-15. Cross-sectional view of a p-i-n photodiode.	54
Figure 2-16. Cross-sectional view of the HPT in forward active mode under illumination.	57
Figure 2-17. 2T HPT Configuration.....	58

Figure 2-18. Current flowing in a 2T-HPT under illumination.	58
Figure 2-19. 3T HPT Configuration.....	60
Figure 2-20. Schematic Illustration of the attenuation of the optical power density with the depth below the incident surface.....	62
Figure 2-21. Schematic of optical flux propagation, absorption and reflection for a multilayered semiconductor device.	63
Figure 2-22. Simulated results (MATLAB) for the fraction of flux absorbed as a function of wavelength for 10 μm mono-layers of InP and GaAs.....	64
Figure 3-1. Schematic device structure of AlGaAs/GaAs sHBT with numbers (1-8) being referred to table 3.1.	72
Figure 3-2. Typical metallization structure for (a) Ni/AuGe/Ni/Au on n-type GaAs, (b) Au/Zn/Au on p-type GaAs with a SI GaAs substrate.....	73
Figure 3-3. Micrograph of a fabricated Npn Al _{0.3} Ga _{0.7} As/GaAs HPT on K15 (emitter contact diameter = 135 μm).....	74
Figure 3-4. Micrograph of a fabricated Npn InP/In _{0.47} Ga _{0.53} As HPT on MR2021 (emitter contact diameter = 130 μm).	75
Figure 3-5. Epitaxial structure of the InGaP/GaAs DHBT.	76
Figure 3-6. Micrograph of the InGaP/GaAs DHBT under review.....	77
Figure 3-7. Active region of the device with marked lengths, Emitter width = 20 μm , Emitter/base length = 16 μm and Base width = 26 μm	77
Figure 3-8. Block diagram of the setup to characterise laser diodes.	79
Figure 3-9. Measured output characteristics for Sanyo DL-3148-033 laser diode...80	
Figure 3-10. Block diagram of experimental setup to obtain the DC electrical characteristics and the SR of HPTs.....	81
Figure 4-1. Schematic of optical flux absorption and propagation in various layers of an N-p-n HPT along with their schematic energy band diagrams.....	86
Figure 4-2. Measured refractive indices of various semiconductors as function of incident wavelength [18].	88
Figure 4-3. Measured absorption coefficients of various semiconductor materials as function of incident wavelengths [18].	89

Figure 4-4. Variation of absorption coefficient, α , with doping concentrations for both (a) n- and (b) p-GaAs layers.	90
Figure 4-5. Simulated and measured (at 635 nm, 780 nm, 808 nm and 850 nm) spectral response for the $\text{Al}_{0.3}\text{Ga}_{0.7}\text{As}/\text{GaAs}$ HPT along with its collection efficiency, η_c and quantum efficiency, η_q ($V_{CE} = 2.5\text{V}$).	94
Figure 4-6. Measured and simulated photogenerated currents with input optical power for various $\text{Al}_{0.3}\text{Ga}_{0.7}\text{As}/\text{GaAs}$ HPT layers at (a) 635nm and (b) 850nm ($V_{CE} = 2.5\text{ V}$).	96
Figure 4-7. Optical flux absorption profile for the $\text{Al}_{0.3}\text{Ga}_{0.7}\text{As}/\text{GaAs}$ HPT at various incident wavelengths for incident power of 100 μW	98
Figure 4-8. Measured and modelled output characteristics of the $\text{Al}_{0.3}\text{Ga}_{0.7}\text{As}/\text{GaAs}$ HPT at various input optical power for (a) 635nm and (b) 850nm.	99
Figure 4-9. Simulated and measured (at 980 nm, 1310 nm and 1550 nm) spectral response for the $\text{InP}/\text{In}_{0.47}\text{Ga}_{0.53}\text{As}$ HPT along with its collection efficiency, η_c and quantum efficiency, η_q ($V_{CE} = 2\text{ V}$).	100
Figure 4-10. Optical flux absorption profile for the $\text{InP}/\text{In}_{0.47}\text{Ga}_{0.53}\text{As}$ HPT at various incident wavelengths for incident power of 100 μW	102
Figure 4-11. Measured and modelled output characteristics of the $\text{InP}/\text{In}_{0.47}\text{Ga}_{0.53}\text{As}$ HPT at various input optical power for (a) 980nm and (b) 1550nm. ..	103
Figure 5-1. Schematic device structure of the $\text{Al}_{0.3}\text{Ga}_{0.7}\text{As}/\text{GaAs}$ HPT showing the incident radiation on the base region.	109
Figure 5-2. Simulated variation of surface recombination parameter $z(\alpha)$ with incident wavelengths for the $\text{Al}_{0.3}\text{Ga}_{0.7}\text{As}/\text{GaAs}$ HPT.	122
Figure 5-3. Measured and calculated spectral response of the $\text{Al}_{0.3}\text{Ga}_{0.7}\text{As}/\text{GaAs}$ HPT.	123
Figure 5-4. Simulated variation of surface recombination parameter $z(\alpha)$ with incident wavelengths for the $\text{InP}/\text{In}_{0.47}\text{Ga}_{0.53}\text{As}$ HPT.	124
Figure 5-5. Measured and calculated spectral response of the $\text{InP}/\text{In}_{0.47}\text{Ga}_{0.53}\text{As}$ HPT.	125
Figure 5-6. Variation of Responsivity with base width for the $\text{Al}_{0.3}\text{Ga}_{0.7}\text{As}/\text{GaAs}$ HPT at various incident wavelengths.	126
Figure 5-7. Variation of responsivity with base width for the $\text{InP}/\text{In}_{0.47}\text{Ga}_{0.53}\text{As}$ HPT at various incident wavelengths.	127

Figure 6-1. Schematic of optical flux absorption and propagation in various layers of sHPT (A) along with the flux reflections in the base layer of a DHPT (B).	134
Figure 6-2. Schematic cross-section of a small-geometry npn HBT together with its lumped element T-shape small-signal equivalent circuit[14]	137
Figure 6-3. Small signal equivalent of the $In_{0.49}Ga_{0.51}P/GaAs$ DHBT in common source mode indicating intrinsic and extrinsic parameters.....	140
Figure 6-4. Measured and simulated photoresponse of the $In_{0.49}Ga_{0.51}P/GaAs$ DHBT, $V_{ce}= 3$ V.....	141
Figure 6-5. Variation of base emitter capacitance and resistance and base collector capacitance with input optical power $In_{0.49}Ga_{0.51}P/GaAs$ DHPT.....	142
Figure 6-6. Variation of the photoresponse with intrinsic base resistance at 4 GHz for the $In_{0.49}Ga_{0.51}P/GaAs$ DHPT.	143
Figure 6-7. Photoresponse variation with input optical power for the $In_{0.49}Ga_{0.51}P/GaAs$ DHPT at 4 GHz.	144

List of tables

Table 1.1: Comparison between various techniques and devices in the viewpoint of microwave signal processing applications.	19
Table 2.1: Band discontinuities for various HBT material heterostructures.....	45
Table 3.1: Layer structure for graded emitter/base junction AlGaAs/GaAs sHBT....	72
Table 3.2: Layer structure for lattice-matched InP/In _{0.47} Ga _{0.53} As HPT.....	74
Table 3.2: Doping profile of the InGaP/GaAs DHBT.	76
Table 5.1: Material parameters used for AlGaAs/GaAs HPTs simulation.	121
Table 5.2: Material parameters used for InP/InGaAs HPTs simulation.	123
Table 6.1: Extracted parameters for InGaP/GaAs DHBT (16x20 μm^2 BE area).....	138

Abstract

The optoelectronics industry continues to demand improved materials, devices and systems for the generation, transmission, detection, amplification and processing of optical signals. Heterojunction phototransistors (HPTs), in recent years, have attracted considerable interest for optical detection due to their intrinsic gain, low noise performance, high-frequency operation and process and the device layer compatibility with heterojunction bipolar transistors for high-speed optoelectronic monolithic microwave/millimetre-wave integrated circuit (OEMMIC) photoreceivers.

A key performance parameter of HPTs is their spectral response (SR) which is critical in their usage in optical applications. The SR depends on several inherent factors including material absorption coefficient, refractive index, device structure, doping and temperature of operation along with the external factors such as bias voltage and the energy of incident radiation. The spectral response and optical characteristics of GaAs-based and InP-based sHPTs have been successfully predicted for the first time through an advanced absorption theoretical model. The model is based on the accurate prediction of photocarriers in the active layers of the phototransistor which, when related to the base current of the transistor in forward active mode, enables the prediction of optical characteristics. The importance of collection efficiency in accurate SR modelling is highlighted and the layer dependence of the optical flux absorption profile at near-band gap wavelengths is also investigated and its generalisation as a single-exponential has been refuted for GaAs-based HPTs.

Analytical modelling of the spectral response has also been developed from the resolution of continuity equations that govern the excess optically generated minority carrier variation in the active layers of the HPT, taking into account the related physical parameters. Realistic boundary conditions have been considered for efficient device operation and a detailed optical flux absorption profile is constructed for accurate device modelling. This analytical model provides insight into the direct influence of various parameters (such as base width and carrier concentration) on the device performance, thus, providing a valuable optimization tool for the future design of HPTs in optical receivers.

The measured results at 635 nm, 780 nm 808 nm and 850 nm for $\text{Al}_{0.3}\text{Ga}_{0.7}\text{As}/\text{GaAs}$ HPTs and 980 nm, 1310 nm and 1550 nm for $\text{InP}/\text{In}_{0.47}\text{Ga}_{0.53}\text{As}$ HPTs show good agreement with the predicted data, validating the proposed theoretical model.

Finally, a detailed absorption model and photoresponse of double heterojunction phototransistors in a top/surface-illuminated orientation has been analyzed with a modified small-signal model. The effect of incident optical illumination on intrinsic small-signal parameters such as resistances and capacitances has been discussed and analyzed for photoresponse modelling.

Declaration

No portion of the work referred to in the thesis has been submitted in support of an application for another degree or qualification of this or any other university or other institute of learning.

Copyright

1. The author of this thesis (including any appendices and/or schedules to this thesis) owns any copyright in it (the “Copyright”) and s/he has given The University of Manchester the right to use such Copyright for any administrative, promotional, educational and/or teaching purposes.
2. Copies of this thesis, either in full or in extracts, may be made only in accordance with the regulations of the John Rylands University Library of Manchester. Details of these regulations may be obtained from the Librarian. This page must form part of any such copies made.
3. The ownership of any patents, designs, trade marks and any and all other intellectual property rights except for the Copyright (the “Intellectual Property Rights”) and any reproductions of copyright works, for example graphs and tables (“Reproductions”), which may be described in this thesis, may not be owned by the author and may be owned by third parties. Such Intellectual Property Rights and Reproductions cannot and must not be made available for use without the prior written permission of the owner(s) of the relevant Intellectual Property Rights and/or Reproductions.
4. Further information on the conditions under which disclosure, publication and commercialisation of this thesis, the Copyright and any Intellectual Property and/or Reproductions described in it may take place is available in the University IP Policy (see <http://www.campus.manchester.ac.uk/medialibrary/policies/intellectual-property.pdf>), in any relevant Thesis restriction declarations deposited in the University Library, The University Library’s regulations (see <http://www.manchester.ac.uk/library/aboutus/regulations>) and in The University’s policy on presentation of Theses.

*To
my parents
and
in loving memory of my grandfather*

Acknowledgments

I express my sincere gratitude to my supervisor Professor Ali Rezazadeh for his continuous guidance and inspiration which kept me on the right track and helped me get through difficult parts of the project. His knowledge and professionalism always guided me through difficult parts of the research and helped me to achieve my goal for this research. In addition, I would also like to thank Dr Suba Subramaniam, Dr Van Tuyen Vo, Dr Qing Sun, Dr Tauseef Tauqeer, Mr Jimmy Tan, Mr Aneeq Mehmood and Mr Sarmad Sohaib for several fruitful discussions.

I am highly grateful to all my friends from Weston Hall, University of Manchester, and to my colleagues in the MACS group. They have been like a family to me and a great source of continuous encouragement.

I would take this opportunity to show my appreciation to my teachers for all my academic achievements and I would like a special mention for Mahar Sajjad Hussain for his continuous supervision, encouragement and backing throughout my academic life. In addition, I am indebted to Anwar Mehmood Paracha for his career advice which lead to my prospective Doctorate.

Finally, I thank my parents and brothers for their continuous support and encouragement throughout this time and all my life.

List of Papers

Journals

- H. A. Khan and A. A. Rezazadeh, "Spectral response modelling of GaAs-based heterojunction phototransistors for short wavelength detection," *Optoelectronics, IET*, vol. 4, pp. 57-63, 2010.
- H. A. Khan and A. A. Rezazadeh, "Analytical modelling of the spectral response of heterojunction phototransistors," *IEEE Electron Device Letters*, vol. 30, pp. 1158-1160, 2009.
- H. A. Khan and A. A. Rezazadeh, "Modelling and Analysis of the Spectral Response for InP/InGaAs HPTs in OEMMICs for long wavelength Optical Communication," submitted to *European Journal of Physics*, 2010.
- H. A. Khan and A. A. Rezazadeh, "Photoresponse Modelling and Analysis of DHPTs for Short Wavelength Optical Receivers," submitted to *Electronics Letters*, 2010.

Conferences

- H. A. Khan and A. A. Rezazadeh, "Optical Absorption Mechanism and Interfacial Analysis of HPTs for Lightwave Technologies", *Novel Aspects of Surfaces and Materials, NASM 2010*, April 11th-15th, Manchester, 2010.
- H. A. Khan and A. A. Rezazadeh, "Optical Detection in HPTs for Remote Sensing Applications", *Annual Conference on New Directions in Photon Science*, January 20th, Manchester, UK, 2010.
- H. A. Khan and A. A. Rezazadeh, "Heterojunction Phototransistors for Optical Detection", *EEE PGR Conference 2008*, The University of Manchester, November 12th, Manchester, UK, 2008.
- H. A. Khan, A. A. Rezazadeh, and S. C. Subramaniam, "Spectral response modelling of heterojunction phototransistors for short wavelength transmission," *IEEE European Microwave Integrated Circuit Conference, EuMIC 2008*, October 27 - October 31, Amsterdam, Netherlands, 2008.
- H. A. Khan and A. A. Rezazadeh, "Optical Absorption Mechanism in Heterojunction Phototransistors", Annual conference on all aspects of semiconductor research, *UK Semiconductor 2008*, 2-3 July, Sheffield, UK, 2008.

Chapter 1

Introduction

Optoelectronic systems are becoming increasingly more capable due to advances in both optics and electronics. Miniaturization of hardware and an exponential increase in computer processing capacity and speed has enabled the creation of advanced optoelectronic systems that has resulted in smart weapons and modern industrial and medical equipment. Optical telecommunication networks or photonic networks have gained increasing popularity over their conventional copper cable and microwave counterparts due to advantages such as higher capacity, high security, electromagnetic interference immunity, and flexibility of bandwidth [1-3]. The superiority of optical fibre communication systems over cabled or microwave systems demands an efficient conversion of optical signals to electrical signals and vice versa. Thus, an efficient interface between optical and microwave components is required for achieving higher performance and improved integration in optoelectronic systems. Understandably, the study of the detection of optical signals and their subsequent amplification has gained impetus in recent years [4-6].

Currently, an exploding growth of mobile internet subscribers has ignited a major interest in broadband wireless services such as high-speed wireless local-area networks (WLAN), broadband wireless access (BWA) and intelligent traffic systems (ITS) [7]. In spite of the large interest, millimetre-wave wireless communication systems are not yet widespread due to the difficulties in millimetre-wave generation, processing and transmission [8]. Fibre-optic technologies have been introduced as solutions to the associated problems, resulting in fibre-optic/millimetre-wave data transmission systems [9]. The merging of fibre-optic wireline and micro/millimetre-wave wireless links is referred to as radio over fibre. Such systems transmit RF signals and data to antenna base stations through optical fibre [10, 11]. This results in a low loss, huge bandwidth transmission medium and its incorporation with previously deployed fibre-optic networks, which makes it an ideal candidate for realizing micro-cellular networks in millimetre-wave wireless communication

systems such as high-speed wireless LANs, wireless personal networks (WPN) and road-to-vehicle communications in ITS [12]. Recently, mobile service providers have begun to utilize these fibre-optic technologies for wireless services in closed areas where subscribers cannot access antenna base stations, for example, in the shadow of a building, for in-building applications and underground areas.

Encouraged by the increasing demand for improved optoelectronic components, a large number of devices (emitters, detectors and modulators) has been developed and introduced in the past decade, most of them based on III–V semiconductors. Si-based optoelectronic detectors have also been investigated as Si electronics is a well-developed and widespread technology, in which monolithic integration with control/driving electronics is possible, with the ensuing potential for low cost. Despite high optical responsivity, speed limitations make Si unsuitable material for high-speed optical communication.

For the purpose of optical detection, photodiodes are most commonly used. The optical signal to be detected is generally weak and requires amplification. Avalanche photodiodes (APDs) have been widely employed as optical detectors for their optical gain. However, their use is limited as they add noise to the signal and increase the noise-equivalent power accordingly. Most receiver-designs employ p-i-n photodiodes due to their simple biasing and operation. However, there is always a trade-off between the width of the intrinsic layer and the transit times which limits the frequency performance of the device [13, 14]. Schottky photodetectors show a good frequency response but provide no internal amplification for the signal.

Phototransistors based on metal–semiconductor field-effect transistors (MESFETs), high electron mobility transistors (HEMTs), and heterojunction bipolar transistors (HBTs) are useful devices because they provide high internal gain without the avalanche noise [15-17]. Phototransistors can also be used as optoelectronic mixers, which simultaneously perform photodetection and frequency up-conversion in a single device [18]. In addition, these phototransistors are fully compatible with monolithic-microwave integrated-circuit (MMIC) processes [19, 20].

Compared with field-effect devices, bipolar transistors employ vertical current transport, which offers better utilization of wafer area and thus leads to higher power density. The bipolar approach also offers higher linearity at higher power levels, superior power-added-efficiency, and smaller frequency noise as necessary for RF circuits and systems [21]. In addition, HBTs have a simple fabrication process for monolithically integrated photoreceivers, when HBTs are used as heterojunction phototransistors or the base-to-collector region of the HBT is used as a p-i-n photodiode [22].

Choosing a device technology depends on several factors including system specification, application and cost. A comparison of the relative merits of each microwave device is described in Table 1-1 [10, 12, 22]. The progress of gallium arsenide (GaAs) MMIC technologies has resulted in the development of GaAs-based phototransistors which can be integrated with high-speed microwave transistors on a single GaAs substrate [23, 24]. The realization of AlGaAs/GaAs heterojunctions has accelerated the development of phototransistors both HEMT- and HBT-based phototransistors. However, the band gap limitation prevents GaAs- and Si- based transistors from detecting optical signals in the long wavelength regions, thus limiting their operating range to short wavelength detection only.

Figures of Merit	Si CMOS	Si BJT	SiGe HBT	GaAs MESFET	GaAs HEMT	GaAs HBT	InP HEMT	InP HBT
Operating Frequency	1	1	2	2	3	2	4	4
Breakdown Voltage	1	1	2	2	2	3	1	2
Threshold Uniformity	2	3	3	2	1	3	1	3
O/p Power Density	1	3	2	2	2	3	2	3
Low Freq. Noise	2	3	3	1	1	3	1	3
High Freq. Noise	1	1	2	2	3	1	4	1
Maturity	3	3	2	3	3	3	1	1
Cost	3	3	3	2	2	2	1	1

Table 1.1: Comparison between various techniques and devices in the viewpoint of microwave signal processing applications (1-poor, 2-average, 3-good and 4-very good).

InP-based devices are better suited to high-speed communication when compared to GaAs counterparts and material compatibility with long wavelengths (1.3-1.55 μm) makes them suitable front-end detectors for long-haul optical applications. Other inherent advantages of InP-based HBTs are their lower turn-on voltages, higher transconductance, good output current drive and, as mentioned previously, higher frequency performance [25].

Motivated by the inherent advantages of HPTs in general, this project was aimed at providing further understanding of the theoretical modelling of the SR of HPTs and an investigation into the various material systems used for phototransistors. Ideally, these models should be semi-physical, i.e. they should clearly show the relationship between the modelled parameters on one side and the dimensions as well as the doping concentrations of HPTs on the other side. Only such models allow the optimisation of devices, and with the possibility of modelling various physical processes inside a device, can lead to intuitive understanding of device function.

$\text{Al}_{0.3}\text{Ga}_{0.7}\text{As}/\text{GaAs}$ and lattice matched $\text{InP}/\text{In}_{0.53}\text{Ga}_{0.47}\text{As}$ sHPTs have been the focus of attention in this project and the spectral response modelling of these devices has been successfully achieved through detailed analytical modelling. A comprehensive absorption model of double heterojunction phototransistors has also been developed and photoresponse modelling has been studied through a modified small-signal model. New results obtained with respect to the modelling of such devices are reported in this thesis.

A general discussion of the main motivation for this work has been presented in chapter 1. The key objectives and various devices examined for this project have been outlined. Chapter 2 describes the background theory of heterojunction transistors and their uses as photodetectors. Various aspects of semiconductors such as band theory, doping, carrier transport, generation/recombination of carriers and pn junction theory are discussed. A detailed comparison between photodiodes and phototransistors is given which is followed by a spectral response model to predict the absorption behaviour of mono-layer detectors. A brief discussion regarding the various HBT material systems and their properties is also given.

Chapter 3 focuses on the devices used in experiments followed by the experimental setup. The doping profiles and micrographs for large geometry $\text{Al}_{0.3}\text{Ga}_{0.7}\text{As}/\text{GaAs}$ sHPT, $\text{InP}/\text{In}_{0.47}\text{Ga}_{0.53}\text{As}$ sHPT and microwave $\text{In}_{0.49}\text{Ga}_{0.51}\text{P}/\text{GaAs}$ DHBT are given in this chapter, followed by the block diagram of the experimental setup used to obtain the electrical characteristics and the SR of HPTs. In chapter 4, an advanced optical absorption model for single-HPTs (sHPTs) is proposed, which is then used to predict the SR and optical characteristics of an N-p-n $\text{Al}_{0.3}\text{Ga}_{0.7}\text{As}/\text{GaAs}$ and an $\text{InP}/\text{In}_{0.53}\text{Ga}_{0.47}\text{As}$ HPT in two-terminal (floating base) mode. A detailed absorption model and optical flux absorption profile is constructed for accurate device modelling and the significance of collection efficiency in accurate responsivity modelling is highlighted and it is not considered unity (as with the previous state of the art). The simulated results are compared to measured data at 635 nm, 780 nm, 808 nm and 850 nm for a GaAs-based HPT for short wavelength detection. The measured results for 980 nm, 1310 nm and 1550 nm using InP-based HPTs for long wavelength detection have also been provided along with the theoretical SR.

In chapter 5, the basic semiconductor equations and transport model, based on the current balancing concept for electron and hole injection currents, are reviewed for HPT modelling. The SR, based on the formulation of semiconductor continuity equations, has been accurately modelled for $\text{Al}_{0.3}\text{Ga}_{0.7}\text{As}/\text{GaAs}$ and $\text{InP}/\text{In}_{0.53}\text{Ga}_{0.47}\text{As}$ HPTs. The effect of doping on the absorption coefficient at near band gap wavelengths has been taken into account along with the subtle variation of refractive index caused by the changes in incident photon energies. Realistic boundary conditions have been considered for efficient HPT operation. A detailed analysis of physical and material parameters, inherently associated with analytical expressions, has also been provided.

A novel formulation for optical flux absorption in surface illuminated Double-HPTs (DHPTs) along with its comparison with single-HPTs (sHPTs) is presented in chapter 6. The photoresponse of an $\text{In}_{0.49}\text{Ga}_{0.51}\text{P}/\text{GaAs}$ NpN DHBT using a modified small signal model has been modelled and compared with the measured results. The variation of various intrinsic elements of the device with the optical signal has also

been analysed and discussed in this chapter. In the concluding chapter of this thesis, various findings from the research study are summarised. This chapter also includes proposals for further investigative work based on the research work presented in the thesis.

References

- [1] E. M. Dianov, "Fibre optics: Forty years later," *Quantum Electronics*, vol. 40, pp. 1-6, 2010.
- [2] J. Gower, *Optical Communication Systems*, 2nd ed: Prentice Hall, 1993.
- [3] S. M. Sze, *Physics of Semiconductor Devices*, 2nd ed. USA: John Wiley & Sons, 2001.
- [4] K.-W. Ang, M.-B. Yu, G.-Q. Lo, and D.-L. Kwong, "Low-voltage and high-responsivity germanium bipolar phototransistor for optical detections in the near-infrared regime," *IEEE Electron Device Letters*, vol. 29, pp. 1124-7, 2008.
- [5] Y. W. Byun, M. S. Park, Y. H. Park, Y. C. Cho, and J. H. Jang, "InGaP/GaAs heterojunction phototransistors for ultra-low optical power detection," presented at 2009 IEEE International Conference on Indium Phosphide & Related Materials, 10-14 May 2009, Piscataway, NJ, USA, 2009.
- [6] Y.-C. Jo, S.-J. Joe, H. Kim, and P. Choi, "Optical characteristics of responsivity-enhanced InGaAs/InP heterojunction phototransistors," *Japanese Journal of Applied Physics, Part 1 (Regular Papers, Short Notes & Review Papers)*, vol. 44, pp. 2537-40, 2005.
- [7] S. Pato, J. Pedro, and P. Monteiro, "Comparative evaluation of fibre-optic architectures for next-generation Distributed Antenna Systems," presented at ICTON 2009: 11th International Conference on Transparent Optical Networks, June 28, 2009 - July 2, 2009, Ponta Delgada, Portugal, 2009.
- [8] C.-S. Choi, H.-S. Kang, W.-Y. Choi, D.-H. Kim, and K.-S. Seo, "Phototransistors based on InP HEMTs and their applications to millimeter-wave radio-on-fiber systems," *IEEE Transactions on Microwave Theory and Techniques*, vol. 53, pp. 256-63, 2005.
- [9] H. Al-Raweshidy and S. Komaki, *Radio-over-fiber technologies for mobile communications networks*. Norwood, MA: Artech House, 2002.
- [10] A. J. Seeds and K. J. Williams, "Microwave photonics," *Journal of Lightwave Technology*, vol. 24, pp. 4628-41, 2006.
- [11] A. Vildot, B. Cabon, and J. Chazelas, *Microwave photonics from components to applications and systems*: Kluwer Academic Publisher, 2003.

- [12] C.-S. Choi, "Phototransistors based on InP HEMTs and HBTs, and their applications to fiber-optic/millimeter-wave data transmission systems," PhD Thesis, Yonsei University, 2005.
- [13] K. Ishii, H. Nosaka, M. Ida, K. Kurishima, T. Enoki, T. Shibata, and E. Sano, "High-input-sensitivity, low-power 43 Gbit/s decision circuit using InP/InGaAs DHBTs," *Electronics Letters*, vol. 38, pp. 557-558, 2002.
- [14] S. M. Frimel and K. P. Roenker, "Thermionic-field-diffusion model for Npn bipolar heterojunction phototransistors," *Journal of Applied Physics*, vol. 82, pp. 1427, 1997.
- [15] W. Hafez, J.-W. Lai, and M. Feng, "Low-power high-speed operation of submicron InP-InGaAs SHBTs at 1 mA," *IEEE Electron Device Letters*, vol. 24, pp. 427-429, 2003.
- [16] N. Jiang and Z. Ma, "Current gain of SiGe HBTs under high base doping concentrations," *Semiconductor Science and Technology*, vol. 22, pp. 168-72, 2007.
- [17] E. Sano, K. Kurishima, H. Nakajima, and S. Yamahata, "High-speed, low-power lightwave communication ICs using InP/InGaAs double-heterojunction bipolar transistors," *IEICE Transactions on Electronics*, vol. E83-C, pp. 2000-2006, 2000.
- [18] C. Gonzalez, J. Thuret, J. L. Benchimol, and M. Riet, "Optoelectronic up-converter to millimetre-wave band using an heterojunction bipolar phototransistor," presented at Proceedings of the 1998 24th European Conference on Optical Communication, ECOC. Part 1 (of 3), September 20, 1998 - September 24, 1998, Madrid, Spain, 1998.
- [19] T. Shimura, M. Komaru, S. Izumi, T. Kuragaki, M. Sakai, H. Nakano, S. Terazono, K. Nagahama, K. Nishitani, and M. Otsubo, "High power density and high efficiency AlGaAs/GaAs heterojunction bipolar transistors for high power MMICs," presented at 23rd International Conference on Solid State Devices and Materials - SSDM '91, August 27, 1991 - August 29, 1991, Yokohama, Jpn, 1991.
- [20] M. A. Di Forte-Poisson, S. L. Delage, and S. Cassette, "GaAs-based materials for heterojunction bipolar transistor's: Reliability results and MMIC applications," 2001.

- [21] O. Esame, Y. Gurbuz, I. Tekin, and A. Bozkurt, "Performance comparison of state-of-the-art heterojunction bipolar devices (HBT) based on AlGaAs/GaAs, Si/SiGe and InGaAs/InP," *Microelectronics Journal*, vol. 35, pp. 901-908, 2004.
- [22] H. Sheng, "Modelling, Fabrication and Characterisation of InP-HBTs for Future High-Speed, Low-Power Optical Telecommunications," Ph.D thesis, King's College London, 2000.
- [23] J.-I. Shirakashi and M. Konagai, "InGaP/GaAs and InP/InGaAs heterojunction bipolar transistors with a super heavily carbon-doped base grown by metalorganic molecular beam epitaxy," *Proceedings of the Topical Workshop on Heterostructure Microelectronics, August 17 - 19, 1994*.
- [24] A. Rezazadeh, " Design and Technology of III-V HBTs for wireless communications," presented at Wireless Broadband Forum, Cambridge, UK, 2002.
- [25] S. C. Subramaniam, "Ion-Implant Isolation of InP/InGaAs HBTs," Ph.D thesis, The University of Manchester, 2005.

Chapter 2

Heterojunction Bipolar Transistors as Photodetectors – An Overview

2.1 Semiconductor Concepts

A semiconductor is a solid whose electrical conductivity is between that of a conductor and that of an insulator, and can be controlled over a wide range, either permanently or dynamically. In the formation of a semiconductor crystal, isolated atoms are brought close together and they interact with neighbouring atoms. The forces of attraction and repulsion between the atoms find equilibrium at the proper inter atomic spacing in the crystal. The reduction in inter-atomic spacing causes the electron wavefunctions to overlap. To avoid violating the Pauli Exclusion Principle, which states that no two electrons can have the same set of quantum numbers, there is a splitting of the discrete energy levels of the isolated atoms into new levels [1, 2].

2.1.1 Band Theory

The splitting of the energy levels forms a set of bands of very closely spaced levels, with ‘forbidden’ energy gaps between them as shown in Figure 2-1. Electrons occupy the lowest possible energy bands. However, as these levels become full, they do not play a role in determining the electrical properties of the crystal. The two highest bands (the valence and conduction bands) are of crucial importance as they are separated by the forbidden energy gap (E_g) between them [3].

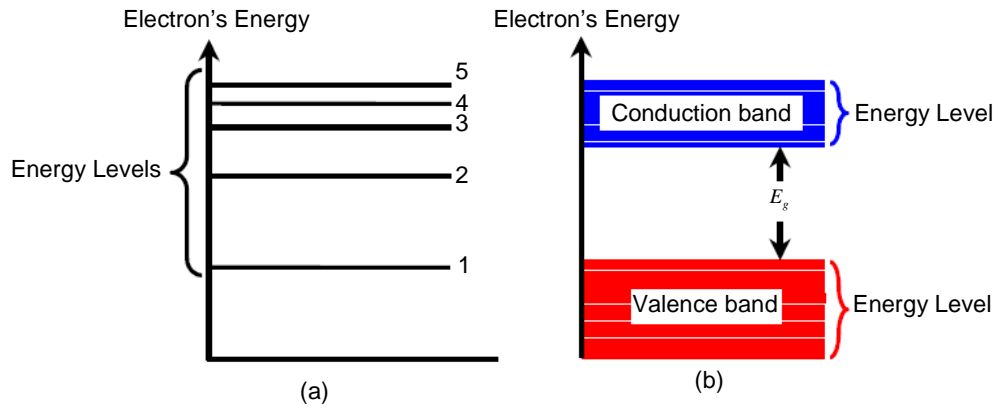


Figure 2-1. Energy arrangement of (a) an isolated atom, (b) atoms in a solid.

The lowermost unoccupied band is called the conduction band and when electrons are excited to the conduction band, the current flows in the semiconductor. The difference between insulators and semiconductors is only that the forbidden band gap between the valence band and conduction band is much larger in an insulator. This forbids the electrons going to the conduction band and the electrical conductivity for an insulator is minimal. On the other hand, the metals have high electrical conductivity because bands either overlap or are only partially filled. This is summarized in Figure 2-2.

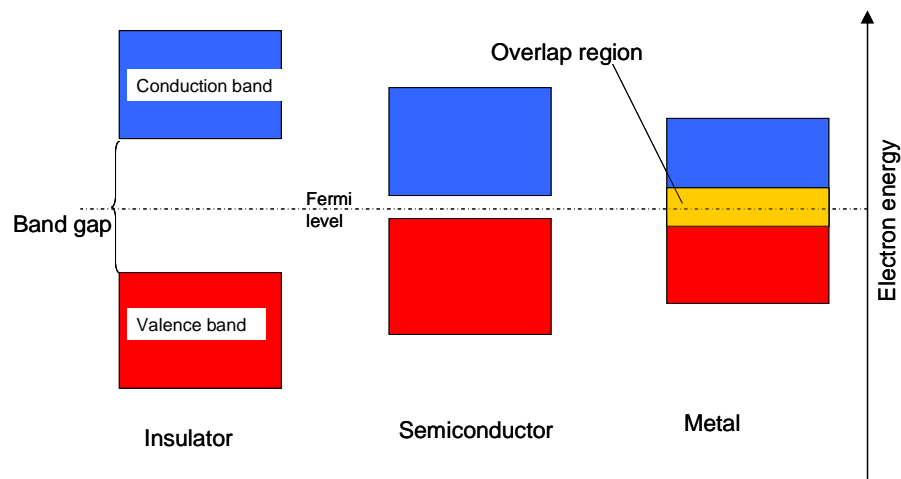


Figure 2-2. Energy band arrangement in various materials.

On the basis of the energy-momentum ($E - k$) curves, the semiconductors can be classified into two types; direct and indirect semiconductors [4].

2.1.1.1 Direct Semiconductors

Those semiconductors in which the minimum of the conduction band and maximum of the valence band occur at the same value of momentum, k (at $k = 0$) are referred to as direct band gap semiconductors as seen in Figure 2-3(a). Common examples of such materials include Gallium Arsenide (GaAs) and Indium Phosphide (InP). Direct band gap materials are suitable light emitters such as lasers or light emitter diodes (LEDs).

2.1.1.2 Indirect Semiconductors

Materials such as silicon and germanium are classed as indirect band gap semiconductors as the carriers experience a momentum change in order for the generation or recombination process to take place. In these semiconductors the minimum of the conduction band and maximum of the valence band do not occur at the same value of k . If such semiconductors are considered for optical detection, they are usually poor detectors as some part of energy is released in the form of heat.

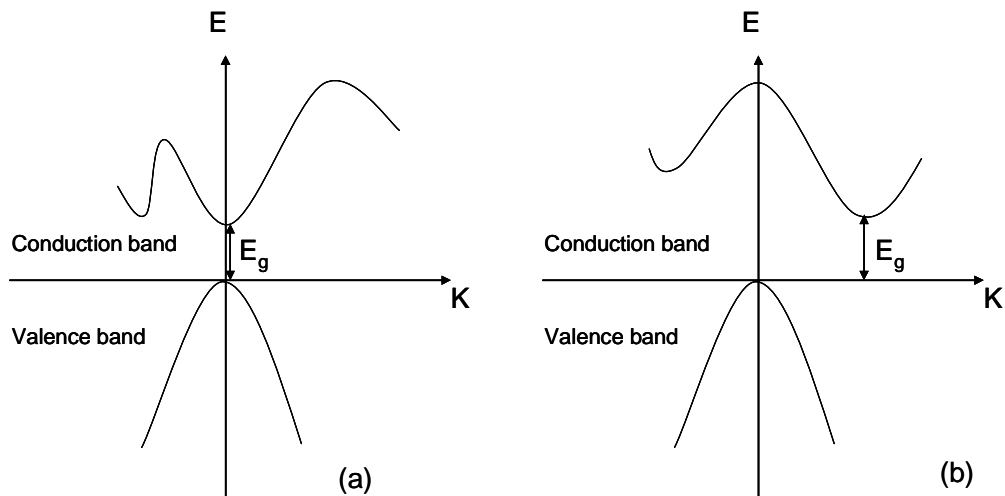


Figure 2-3. Energy-momentum curves for (a) a direct band-gap semiconductor (e.g. GaAs), and (b) an indirect band-gap semiconductor (e.g. Si).

2.1.2 Semiconductor Doping

Semiconductor characteristics can be altered by doping, in other words, by adding impurity atoms to a relatively pure semiconductor material. This results in the change in intrinsic characteristics by the addition of induced impurity energy levels. Lightly and moderately doped semiconductors are referred to as extrinsic. A semiconductor which is doped to such high levels that it acts more like a conductor than a semiconductor is called a degenerated semiconductor [5].

The doping process leads to two different types of extrinsic semiconductors depending on the number of valence electrons the doping atoms have. These are p-type and n-type extrinsic semiconductors. The n-type semiconductor will be formed when the doping atoms have more valence electrons than those of the doped semiconductor, e.g. a silicon crystal may be transformed into n-type material by doping it with a five valence electron material such as arsenic. The arsenic atom will form covalent bonds with its four neighboring silicon atoms, and the fifth electron will be free to act as a negative charge carrier making the material n-type. In this case, the arsenic acts as a donor. On the other hand, the p-type material may be formed by doping a silicon atom with a three valence electron atom, such as boron. The boron atom will form three covalent bonds with three neighboring silicon atoms and an electron-deficiency (a hole) is created and therefore boron acts as an acceptor. This can be summarized by Figure 2-4.

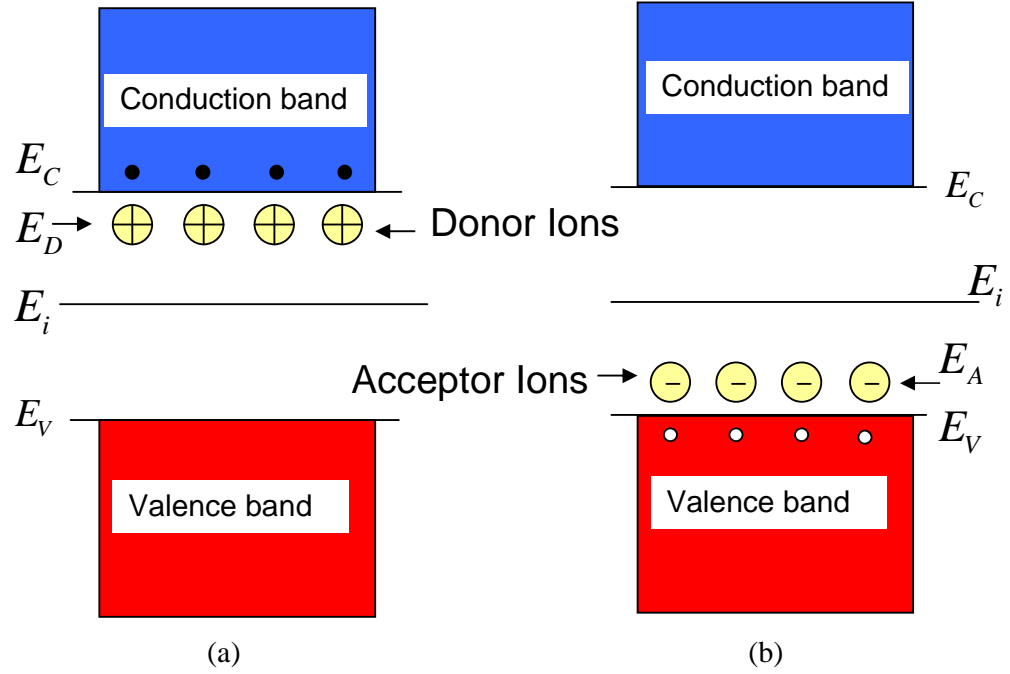


Figure 2-4. Schematic energy band representation of extrinsic semiconductors with (a) donor ions and (b) acceptor ions (adapted from Figure 19 in [6]).

2.1.3 Carrier Transport

Due to the motion of carriers in a crystal structure, there are bound to be collisions between carriers and the atoms which could be lattice atoms or the impurity atoms. However, under the influence of an electric field the motion of the carrier changes. For instance, an electric field (E) applied to a semiconductor will exert a force of magnitude $-qE$ (where q is the charge on electrons) on the electrons. These electrons will accelerate in the opposite direction to the field, colliding with the atoms, and an additional component of velocity will be superimposed upon its thermal motion. This new velocity component is called drift velocity (v_d) [6]. v_d is proportional to the applied electric field at low values of E , and the proportionality factor is the electron mobility (μ) which depends on the mean time between the collisions (τ_c) and the effective mass (m^*). The drift velocity and the mobility can therefore be related by (2.1).

$$v_d = -\mu E \quad (2.1)$$

The negative sign denotes the fact that the drift velocity is in the opposite direction to the applied electric field. The electron mobility describes how strong the motion of an electron is in the presence of an applied electric field and is given by (2.2).

$$\mu = \frac{q\tau_c}{m^*} \quad (2.2)$$

When the electric field is sufficiently high, (2.1) no longer remains valid. The carriers will collide at a high constant rate no matter how intense the electric field is, and the total velocity of the carriers will be equal to the ‘saturation velocity’. The associated resistance to the motion of the carriers can be linked to resistivity (ρ) of the semiconductor which can be given as [5]:

$$\rho = \frac{1}{q(n\mu_n + p\mu_p)} \quad (2.3)$$

where n (μ_n) and p (μ_p) are the electron and hole density (mobility) respectively. Generally, in extrinsic semiconductors, only one of the components in (2.3) is significant. Therefore (2.3) reduces to,

$$\rho = \frac{1}{qn\mu_n} \text{ for n-type semiconductor} \quad (2.4)$$

$$\rho = \frac{1}{qp\mu_p} \text{ for p-type semiconductor} \quad (2.5)$$

The resistance of a semiconductor material can then be calculated from (2.6):

$$R = \rho \frac{l}{A} \quad (2.6)$$

where A is the cross-section area normal to the current direction and l is the length of the semiconductor. The motion of carriers generated by the applied electric field represents drift current (J), and is written as [5]:

$$J = \sigma E = \frac{1}{\rho} E \quad (2.7)$$

where σ is the conductivity of the semiconductor which is the inverse of resistivity.

Another important current component can also exist if the doping concentration is not homogeneous throughout the structure, as the carriers move from a region of higher concentration to a region of low concentration, resulting in another form of current component called ‘diffusion current’.

2.1.4 Carrier Generation/Recombination

Whenever the thermal condition is disturbed in a semiconductor, some mechanism has to take place to restore the equilibrium. If the carriers are injected using optical excitation, an electron-hole pair will be generated as an electron makes an upward transition from the valence to the conduction band. However, the energy of the incident photons should be larger than the band gap of the material (this will be discussed further in Section 4.1). This process is called ‘carrier generation’. The process that attempts to restore the thermal equilibrium condition is the ‘recombination’ in the structure. Recombination of electron-hole pairs releases energy in the form of photons or heat to the lattice depending upon the type of process. When a photon is emitted the process is called radiative recombination; otherwise, it is called nonradiative recombination [4, 6].

2.1.5 p-n Junction

A p-n junction is formed when n-type and p-type semiconductors make physical contact. The difference in the concentration at the interface will produce diffusion of carriers from one material to the other. The diffused minority carriers will recombine with the majority carriers of the other material. Electrons near the p-n interface tend to diffuse into the p region and vice versa. As electrons diffuse, they leave positively charged ions (donors) on the n-side. Similarly, the movement of holes into the n-type region will leave fixed ions (acceptors) with negative charge. Doping atoms are fixed to the lattice and will produce negative and positive space charge regions, which together are known as a ‘depletion region’. The neutral side of the p-type material along with the neutral side of the n-type material present an electrostatic potential difference, this potential difference at thermal equilibrium being known as the built-in potential (V_{bi}). This is summarized in Figure 2-5.

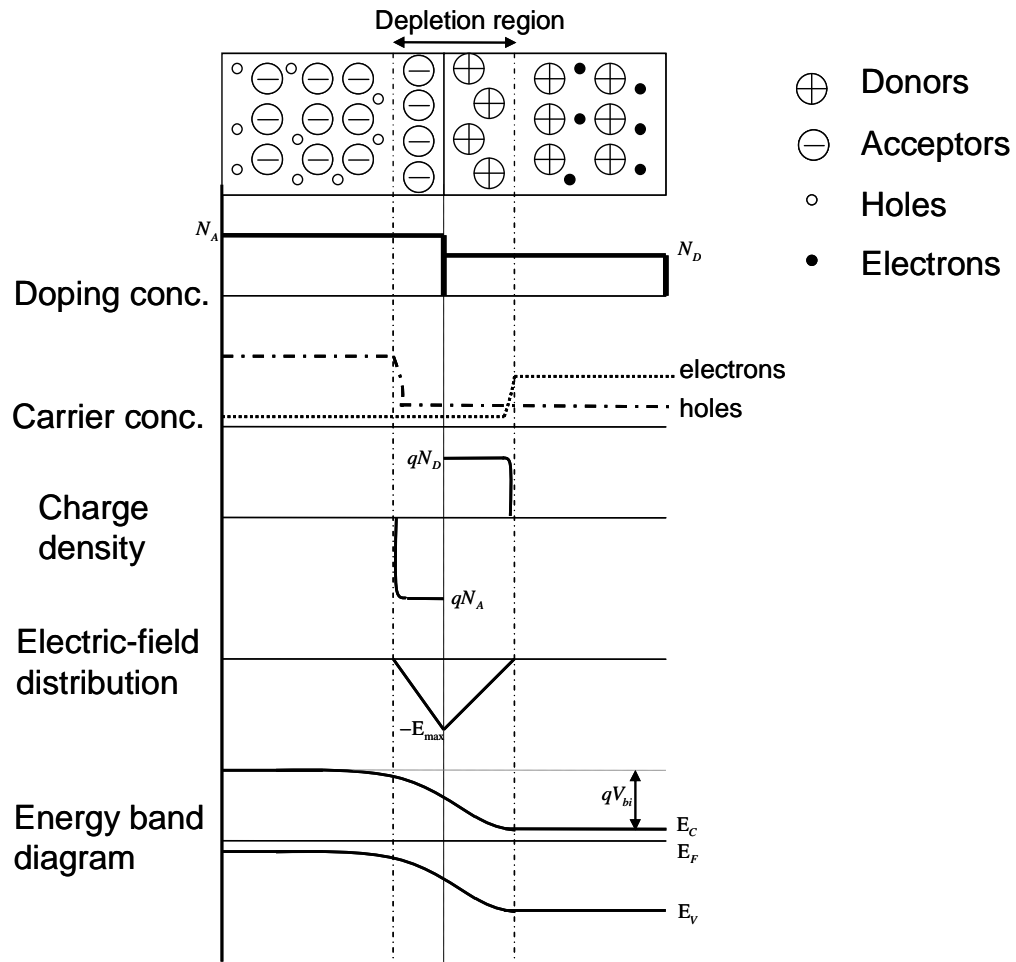


Figure 2-5. Various distributions for a typical uniformly-doped abrupt $p^+ - n$ junction.

2.1.5.1 Reverse Biased Junction

When a p-n junction is reversed biased, the free carriers (electrons in n-type and holes in p-type) will be attracted to the appropriate bias terminals. This rearrangement of carriers will increase the width of the depletion region resulting in an increase of the associated electric field. The current at the junction will therefore be largely reduced. If the reverse voltage is increased the current will decrease to a certain saturation level. This will happen until the junction reaches its dielectric break-down point [7].

2.1.5.2 Forward Biased Junction

On the other hand, if a p-n junction is forward biased, the potential barrier in the depletion region is largely reduced resulting in majority carrier flow across the junction which produces an electrical current that is exponentially proportional to the applied forward voltage. However, the junction terminal has an intrinsic series resistance (R_s) which will cause the current to slow down its exponential behaviour and eventually behave linearly with the applied voltage. The overall series resistance will be the result of the n-type and p-type materials series resistance. This resistance is directly proportional to the resistivity and inversely proportional to the terminal doping of the semiconductors. The diode equation can then be described as [6]:

$$I = I_o \exp\left(\frac{q(V_{app} - IR_s)}{nkT} - 1\right) \quad (2.8)$$

where V_{app} is the applied voltage, k is Boltzmann's constant, I_o is the saturation current and n is the diode ideality factor. $n = 1$ if the ideal diffusion current dominates, however, depending on the number of carriers injected the recombination current may become dominant. In this case, the ideality factor decreases. The ideality factor may also increase if the materials are not of a good quality. Imperfections due to the manufacturing process add to the recombination current and this in turn lowers the ideality factor [8, 9].

2.1.5.3 Intrinsic Capacitances

Under the influence of forward bias, an excess of carriers is injected from one semiconductor to the other. These minority carriers recombine with the existing majority carriers and decay exponentially with distance. However, the carriers within the diffusion length represent stored charge. This charge gives rise to the 'diffusion capacitance'. On the other hand, the capacitance due to the stored charges in the positive and the negative charge regions is called 'depletion capacitance'. Depletion capacitance changes with the applied voltage as the width of the depletion region changes. The smaller the depletion region, the larger the depletion capacitance and vice versa. In the reverse bias condition, negligible charge carriers can be injected

from one material to the other, the diffusion capacitance is negligible and the depletion capacitance dominates [10]. However, under the influence of forward bias, the charge stored within the diffusion lengths increases and so does the diffusion capacitance; therefore, the diffusion capacitance is dominant in forward bias.

2.1.6 Heterojunction Concepts

A heterojunction is defined as a junction formed between two dissimilar semiconductors, such as n-type InP on p-type $\text{In}_{0.53}\text{Ga}_{0.47}\text{As}$ or n-type $\text{Al}_{0.3}\text{Ga}_{0.7}\text{As}$ on p-type GaAs. HBTs are in many ways similar to conventional homojunction bipolar transistors (BJTs) but have unique features compared to BJTs [11]. With the use of heterostructures and by carefully selecting the appropriate band gap and the electric fields, it becomes possible (within limits) to control the forces acting on electrons and holes, separately and independently of each other - a design freedom not rendered by homostructures [12].

In a practical HBT, a wide band gap emitter (e.g. $\text{Al}_{0.3}\text{Ga}_{0.7}\text{As}$, $\text{In}_{0.5}\text{Ga}_{0.5}\text{P}$ or InP) comes in contact with the narrow band gap base (e.g. GaAs or $\text{In}_{0.53}\text{Ga}_{0.47}\text{As}$). The band energy diagram for such an emitter-base (E-B) heterojunction, before and after the two materials are brought into contact, is depicted in Figure 2-6 (a) and (b) respectively.

The energy band gaps of the emitter and the base materials are denoted as E_{gE} and E_{gB} , while E_C and E_V are the energy levels at the conduction and valence bands, respectively. The subscript 'E' and 'B' represent the emitter and base regions respectively. The electron affinity ($q\chi$) is the energy required to remove an electron from the bottom of the conduction band to the vacuum level. Once the junction is formed, thermodynamic equilibrium is attained and the alignment of the fermi level (E_f) occurs for both materials. The difference in the electron affinities of the two materials give rise to a conduction band discontinuity, ΔE_C . Similarly, the difference in the band gap energies of the two semiconductors gives rise to a discontinuity in the valence band, ΔE_V . The difference in the band gap, ΔE_g can be related to the two discontinuities in the conduction and valence band by the following expression [12],

$$\Delta E_g = \Delta E_C + \Delta E_V \quad (2.9)$$

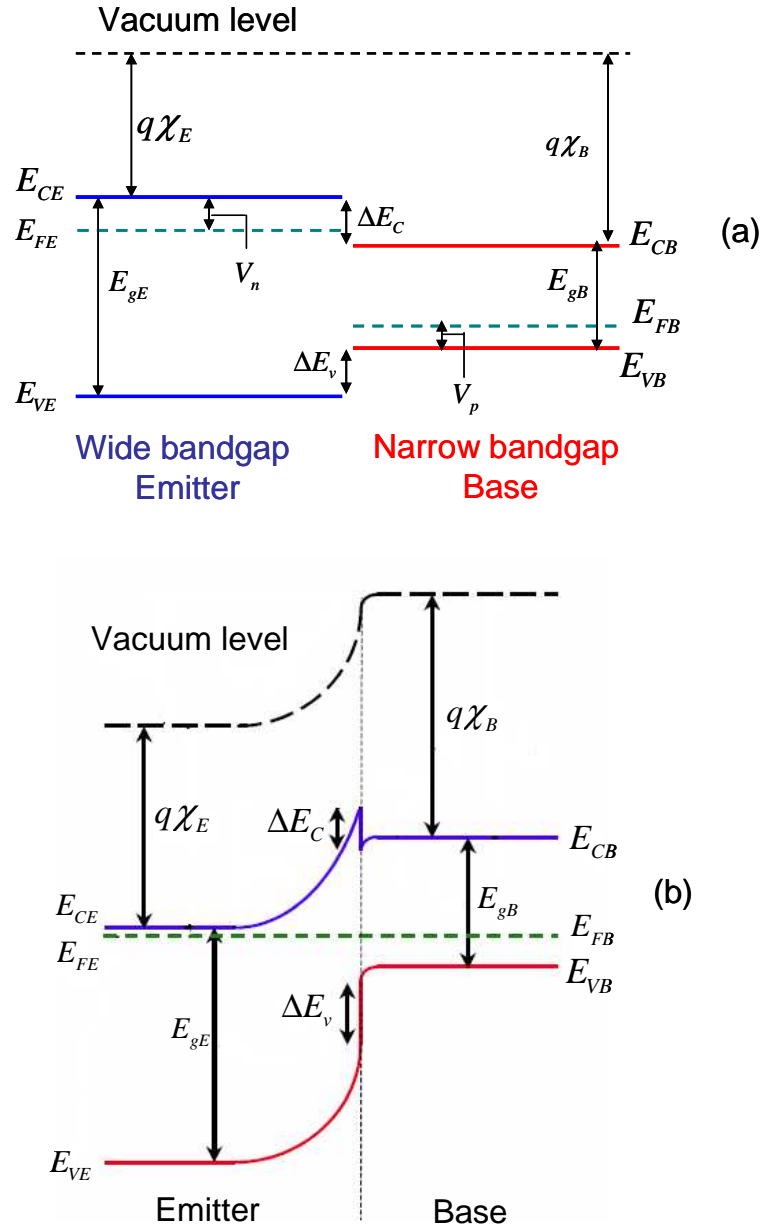


Figure 2-6. Energy band diagram of a wide band gap N-emitter and narrow band gap p-base abrupt heterojunction at thermal equilibrium (a) before and (b) after formation.

2.1.7 Bipolar Junction Transistors

In brief, a BJT is a three layer semiconductor device in which a different doped semiconductor layer is sandwiched between two layers of semiconductor type resulting in an npn or pnp configuration. In practice, for high frequency applications, the npn configuration is preferred to the pnp because electrons are the principal carriers in the npn configuration and the drift velocity of electrons is higher than that of holes [13], yielding better high frequency operation and therefore higher bit rates. For amplification purposes, the transistor has to operate in forward active mode. In this mode, the B-E junction is forward biased and the B-C junction is reversed biased. A detailed mechanism is explained with the help of Figure 2-7.

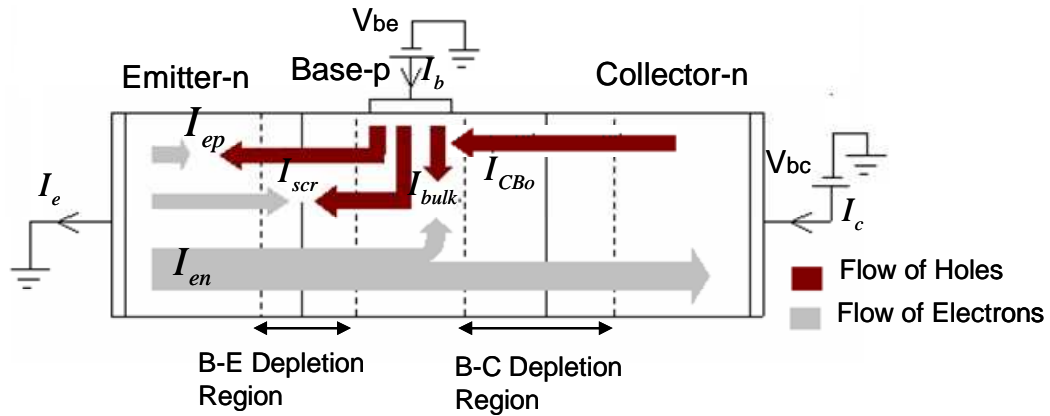


Figure 2-7. Schematic diagram of an npn BJT showing internal current components for emitter ground configuration (adapted from Figure 7-3 in [16]).

The forward biased B-E junction produces an electron current I_{en} , from the emitter to the base, and a hole current (called ‘emitter defect current’ [13]) I_{ep} , into the emitter from the base. I_{en} , then diffuses from the base to collector region through the base collector (B-C) junction. Some of the holes injected into the base region recombine with some of the electrons in the B-E depletion region giving rise to I_{scr} . Some of the electrons from I_{en} will recombine with further holes in the base region generating I_{bulk} . The base width must therefore be designed to be much smaller than the diffusion length of the minority carriers in order for a large proportion of I_{en} to reach

the collector. Finally, some thermally generated hole leakage current (I_{CBo}) flows into the base from reverse B-C junction.

From Figure 2-7, the emitter, base and collector current components can be summarised as follows [14]:

$$\text{Emitter current,} \quad I_e = I_b + I_c \quad (\text{from Kirchhoff's current law}) \quad (2.10)$$

$$\text{Base Current,} \quad I_b = I_{ep} + I_{bulk} + I_{scr} - I_{CBo} \quad (2.11)$$

$$\text{Collector Current,} \quad I_c = I_{en} - I_{bulk} + I_{CBo} \quad (2.12)$$

The common emitter current gain (β) of the transistor is defined as the ratio of collector current to the base current and is written as:

$$\beta = \frac{I_c}{I_b} = \frac{I_{en} - I_{bulk} + I_{CBo}}{I_{ep} + I_{bulk} + I_{scr} - I_{CBo}} \quad (2.13)$$

From (2.13), it is noticeable that the device operation mainly depends on the contribution of I_{en} while other currents are strictly nuisance [15]. If the base thickness is much smaller than the electron diffusion length in the base, then I_{bulk} is very small. The thermal regeneration current contribution I_{CBo} , and space-region recombination current I_{scr} , are small in comparison with I_{en} and I_{ep} respectively, hence they can be ignored in the calculation of the maximum current gain for homojunction transistors. The maximum value of gain is then given as:

$$\beta = \frac{I_{en}}{I_{ep}} \quad (2.14)$$

In terms of current densities, (2.14) is written as:

$$\beta = \frac{J_{en}}{J_{ep}} \quad (2.15)$$

2.1.7.1 Energy Band Diagram

The energy band diagram of an npn transistor working in forward active mode is given in Figure 2-8.

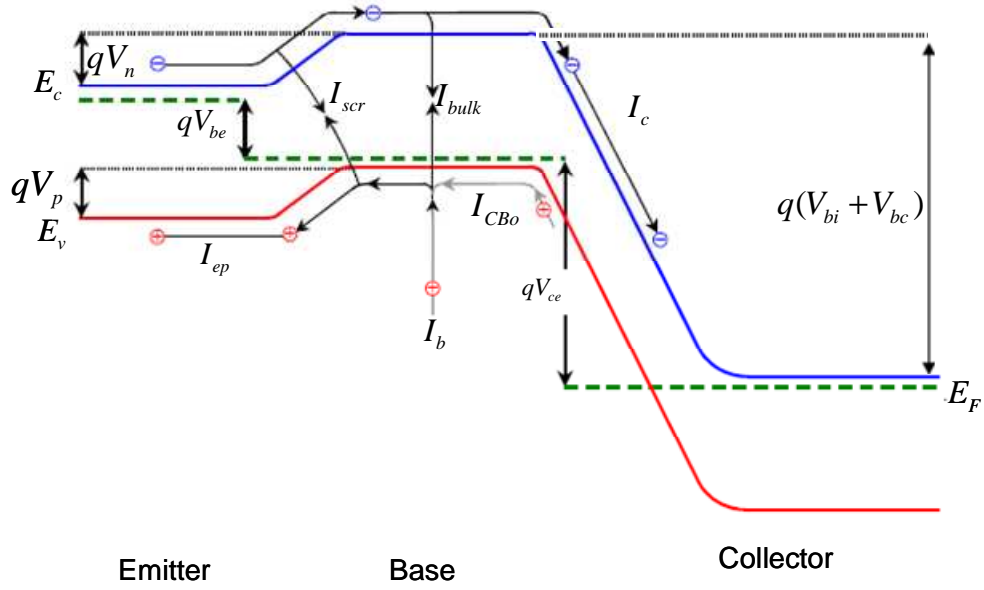


Figure 2-8. Energy band diagram of npn BJT under bias in forward active mode.

where V_n and V_p are the valence and conduction band potential barriers for holes and electrons respectively. Using Boltzmann statistics and Fick's law, the electron current density in the emitter-base ideal junction (J_{EN}) and the hole current density in the base-emitter ideal junction (J_{EP}) are given by (2.16) and (2.17) respectively [5, 7]:

$$J_{EN} = \frac{N_D q D_{nb}}{W_B} \exp\left(\frac{-qV_n}{kT}\right) \quad V_p = V_{bie} - V_{be} \quad (2.16)$$

$$J_{EP} = \frac{N_A q D_{pe}}{L_{pe}} \exp\left(\frac{-qV_p}{kT}\right) \quad V_n = V_{bib} - V_{be} \quad (2.17)$$

where,

V_{bie} = built in potential barrier to electrons in the emitter

V_{bib} = built in potential barrier to holes in the base

D_{nb} = diffusion constant of electrons in the base

D_{pe} = diffusion constant of holes in the emitter

N_D = donor concentration in emitter

N_A = acceptor concentration in base, and

L_{pe} = diffusion length of holes in emitter.

Consequently, the current gain can be obtained from (2.16) and (2.17) as:

$$\beta = \frac{I_{EN}}{I_{EP}} = \frac{J_{EN}}{J_{EP}} = \frac{N_D D_{nb} L_{pe}}{N_A D_{pe} W_B} \exp\left(\frac{q}{kT}(V_p - V_n)\right) \quad (2.18)$$

In homojunctions, $V_n = V_p$ as the semiconductor for the base, collector and sub-collector layers is the same in BJT's. Therefore:

$$\beta_{Homo} = \frac{N_D D_{nb} L_{pe}}{N_A D_{pe} W_B} \quad (2.19)$$

In order to maximize the current gain, the emitter has to be highly doped and the base doping should be low. The physical width of the base should also be kept low to minimize the recombination in the base region. In the forward active mode, the B-C junction is reversed biased and if the base region is lowly doped, the base space charge region increases excessively, and the electrons reach the base faster, avoiding bulk recombination. This phenomenon is referred to as base width modulation and is undesirable as it causes a slight increase in the collector current with increasing C-E voltage, resulting in nonlinear amplification in transistors [9].

2.1.7.2 Small Signal Equivalent Model

In order to obtain the frequency response in BJTs, a small-signal equivalent circuit is studied. The structure of the BJT presents depletion and diffusion capacitances in the BE and BC junctions. In addition to these capacitances, each layer has its own series resistance. When an ideal transistor is biased in active mode, the collector current (i_c) is related to V_{be} by (2.20) [6]:

$$i_c = i_{co} \exp\left(\frac{qV_{be}}{n_c kT}\right) \quad (2.20)$$

where n_c is the collector ideality factor. We can use this to calculate the transconductance (g_{mo}) of the transistor, which is defined as [6]:

$$g_{mo} = \left. \frac{\partial i_c}{\partial V_{be}} \right|_{V_{ce} = \text{const.}} = \frac{q}{kT} i_c \quad (2.21)$$

Similarly, the input conductance (g_{be}) can be calculated by differentiating the base current (i_b) with respect to the base-emitter voltage (V_{be}) and then substituting the base current. The input conductance is given by (2.22):

$$g_{be} = \left. \frac{\partial i_b}{\partial V_{be}} \right|_{V_{ce}=\text{const.}} = \frac{q}{kT} i_b = \frac{1}{r_{be}} \quad (2.22)$$

Finally, the high frequency equivalent circuit incorporating all the above elements is given by Figure 2-9.

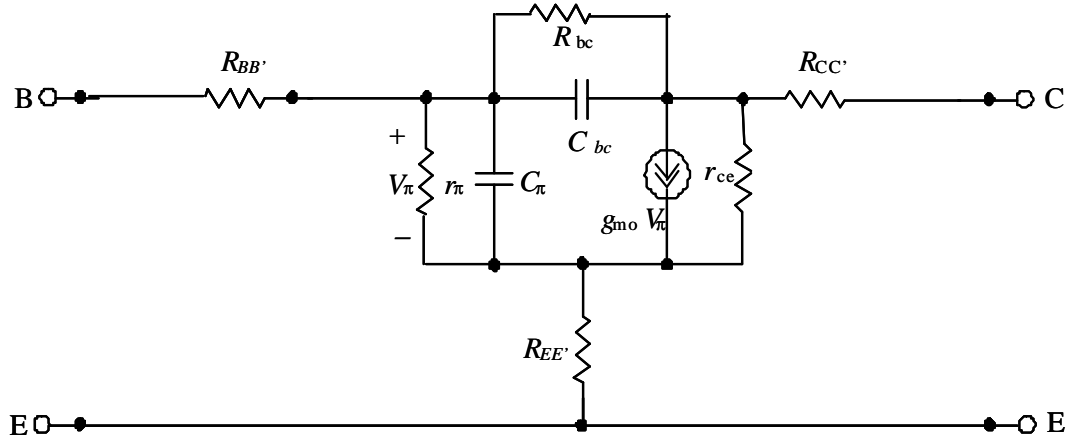


Figure 2-9. Small-signal π - equivalent circuit for BJT at high frequency in common emitter configuration.

where, $C_\pi = C_{dep} + C_{diff}$ and $C_{diff} = g_m \tau_f$, τ_f being the forward transit time. $R_{BB'}$, $R_{CC'}$ and $R_{EE'}$ are the associated series resistances for base, collector and emitter respectively. Using the small signal parameters, the cut-off frequency (f_t) of a device can be found. f_t is the frequency at which the short circuit current gain, h_{21} drops to unity which is given by (2.23) [6]:

$$f_t = \frac{g_m}{2\pi(C_\pi + C_{bc})} \quad (2.23)$$

While the unity gain frequency, f_t , is an important Figure of merit of a bipolar transistor, another important Figure of merit is the maximum oscillation frequency (f_{max}). This Figure of merit predicts the unity power gain frequency and indicates the

maximum frequency at which useful power gain can be expected from a device. The maximum oscillation frequency is linked to f_t and is obtained from (2.24) [7].

$$f_{\max} = \left[\frac{f_t}{8\pi R_{BB'} C_{bc}} \right]^{\frac{1}{2}} \quad (2.24)$$

From (2.24), it can be seen that f_{\max} depends heavily on the intrinsic base resistance; therefore, the doping in the base should be high. However, high base doping decreases the current gain as shown in (2.19). Similarly, in order to obtain high gain, an increase in the emitter's doping will cause a high emitter-base capacitance, again limiting the high frequency of the device.

The solution to these BJT doping concentration problems is a BE heterojunction. This allows an increase in the base doping and reduction in the emitter doping without affecting the frequency response of the device.

2.1.8 Heterojunction Bipolar Transistors

It is evident from (2.13) that I_{ep} is undesirable and a mechanism must be developed to reduce this unwanted motion of holes from the base to the emitter. This can be achieved through heterostructures. HBTs are bipolar junction transistors which are composed of at least two different semiconductors. As a result, the energy band gap and other material properties can be different in the emitter, base and collector. The single-HBT (sHBT) consists of a wide band gap emitter and a narrow band gap base and collector. The current transport mechanism in the sHBT is the same as in the BJT, however, the energy gap variations act on electrons and holes to control their distribution and flow, resulting in higher speed and higher frequency capability. Moreover, a gradual change or 'grading' of the material is possible within each region which removes the conduction band spike and yields smooth monotonically varying band edges [16]. The energy band diagram of a compositionally graded HBT with a discontinuity in the valence band is shown in Figure 2-10.

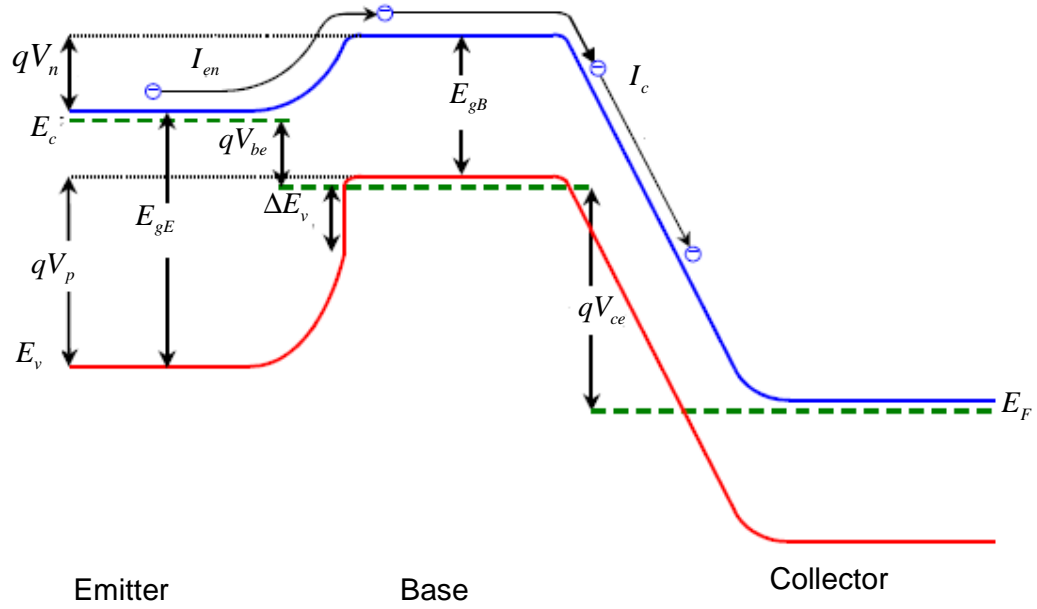


Figure 2-10. Energy band diagram of a graded Npn HBT in forward active mode.

Here, qV_n and qV_p are the potential energy barriers heights for electrons and holes respectively in B-E junction. In this case (2.18) can be rewritten as [16]:

$$\beta = \frac{N_D D_{nb} L_{pe}}{N_A D_{pe} W_B} \exp\left(\frac{\Delta E_g}{kT}\right) \quad (2.26)$$

ΔE_g is in the exponential and controls the value for the current gain. A heterojunction can therefore provide us with the freedom to adjust the doping levels in the base and emitter without compromising the injection efficiency and still provide adequate gain [3]. The base doping can now be significantly larger than for BJTs and thus performance is enhanced for both the high frequency and DC aspects. However, the large injection efficiency does not necessarily imply that the large value of current gain is attainable. It simply implies that the backward hole injection becomes a negligible part of the base current compared to the other two recombination currents. Therefore, (2.10) can be modified as:

$$I_b \cong I_{bulk} + I_{scr} \quad (2.27)$$

The gain will also change as a result of the change in base current. Since $I_{en} \gg I_{bulk}$, and I_c can be approximated as I_{en} , (2.13) can be written as:

$$\beta = \frac{I_{en}}{I_{bulk} + I_{scr}} \quad (2.28)$$

Thus, by comparing (2.13) and (2.28), it can be seen that heterojunction transistors can provide better current gain in contrast to homojunction phototransistors.

In abrupt heterojunction transistors, a discontinuity is present at the emitter-base interface. One major disadvantage in this type of structure is the presence of ΔE_c in the base conduction band. This discontinuity will tend to collect the injected electrons, enhancing the recombination losses at the junction and reducing the gain [15]. This also adds to a potential barrier for the electrons from emitter to base and thus reduces the I_{en} / I_{ep} ratio, which is detrimental to the gain.

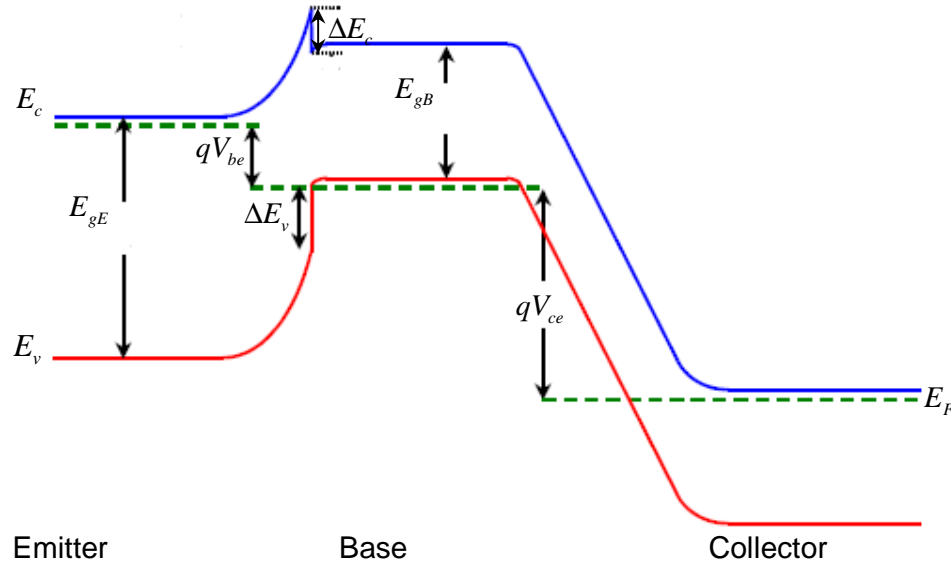


Figure 2-11. Energy band diagram of an abrupt-junction Npn HBT in forward active mode.

Figure 2-11 shows the energy band diagram of an abrupt Npn HBT with a notch in the conduction band due to ΔE_c . This is undesirable and can be removed by grading

the junction properly or by proper choice of materials as well. If materials are chosen properly (lattice matched), grading might not even be required.

2.1.9 HBT Material Systems

In HBTs, a large ΔE_c is undesirable since it provides an extra barrier to electron injection from the emitter to the base thereby requiring a larger emitter-base forward bias voltage. This ultimately lowers the emitter injection efficiency, limiting the device current gain for a HBT. By the same analogy, a large ΔE_v is advantageous as it limits the reverse injection of holes from the base into the emitter. Table 2.1 lists some of the band discontinuities of various HBT material systems [11, 12, 17].

Material structure	E_{g1} (eV)	E_{g2} (eV)	ΔE_c (eV)	ΔE_v (eV)	ΔE_g (eV)
$Al_{0.3}Ga_{0.7}As / GaAs$	1.86	1.42	0.28	0.15	0.43
$In_{0.5}Ga_{0.5}P / GaAs$	1.92	1.42	0.12	0.38	0.5
$InP / In_{0.53}Ga_{0.47}As$	1.35	0.76	0.25	0.34	0.59
$In_{0.52}Al_{0.48}As / In_{0.53}Ga_{0.47}As$	1.20	0.76	0.32	0.12	0.44
$In_{0.5}Al_{0.5}P / GaAs$	2.35	1.42	0.31	0.62	0.93
$Si / Si_{0.75}Ge_{0.25}$	1.12	0.97	0.02	0.13	0.15

Table 2.1: Band discontinuities for various HBT material heterostructures.

2.1.9.1 $Al_{0.3}Ga_{0.7}As / GaAs$ HBTs

Among all the HBT material systems, $Al_{0.3}Ga_{0.7}As/GaAs$ HBTs have been widely studied and have also demonstrated good high frequency performance [18-20]. However, Table 2.1 shows that most of the band gap discontinuity is due to the conduction band offset which reduces the emitter injection efficiency. Although, this problem can be solved by grading the emitter-base junction, this has some drawbacks in the form of scattering centres resulting in larger recombination current [21]. In

addition, Al in $\text{Al}_{0.3}\text{Ga}_{0.7}\text{As}/\text{GaAs}$ HBTs generates DX centres, increasing the recombination currents further and therefore reducing the current gain [22].

2.1.9.2 $\text{In}_{0.5}\text{Ga}_{0.5}\text{P}/\text{GaAs}$ HBTs

$\text{In}_{0.5}\text{Ga}_{0.5}\text{P}/\text{GaAs}$ material system has the most desirable band alignment out of the III-V compounds shown in Table 2.1 because most of the discontinuity in the band structure is in the valence band which limits back injection of holes into the emitter. At the same time, the conduction band discontinuity is relatively small which increases the emitter injection efficiency without the need for grading. This improves the current gain of the device. The problems related to DX centres in $\text{Al}_{0.3}\text{Ga}_{0.7}\text{As}$ are not present in $\text{In}_{0.5}\text{Ga}_{0.5}\text{P}$ making it more useful as an emitter. Furthermore, a lower surface recombination velocity and the existence of highly selective wet and dry etch chemistries for the $\text{In}_{0.5}\text{Ga}_{0.5}\text{P}/\text{GaAs}$ material system are among the other advantages of $\text{In}_{0.5}\text{Ga}_{0.5}\text{P}$ over $\text{Al}_{0.3}\text{Ga}_{0.7}\text{As}$ [22].

2.1.9.3 $\text{InP}/\text{In}_{0.53}\text{Ga}_{0.47}\text{As}$ HBTs

InP based HBTs are attractive due to their compatibility with optical sources and detectors in optoelectronic integrated circuit applications. The smaller band gap of $\text{In}_{0.53}\text{Ga}_{0.47}\text{As}$ (0.75 eV), compared to that of GaAs (1.42 eV) means that a lower base emitter voltage is required for operation resulting in a low power consumption for these devices, which is advantageous for low power applications [23, 24]. Furthermore, HBTs with an $\text{In}_{0.53}\text{Ga}_{0.47}\text{As}$ base have higher peak electron velocity and lower surface recombination velocity compared to GaAs-based HBTs [25]. These devices have a larger valence band offset when compared to the conduction band which allows high injection efficiency with high base doping. $\text{In}_{0.53}\text{Ga}_{0.47}\text{As}$ is also lattice matched to InP and therefore no grading of the B-E junction is required to remove the potential spike to improve the emitter injection efficiency.

One major problem associated with $\text{InP}/\text{In}_{0.53}\text{Ga}_{0.47}\text{As}$ HBTs is very low C-E breakdown voltage, typically about 2.5 V. This problem is less severe in DHBTs where a wide band gap collector is used [26, 27].

2.1.9.4 $In_{0.52}Al_{0.48}As/In_{0.53}Ga_{0.47}As$ HBTs

HBTs composed of $In_{0.52}Al_{0.48}As/In_{0.53}Ga_{0.47}As$ have demonstrated excellent potential for high speed operation in digital and analog applications [28, 29]. A higher value of conduction band offset, compared to valence band offset, implies that this material system will have low emitter injection efficiency. On the other hand, a large ΔE_C enables high energy electron injection into the base, decreasing the base transit time [17] and resulting in high frequency operation and high bit rates. In order to reduce ΔE_C , grading can be used to provide better emitter injection efficiency [30]. Another technique to overcome this problem is the introduction of an $In_{0.53}Ga_{0.47}As$ spacer layer between the emitter and base [28].

2.1.9.5 $In_{0.5}Al_{0.5}P/GaAs$ HBTs

The $In_{0.5}Al_{0.5}P/GaAs$ material system is suitable for HBTs due to one of the largest values of ΔE_V , seen in any material, namely 0.62 eV. This provides excellent reduction of back injection of holes from the base to the emitter. A ΔE_C of 0.31 eV ensures good emitter injection efficiency and produces high current gains. High etching selectivity to GaAs, during the fabrication process, is another important advantage of $In_{0.5}Al_{0.5}P$. Both sHBT and DHBT configurations have been reported [17] for this material system.

2.1.9.6 $Si/SiGe$ HBTs

The $Si/SiGe$ structure looks the most interesting since it has near ideal band discontinuities for a HBT. A high current gain can therefore be achieved from these devices. Since Si has been firmly established and its material properties have been well understood, this technology has been converted to use for $Si/SiGe$ HBTs. However, it is important to mention that the mobility of Si ($\mu_n = 1400 \text{ cm}^2 / \text{Vs}$) and silicon based devices is lower than other materials like InP ($\mu_n = 5400 \text{ cm}^2 / \text{Vs}$), making it less suitable for high frequency devices. Due to the narrow band gaps of both Si and Ge, they are not very suitable for high temperature and high power applications [17]. Nevertheless, a very high gain can be expected from $Si/SiGe$ -based HBTs [31, 32].

2.1.10 Wavelength Sensitivity of Various Material Systems

Regarding wavelength sensitivity of these materials, $\text{In}_{0.5}\text{Ga}_{0.5}\text{P}$ and AlGaAs have band gap of 1.92 eV and 1.86 eV respectively. They are transparent to optical communication wavelengths of 850 nm (1.38 eV), 1300 nm (0.95 eV), and 1550 nm (0.8 eV). If the emitter is made of one of these materials then it will be transparent to the optical signal and most of the optical energy will go through the emitter towards the base without being absorbed. GaAs has a band gap of 1.42 eV, making it sensitive to incident electromagnetic radiation of 800 nm. Therefore, GaAs -based devices are suitable for short-wavelength optical detection. Early optical detectors were based on Si which is also sensitive to wavelengths from 800 nm to 900 nm and is compatible with $\text{AlGaAs}/\text{GaAs}$ lasers and LEDs. However, Si is an indirect band gap material resulting in low conversion efficiency as some of the optical energy is converted and dissipated as heat to the lattice structure.

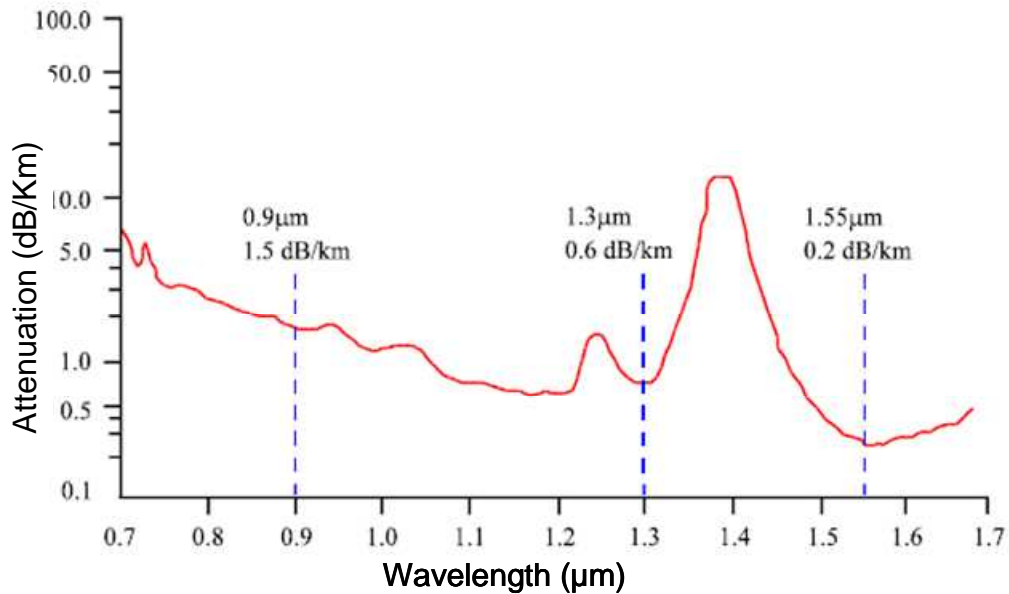


Figure 2-12. Loss Characteristics of a Silica Optical Fiber showing the three wavelengths of interest. After [23].

From the point of view of telecommunication applications, the wavelength window that provide lowest attenuation is 1550 nm and is used in long haul optical links [33]. Therefore HPTs that detect long wavelengths are desirable; these must have a base-

collector band gap of 0.8 eV. InP/ In_{0.53}Ga_{0.47}As lattice matched HPT systems come into contention because of the collector band gap of 0.75 eV which is sensitive to both the 1300 nm and 1550 nm wavelengths. These wavelengths correspond to the low loss windows of optical fibres and have been used for long haul optical fibre telecommunications. Apart from the high current driving capacity of InP/In_{0.53}Ga_{0.47}As HBTs, the material compatibility allows monolithic integration with other optoelectronic devices [34].

2.2 Photodetection

Optical detection is the conversion of optical (light) energy to electrical energy (current). Photodetectors in optical communication systems sense the incident optical power and convert the variation in the optical power into a corresponding varying electric current. In order for a semiconductor device to be useful as a photodetector, some property of the device should be affected by optical radiation. The most commonly used property is the conversion of light into electron-hole pairs that can be detected in a properly chosen circuit.

Photodetection involves electron excitation from the valence band to the conduction band and is referred to as intrinsic absorption, while those excitations involving impurity centres within the material are known as extrinsic absorption. However, due to its associated efficiency and fast response it is the former process which is of general interest. For intrinsic transitions possible near the band edge for direct band gap semiconductors such as GaAs and In_{0.53}Ga_{0.47}As, the absorption coefficient is given by (2.29) [2, 6].

$$\alpha(h\nu) \cong 3 \times 10^6 \left(\frac{m_n^*}{m_o} \right)^{(3/2)} \left[\frac{(h\nu - E_g)^{(1/2)}}{h\nu} \right] (\text{cm}^{-1}) \quad (2.29)$$

The absorption coefficient is zero above a cut-off wavelength given by λ_c . λ_c is shown in (2.30).

$$\lambda_c (\mu\text{m}) = \frac{hc}{E_g} = \frac{1.24}{E_g (\text{eV})} \quad (2.30)$$

The absorption coefficients for the two materials are shown as a function of wavelength in Figure 2-13. The detailed absorption aspects and their variation with carrier concentration is described in section 4.1. However, it is useful to establish that the absorption is wavelength dependent and beyond the cut-off wavelength the absorption is negligible. The cut-off wavelength of GaAs is about 870 nm and for $\text{In}_{0.53}\text{Ga}_{0.47}\text{As}$ it is 1550 nm as seen from Figure 2-13.

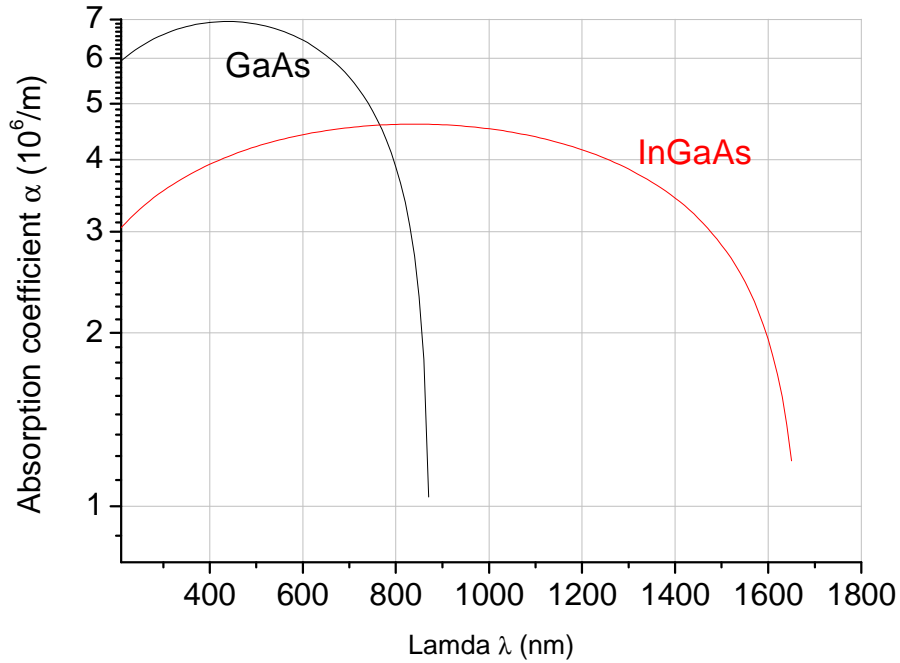


Figure 2-13. Absorption coefficient for $\text{In}_{0.57}\text{Ga}_{0.43}\text{As}$ and GaAs as a function of incident wavelength.

2.2.1 Photodiodes

Photodiodes are frequently used in a variety of applications, including optical communications, isolation, and motion detection and control. A photodiode is constructed by doping a semiconductor material to form a p-n junction. When a photon of sufficient photon energy strikes the diode, it may excite an electron thereby creating a mobile electron and a positively charged hole. If the photoabsorption occurs in the junction's depletion region, or one diffusion length away from it, these carriers are swept from the junction by the built-in field of the

depletion region, producing a photocurrent [2]. The semiconductor materials commonly used are silicon, indium, aluminium, gallium, and arsenic. Depending upon the process and materials used, photodetectors can be optimized for any part of the spectrum from ultraviolet to infrared. Photodiodes are packaged in such a way as to focus the incoming light through a lens, and occasionally through an optical filter, directly onto the diode junction. The photons in the incident light break covalent bonds in the depletion region, producing electron-hole pairs that are swept across the junction by the electric field imposed by the external bias circuit. The resulting current is proportional to the intensity of the incoming light [35]. Modelling the photodiode as an RC circuit is common practice, as is shown in Figure 2-14.

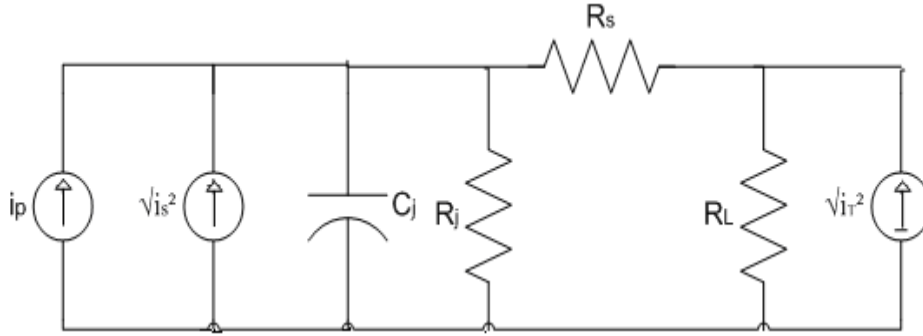


Figure 2-14. Equivalent circuit of a photodiode

Here C_j is the junction capacitance, R_j is the junction resistance, R_s is the series resistance and R_L is the external load resistor. I_p is the photogenerated current which is given by [35]:

$$I_p = \frac{q\eta P_{opt}}{h\nu} \quad (2.31)$$

where P_{opt} is the average optical power and η is the quantum efficiency. h , ν and q have their usual meanings of Planck's constant, frequency and electron charge respectively. i_s is the shot or white noise which is frequency independent, has a Gaussian distribution and is given as a mean value in the circuit which is given as [35]:

$$\langle i_s^2 \rangle = 2q(I_p + I_b + I_d)B \quad (2.32)$$

where B is the bandwidth of the measurement. Shot noise is caused by background radiation (I_b), the dark current (I_d), and noise from photocurrent itself. The thermal Johnson noise i_t due to the random movement of the carriers in the resistive elements is given by (2.33) [35]:

$$\langle i_t^2 \rangle = 4KT(1/R_L)B \quad (2.33)$$

2.2.1.1 Factors limiting the Speed of Photodiodes

The speed of a photodetector depends on the following factors:

- Diffusion of carriers
- Drift transit time in the depletion region
- Capacitance of the depletion region.

The slowest or the bottleneck of the three processes is the diffusion of carriers to the high electric field depletion region from outside that region. To minimize this slow effect, carriers should be generated near or in the depletion region. The second process, transit time, is the time required for the carriers to drift across the depletion region and get swept out of the device. With sufficient reverse bias, these carriers will drift at their saturation velocities, on the order of 3×10^6 cm/s for GaAs. Lastly, the capacitance of the device will determine its RC time constant, where R is the load resistance (usually 50 Ω). To maximize photodiode response, the transit time is typically designed to be comparable to the RC time constant [35].

If the depletion region is thick, a high number of photocarriers will be generated; however, the transit time will limit the frequency response of the photodetector. On the other hand, if the depletion region is kept thin, the capacitance of the junction will increase resulting in the reduction of f_t . Similarly, if the carriers are generated away from the high electric field (depletion) region, there will be an additional time delay experienced by the carriers that diffuse in the depletion region. Thus materials, dimensions and the mode of operation play a very important role in modelling the responsivity and the frequency response of photodetectors.

2.2.1.2 Common Types of Photodiodes

The most common type of photodiodes are p-i-n, avalanche photodiodes (APD) and Schottky photodiodes.

2.2.1.2.1 p-i-n Photodiodes

p-i-n photodiodes are diodes with a wide, undoped or a slightly-doped intrinsic semiconductor region between p-type and n-type semiconductor regions. The electrical conductivity of the photodiode is a function of the signal intensity, wavelength, and the modulation rate of the incident radiation [6]. The depletion region of a p-i-n photodiode exists almost completely within the intrinsic region, which is a constant width (or almost constant) regardless of the reverse bias applied to the diode. This intrinsic region can be made large, increasing the area where electron-hole pairs can be generated. Figure 2-15 shows the cross-section and operation of a p-i-n photodiode [5]. The photogeneration occurs in the depletion region if the energy of the incoming signal is greater than the band gap of the material. The resulting photogenerated electron-hole pair is separated by the depletion layer. However, if this does not occur fast enough, electron-hole pair recombines. For the forward bias circuit, the electrons are swept into the p-type and holes into the n-type and in order to maintain the charge neutrality carriers are injected through the bias circuit. One extra electron flows in the bias circuit for every photon absorbed in the depletion region or within a diffusion length [10].

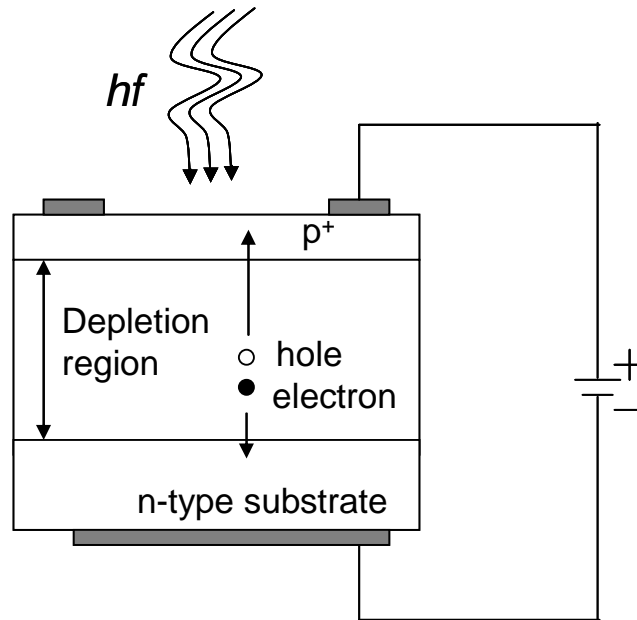


Figure 2-15. Cross-sectional view of a p-i-n photodiode.

2.2.1.2.2 Schottky Photodiodes

A Schottky diode uses a metal-semiconductor junction as a Schottky barrier instead of a semiconductor-semiconductor junction as in conventional photodiodes. This Schottky barrier results in both very fast switching times and low forward voltage drop. The Schottky diode is a ‘majority carrier’ semiconductor device. This means that if the semiconductor body is doped n-type, only the n-type carriers (mobile electrons) play a significant role in the operation of the device. Hence there is no slow component associated with minority carrier effects in the p⁺ region of a p-i-n photodiode [36]. The majority carriers are quickly injected into the conduction band of the metal contact on the other side of the diode to become free moving electrons. The most evident limitations of Schottky diodes are the relatively low reverse voltage ratings and relatively high reverse leakage current resulting in a thermal stability issue.

2.2.1.2.3 Avalanche Photodiodes

In the avalanche photodiodes the free electrons and holes created by absorbed photons accelerate, gaining several electron volts of kinetic energy. Collisions of these fast carriers with neutral atoms cause the other electrons to break out of the valence shell. The electron-hole pairs generated as a result of collision ionization are called secondary carriers. As the primary carriers create secondary carriers, the secondary carriers themselves accelerate and create new carriers resulting in a chain reaction referred to as avalanche-multiplication. APDs require high-voltage power supplies for their operation [37] and add to circuit complexity. APDs are very temperature sensitive, further complicating circuit requirements, and are always less reliable than p-i-n photodetectors.

2.2.2 *Heterojunction Phototransistors*

In phototransistors, most of the radiation falls upon the emitter and the base. In order to generate photocurrent, the radiation has to reach the base-collector depletion region. If the emitter is wide-band gap compared with the radiation wavelength, radiation goes unattenuated through the emitter towards the base. This incident radiation gets absorbed in the base and base-collector region resulting in photo-generated electron-hole pairs. The depletion-layer serves to separate the photo-generated electron-hole pairs. However, if this does not occur fast enough (generally for the carriers generated outside the diffusion lengths), the carriers recombine which in turn destroys electron-hole pairs. This energy is released in the form of heat (for direct band gap) or heat/light (for indirect band gap) materials. HPTs work in a forward active mode in which B-C junction is reverse biased and the B-E junction is forward biased. The electron-hole pair generated, for photons absorbed in the B-C depletion region or within the diffusion length, will effectively add to the I_{CBo} component of the base current (Figure 2-7). The ratio of photogenerated current (I_{ph}) to incident optical power (P_{opt}) is the responsivity (R) of the detector. It indicates how well the optical signal is converted into an electrical signal which can be given as:

$$R = \frac{I_p}{P_{opt}} \quad (2.34)$$

Quantum efficiency (η_q) is the ratio of number of electrons generated per second to the number of incident photons per second and it is given by (2.35).

$$\eta_q = \frac{I_p / q}{P_{opt} / E_{ph}} \quad (2.35)$$

where E_{ph} is the energy of a photon, given as:

$$E_{ph} = \frac{hc}{\lambda} \quad (2.36)$$

Substituting (2.34) and (2.36) into (2.35) gives (2.37).

$$\eta_q = R \frac{hc}{\lambda q} \quad (2.37)$$

This shows that the quantum efficiency is directly proportional to the responsivity of the detector for a given wavelength. The internal gain is achieved through the normal transistor action whereby the optical signal absorbed affects the base current (in three terminal orientation) or generates a virtual base current (two-terminal devices). Figure 2-16 shows the flow of photo-generated electrons and holes in the depletion region for a AlGaAs/GaAs HPT. It also shows the experimental setup of HBTs under illumination when input base current is added.

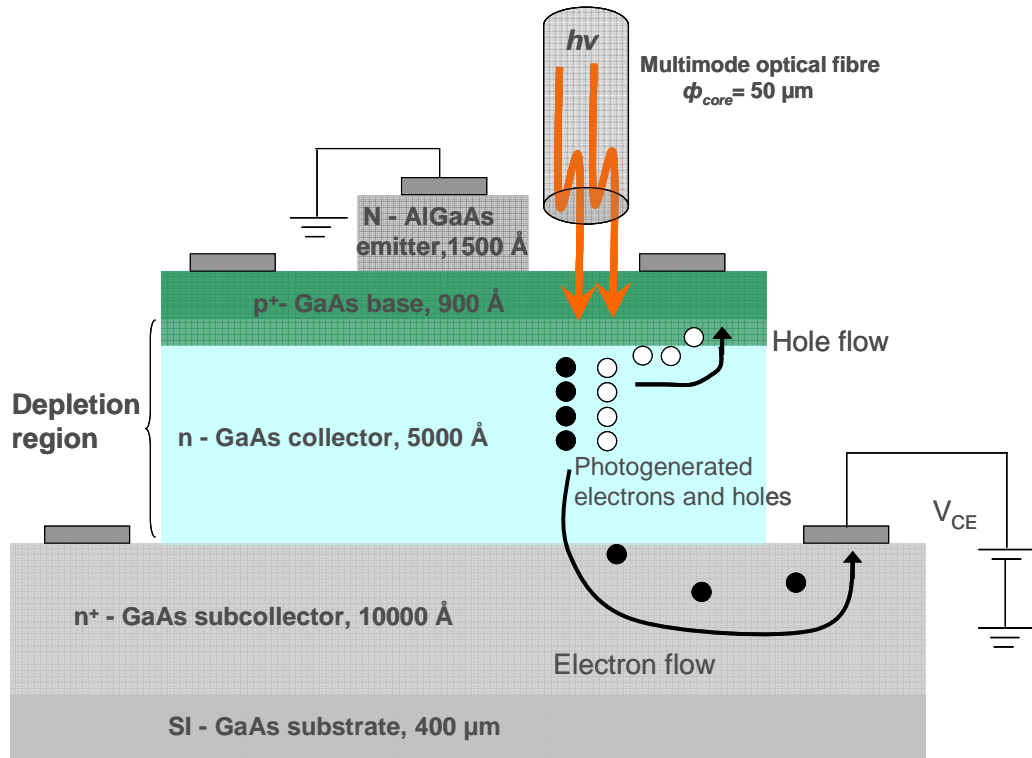


Figure 2-16. Cross-sectional view of the HPT in forward active mode under illumination.

From Figure 2-16, it is clear that absorption occurs in the base, base collector and collector region. The absorbed optical signal gives rise to an optical current (I_p). Under the active common-emitter operation, B-C is reversed biased and the photocurrent adds to the reverse leakage current to the base. So, the production of photocurrent in the base is amplified by internal transistor gain. It can be seen that the absorption process is similar to p-i-n detection but the phototransistor has an inherent current gain which gives rise to the amplification of photocurrent unlike ordinary p-i-n diodes.

2.2.2.1 Two-Terminal HPT

In the absence of any electrical contact at the base, the arrangement is referred to as 2T-HPT. Incident light at the base terminal provides a steady bias current for the transistor. The frequency operation of 2T- HPT is degraded as compared to corresponding 3T-HBT operation. At low incident power, the optical gain of the

HPT is generally small due to recombination at the base-emitter heterojunction, resulting in a small collector current, which in turn results in a longer charging time for the junction capacitance. Consequently, the gain-bandwidth product f_t is small [38]. The 2T arrangement is shown in Figure 2-17.

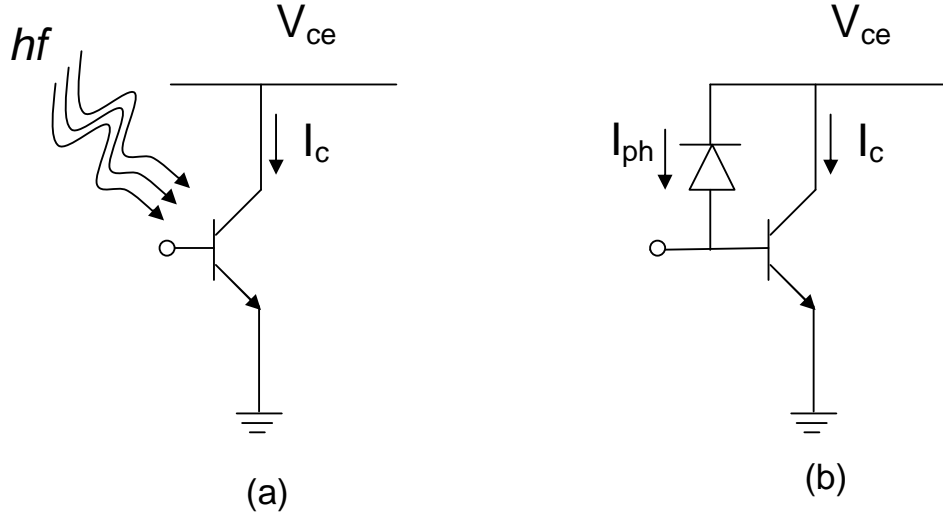


Figure 2-17. 2T HPT Configuration

In Figure 2-17(a), the transistor is working in the forward active mode with base current provided by the incident photonic radiation. Figure 2-17(b) is the equivalent electrical model for Figure 2-17(a) with I_p as the photo-generated base current. The current flow in the 2T-HPT can be discussed with the help of Figure 2-18.

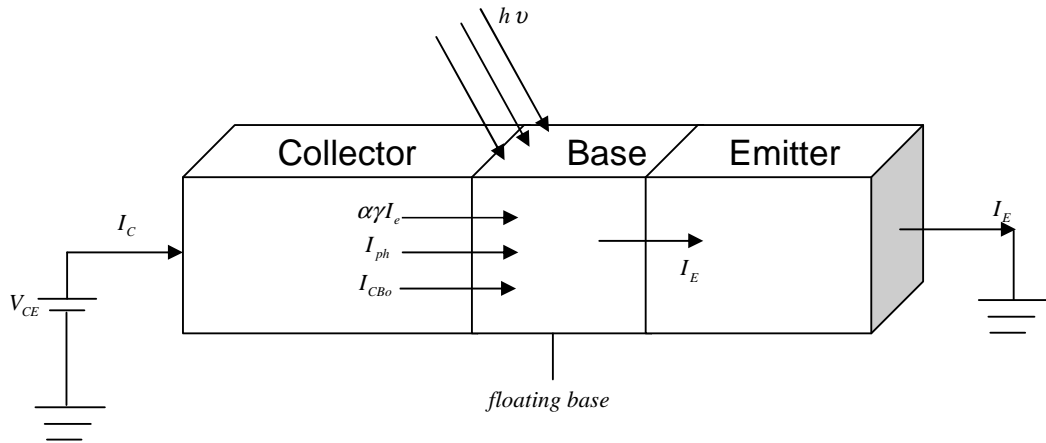


Figure 2-18. Current flowing in a 2T-HPT under illumination.

Recalling (2.10) and making reference to Figure 2-18, it can be seen that some of the original I_{en} is lost due to recombination in the depletion region and in the base bulk.

The fraction of this current that reaches the collector (fr_c) can be written as:

$$fr_c = \alpha' \gamma I_{en} \quad (2.38)$$

where, γ is the emitter injection efficiency and α' is the base transport factor. The fraction of this current that gets absorbed in the base (fr_b) can be expressed as:

$$fr_b = I_{en} - fr_c = (1 - \alpha' \gamma) I_{en} \quad (2.39)$$

The hole current entering the base is a combination of I_{CBo} and I_{ph} . In order to maintain charge neutrality, this hole current should be equal to the fraction of emitter current absorbed in the base. This gives:

$$I_{CBo} + I_{ph} = (1 - \alpha' \gamma) I_e \quad (2.40)$$

Since the transistor is working in the two-terminal configuration, the measured current in the emitter will be equal to the magnitude of the electron flow injected from the emitter into the base. Thus, we can replace I_e for I_{en} in (2.40). From Figure 2-18, the collector current I_c can be expressed as:

$$I_c = I_{CBo} + I_{ph} + \alpha' \gamma I_e \quad (2.41)$$

Substituting (2.40) into (2.41), the collector current can be written as:

$$I_c = I_{CBo} + I_{ph} + \frac{\alpha' \gamma}{1 - \alpha' \gamma} (I_{CBo} + I_{ph}) \quad (2.42)$$

where $\frac{\alpha' \gamma}{1 - \alpha' \gamma}$ is the current gain of the transistor [15], so (2.42) becomes:

$$I_c = \beta (I_{CBo} + I_{ph}) + I_{CBo} + I_{ph} \quad (2.43)$$

Note that when no incident radiation is present, the dark current will also be amplified by the gain of the transistor. This shows that phototransistors are inherently noisy. The optical gain, G_{2T-HPT} is given by [39]:

$$G_{2T-HPT} = \beta \eta_{BC} \quad (2.44)$$

where η_{BC} is quantum efficiency of the base-collector gathering layer.

The responsivity can then be given as [6, 39]:

$$R_{2T-HPT} = \beta R_{BC} \quad (2.45)$$

where R_{BC} is the responsivity of the base-collector junction.

2.2.2.2 Three-Terminal HPT

If an input base current is added to the incident optical energy, the arrangement is known as 3T-HPT. This arrangement improves the optical gain and the frequency response of the HPT's when used as photodetectors [38, 40]. However, it increases the shot noise which degrades the signal-to-noise ratio [41]. The arrangement is shown in Figure 2-19.

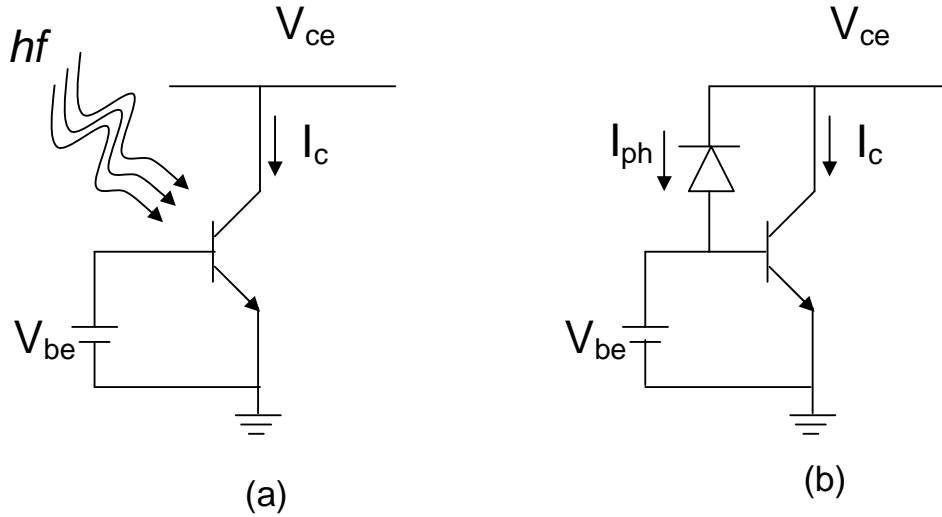


Figure 2-19. 3T HPT Configuration

The additional hole current ($I_{b,ext}$) in 3T-HPT configuration is obtained from the external bias (V_{be}). The collector current of a HBT under dark conditions can be given as:

$$I_c = \beta I_{b,ext} \quad (2.46)$$

However, when the HPT is illuminated the photo-generated current contributes directly to the gain and the collector current under illumination ($I_{c,ill}$) is given as:

$$I_{c,ill} = \beta_{ill}(I_{b,ext} + I_{ph}) + I_{ph} \quad (2.47)$$

where β_{ill} is the current gain under illumination. The photoresponse (ΔI_c) of the 3T-HPT may be expressed as the difference of the collector current under-illumination and under dark conditions [40] and can be written as:

$$\Delta I_c = I_{c,ill} - I_c \quad (2.48)$$

Substituting (2.46) and (2.47) in (2.48) gives (2.49):

$$\Delta I_c = I_{ph}(\beta_{ill} + 1) + I_{b,ext}(\Delta\beta) \quad (2.49)$$

where $\Delta\beta = \beta_{ill} - \beta$. Thus the optical gain is the ratio of photoresponse to the primary photocurrent in the base. The final expression for the optical gain can be given as [40]:

$$G_{3T-HPT} = (\beta_{ill} + 1) + \Delta\beta \left(\frac{I_{b,ext}}{I_{ph}} \right) \quad (2.50)$$

2.3 Spectral Response Model for Detection

2.3.1 Basic Absorption Mechanism

This section explains the process of optical detection in a semiconductor and the different parameters affecting it. The first consideration is to determine the optical power absorbed at any point in a semiconductor layer when incident radiation falls on it. On reaching the surface of the semiconductor, light of incident power (P_o) will be reduced to $P_o(1 - R_f)$, where R_f is the Fresnel reflection coefficient. On passing through the semiconductor, the light will be absorbed and the attenuation will lead to an exponential decay of the propagating radiation power density with distance. This is shown in Figure 2-20.

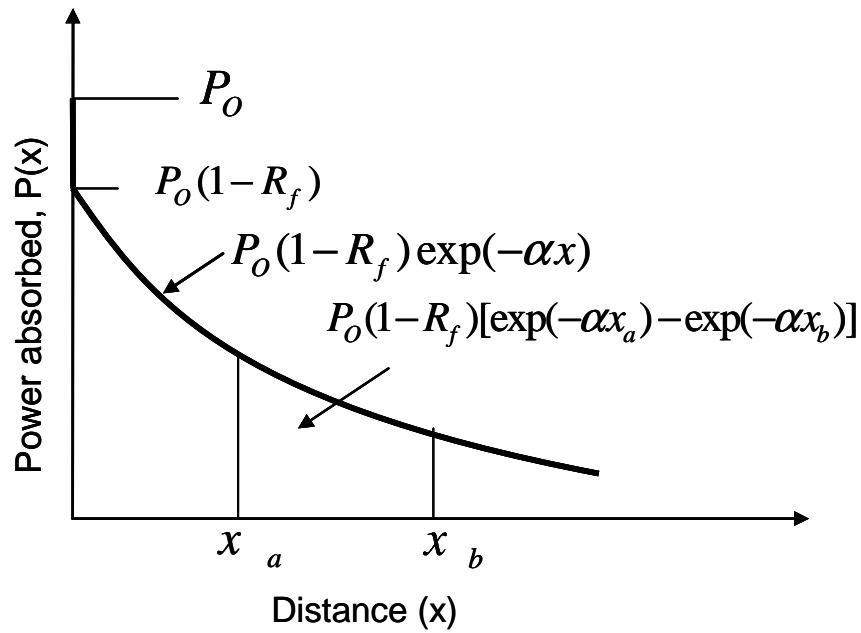


Figure 2-20. Schematic Illustration of the attenuation of the optical power density with the depth below the incident surface.

Here, α is the attenuation coefficient and is dependent on the characteristics of the material. This is a strong function of threshold wavelength of the material. The intensity of the power at different locations in the material can also be ascertained from Figure 2-20. If the power absorbed between two points is to be calculated, say x_a and x_b , the difference of power between the two points is the power absorbed within that region, i.e. $P(x_a) - P(x_b)$. The principle explained above can be used for semiconductor photodetectors.

A photodetector is capable of detecting only radiation with photon energy $h\nu$ greater than the band gap, E_g of the device material. However, if $h\nu$ is much greater than E_g , then the absorption will take place entirely near the surface and as the photon energy increases, the penetration depth decreases. The electron-hole pairs created by absorption of the high energy photons near the surface of the detecting device (i.e., away from the junction or the adjacent diffusion fields) is not useful. A large proportion of these photogenerated carriers will recombine with majority carriers before diffusing into the depletion layer. This event does not contribute to the current flow and is undetectable [42]. Figure 2-21 shows a layer of semiconductor, layer 2, bounded at 'A' by layer 1 and at 'B' by layer 3.

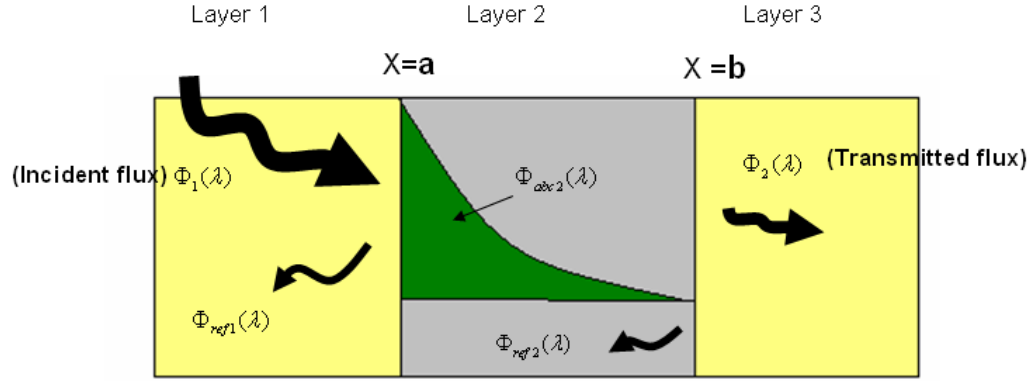


Figure 2-21. Schematic of optical flux propagation, absorption and reflection for a multilayered semiconductor device.

It is assumed that layer 1 is completely transparent to the incoming flux and each of these layers is assumed to have homogenous material properties and constant doping concentration. Thus the flux absorbed as a function of the wavelength for layer 2 ($\phi_{abs2}(\lambda)$) can be expressed as [43],

$$\Phi_{abc2}(\lambda) = [\Phi_1(\lambda) - \Phi_{ref1}(\lambda)] \cdot \left\{ \exp^{-[a\alpha_2(\lambda)]} - \exp^{-[b\alpha_2(\lambda)]} \right\} \quad (2.51)$$

The parameters involved are;

ϕ_1 = The incident flux from layer 1 at the layer1/layer 2 interface

ϕ_2 = The absorption coefficient of layer 2

a = The distance of the first boundary of layer 2 from the air

b = The distance of the second boundary of layer 2 from the air

ϕ_{ref1} = the reflected flux from layer 1 at the layer1/layer 2 interface given as,

$$\Phi_{ref1}(\lambda) = \left[\frac{n_2(\lambda) - n_1(\lambda)}{n_2(\lambda) + n_1(\lambda)} \right]^2 \quad (2.52)$$

where,

n_1 = refractive index of layer 1 at a given λ .

n_2 = refractive index of layer 2 at a given λ .

2.3.2 Monolayer Detection for InP and GaAs

The simulation results from the detection model for InP and GaAs are given and discussed in this section. However, only the monolayers are considered for simplicity at this point and multilayer absorption using HPTs is discussed in section 4.1. The optical data used for GaAs and InP layers is obtained from the literature [44, 45]. Referring to (2.51), the fraction of flux absorbed versus wavelength for InP and GaAs is given in Figure 2-22. It is clear that the maximum absorption occurs at a wavelength close to the corresponding band gap of the materials.

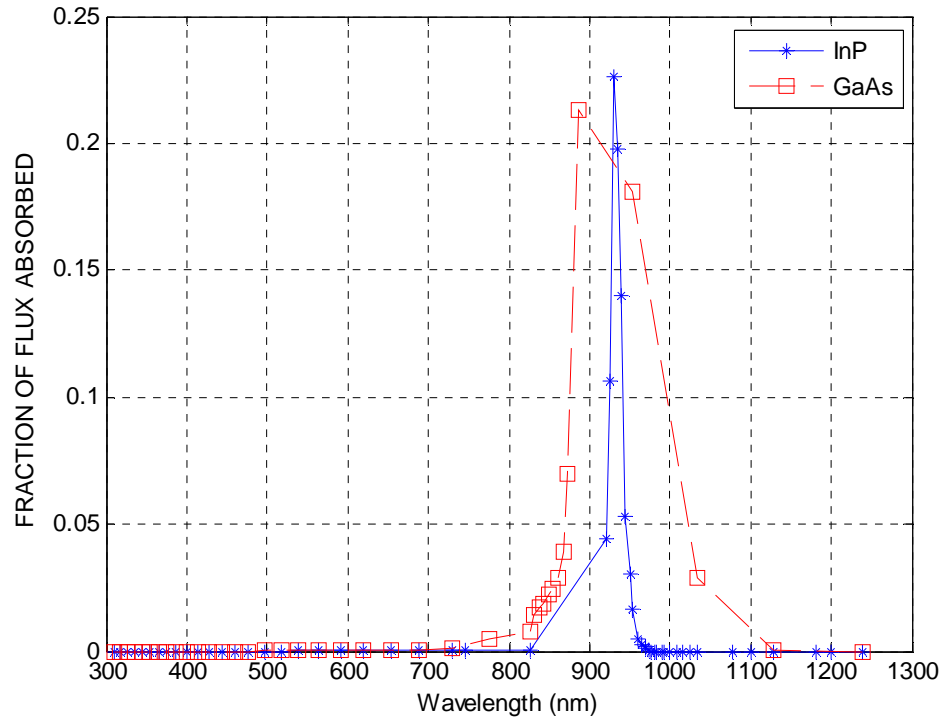


Figure 2-22. Simulated results (MATLAB) for the fraction of flux absorbed as a function of wavelength for 10 μm mono-layers of InP and GaAs.

Absorption for InP is maximum in the wavelength of region 920-950 nm. The absorption at any other wavelength is relatively minimal. This is due to the reason that the wavelength corresponding to the band-gap of InP is 925 nm ($E_g = 1.34$ eV). Thus, the maximum absorption should take place close to this critical wavelength. Associated parameters such as refractive index and the absorption coefficient are strongly dependent on the band gap of the material. InP will be transparent for wavelengths beyond 950 nm and therefore devices with InP-emitters (e.g InP/ $\text{In}_{0.53}\text{Ga}_{0.47}\text{As}$ HPTs) are suitable for long wavelength detection.

Similarly, most of the absorption for GaAs occurs close to the 873 nm wavelength which corresponds to the band gap of GaAs. Thus GaAs devices cannot be used for detecting wavelengths beyond 870 nm and are therefore restricted to short wavelength detection at 850 nm.

References

- [1] J. H. J. Wilson, *Optoelectronics: An Introduction*, 3rd ed: Prentice Hall, 1998.
- [2] R. S. Muller and T. I. Kamins, *Device Electronics for Integrated Circuits*, 2nd ed: New York Wiley, 1986.
- [3] J. Sexton, "Fabrication and Characterisation of High-Speed Indium Phosphide Based Heterojunction Bipolar Transistors," Ph.D thesis, The University of Manchester, 2005.
- [4] T. Tauqeer, "Low Power, High Speed InP-Based Digital Integrated Circuits for Ultra Wide Band Communication Systems," PhD Thesis, The University of Manchester, 2009.
- [5] S. M. Sze, *Semiconductor Devices: Physics and Technology*: John Wiley & Sons, 1985.
- [6] S. M. Sze, *Physics of Semiconductor Devices*, 2nd ed. USA: John Wiley & Sons, 2001.
- [7] M. S. Tyagi, *Introduction to Semiconductor Materials and Devices*: John Wiley & Sons, 1991.
- [8] D. E. Aspnes, "Recombination at semiconductor surfaces and interfaces," presented at Proceedings of the Second Trieste ICTP-IUPAP Semiconductor Symposium on Surfaces and Interfaces, Physics and Electronics, 30 Aug.-3 Sept. 1982, Netherlands.
- [9] A. A. Rezazadeh, M. Sotoodeh, and N. Dharmasiri, "Base-collector design optimisation of InGaP/GaAs DHBTs," presented at 8th IEEE International Symposium on High Performance Electron Devices for Microwave and Optoelectronic Applications (EDMO 2000), November 13, 2000 - November 14, 2000, Glasgow, United kingdom, 2000.
- [10] V. Hernandez-Solis, "Electrical and Optical Characterisation of Hetrojunction Bipolar Transistors," MSc Dissertaion, UMIST, 2003.
- [11] S. C. Subramaniam, "Ion-Implant Isolation of InP/InGaAs HBTs," Ph.D thesis, The University of Manchester, 2005.
- [12] S. A. Bashar, "Study of Indium Tin Oxide (ITO) for Novel Optoelectronic Devices," Ph.D thesis, King's College London, 1998.

- [13] R. M. Warner and B. L. Grung, *Transistors. Fundamentals for the Integrated Circuit Engineer*: John Wiley & Sons, USA, 1983.
- [14] C. T. Kirk, Jr., "A theory of transistor cutoff frequency (f_t) falloff at high current densities," *Electron Devices, IRE Transactions on*, vol. 9, pp. 164-174.
- [15] H. Kroemer, "Heterostructure bipolar transistors and integrated circuits," *Proceedings of the IEEE*, vol. 70, pp. 13-25, 1982.
- [16] B. Zeghbroeck, *Principles of Semiconductor Devices*: Colorado Press, University of Colorado, 2004.
- [17] D. E. Kren, "High Carbon-Doped Base HBTs Growth and Processing Engineering," Ph.D thesis, King's College London, 1995.
- [18] M. E. Klausmeier-Brown, M. S. Lundstrom, and M. R. Melloch, "Effects of heavy impurity doping on AlGaAs/GaAs bipolar transistors," *IEEE Transactions on Electron Devices*, vol. 36, pp. 2146-2155, 1989.
- [19] K. L. Lew, S. F. Yoon, H. Wang, S. Wicaksono, J. A. Gupta, and S. P. McAlister, "High-gain low turn-on voltage AlGaAs/GaAsNSb/GaAs heterojunction bipolar transistors grown by molecular beam epitaxy," *IEEE Electron Device Letters*, vol. 28, pp. 1083-1085, 2007.
- [20] S. Zhou, H. Cui, Y. Huang, and X. Ren, "Numerical study on currents for band gap narrowing in abrupt AlGaAs/GaAs HBT," *Guti Dianzixue Yanjiu Yu Jinzhan/Research and Progress of Solid State Electronics*, vol. 25, pp. 152-156, 2005.
- [21] C. D. Parikh and F. A. Lindholm, "Space-charge region recombination in heterojunction bipolar transistors," *IEEE Transactions on Electron Devices*, vol. 39, pp. 2197-2205, 1992.
- [22] A. Rezazadeh, "Design and Technology of III-V HBTs for wireless communications," presented at Wireless Broadband Forum, Cambridge, UK, 2002.
- [23] H. Sheng and A. A. Rezazadeh, "Prospects of InP/InGaAs HBTs for low power and high speed analogue applications," presented at IEE Electronics Division on Low Power Analogue and Digital VLSI: Asics, Techniques and Applications, June 2, 1995 - June 2, 1995, London, UK, 1995.
- [24] K. Ishii, H. Nosaka, M. Ida, K. Kurishima, M. Hirata, T. Enoki, and T. Shibata, "High-bit-rate low-power decision circuit using InP/InGaAs HBT

technology," presented at ESSCIRC 2004 - Proceedings of the 30th European Solid-State Circuits Conference, September 21, 2004 - September 23, 2004, Leuven, Belgium, 2004.

- [25] J.-I. Shirakashi and M. Konagai, "InGaP/GaAs and InP/InGaAs heterojunction bipolar transistors with a super heavily carbon-doped base grown by metalorganic molecular beam epitaxy," *Proceedings of the Topical Workshop on Heterostructure Microelectronics, August 17 - 19, 1994*.
- [26] E. Sano, K. Sano, T. Otsuji, K. Kurishima, and S. Yamahata, "Ultra-high speed, low power monolithic photoreceiver using InP/InGaAs double-heterojunction bipolar transistors," *Electronics Letters*, vol. 33, pp. 1047-1048, 1997.
- [27] E. Sano, K. Kurishima, H. Nakajima, and S. Yamahata, "High-speed, low-power lightwave communication ICs using InP/InGaAs double-heterojunction bipolar transistors," *IEICE Transactions on Electronics*, vol. E83-C, pp. 2000-2006, 2000.
- [28] H. Fukano, M. Tomizawa, Y. Takanashi, and M. Fujimoto, "InAlAs/InGaAs heterojunction bipolar transistors with an n-doped InGaAs spacer," *Japanese Journal of Applied Physics, Part 1: Regular Papers and Short Notes and Review Papers*, vol. 31, pp. 3816-3822, 1992.
- [29] D. Cui, D. Sawdai, D. Pavlidis, Shawn, S. H. Hsu, P. Chin, and T. Block, "High power performance using InAlAs/InGaAs single heterojunction bipolar transistors," *2000 International Conference on Indium Phosphide and Related Materials, May 14, 2000 - May 18, 2000*, pp. 473-476, 2000.
- [30] M. Hafizi, R. A. Metzger, W. E. Stanchina, D. B. Rensch, J. F. Jensen, and W. W. Hooper, "The effects of base dopant diffusion on DC and RF characteristics of InGaAs/InAlAs heterojunction bipolar transistors," *Electron device letters*, vol. 13, pp. 140-142, 1992.
- [31] Z. Lixin and S. Guangdi, "The microwave performance of SiGe/Si HBTs and amplifiers," presented at Proceedings of International Conference on Microwave and Millimeter Wave Technology, 18-20 Aug. 1998, Beijing, China, 1998.
- [32] N. Jiang and Z. Ma, "Current gain of SiGe HBTs under high base doping concentrations," *Semiconductor Science and Technology*, vol. 22, pp. 168-72, 2007.

- [33] T. Miya, Y. Terunuma, T. Hosaka, and T. Miyashita, "Ultra low loss single-mode fibers at 1.55 μ m," *Review of the Electrical Communication Laboratories*, vol. 27, pp. 497-516, 1979.
- [34] O. Esame, Y. Gurbuz, I. Tekin, and A. Bozkurt, "Performance comparison of state-of-the-art heterojunction bipolar devices (HBT) based on AlGaAs/GaAs, Si/SiGe and InGaAs/InP," *Microelectronics Journal*, vol. 35, pp. 901-908, 2004.
- [35] K. D. L. Dessau, "Insights into High-Speed Detectors and High-Frequency Techniques," in *Application notes (Edward L. Ginzton Laboratory)*. Stanford University, 2004.
- [36] D. G. Parker and P. G. Say, "Indium tin oxide/GaAs photodiodes for millimetric-wave applications," *Electronics Letters*, vol. 22, pp. 1266-7, 1986.
- [37] D. Renker and E. Lorenz, "Advances in solid state photon detectors," *Journal of Instrumentation*, vol. 4, pp. P04004 (55 pp.), 2009.
- [38] S. Chandrasekhar, M. K. Hoppe, A. G. Dentai, C. H. Joyner, and G. J. Qua, "Demonstration of enhanced performance of an InP/InGaAs heterojunction phototransistor with a base terminal," *IEEE Electron Device Letters*, vol. 12, pp. 550-2, 1991.
- [39] R. A. Milano, P. D. Dapkus, G. E. Stillman, and G. E. Stillman, "An analysis of the performance of heterojunction phototransistors for fiber optic communications," *IEEE Transactions on Electron Devices*, vol. ED-29, pp. 266-74, 1982.
- [40] L. E. M. Barris, "Bias dependent gain and speed mechanism in illuminated HBTs," presented at 26th EuMC, Prague, pp 1019-1023, 1996.
- [41] S. M. Frimel and K. P. Roenker, "A thermionic-field-diffusion model for Npn bipolar heterojunction phototransistors," *Journal of Applied Physics*, vol. 82, pp. 1427-37, 1997.
- [42] S. A. Bashar and A. A. Rezazadeh, "Characterisation of transparent ITO emitter contact InP/InGaAs heterojunction phototransistors," presented at Proceedings of the 3rd IEEE International Workshop on High Performance Electron Devices for Microwave and Optoelectronic Applications, EDMO 95, 27 Nov. 1995, London, UK, 1995.

- [43] S. A. Bashar and A. A. Rezazadeh, "Fabrication and spectral response analysis of AlGaAs/GaAs and InP/InGaAs HPTs with transparent ITO emitter contacts," *IEE Proceedings-Optoelectronics*, vol. 143, pp. 89-93, 1996.
- [44] A. R. Forouhi and I. Bloomer, ""Optical Functions of Intrinsic InP : General Remarks" , Properties of Indium Phosphide," *INSPEC, EMIS Data Review Series No. 6, 1991, pp. 105 - 137*, 1991.
- [45] D. E. Aspnes, S. M. Kelso, R. A. Logan, and R. Bhat, "Optical properties of Al_xGa_{1-x}As," *Journal of Applied Physics*, vol. 60, pp. 754-67, 1986.

Chapter 3

Device Structures and Experimental Setup

3.1 Device Structures

The device layer structures and the micrographs for the $\text{Al}_{0.3}\text{Ga}_{0.7}\text{As}/\text{GaAs}$ sHPT, $\text{InP}/\text{In}_{0.47}\text{Ga}_{0.53}\text{As}$ sHPT and $\text{In}_{0.49}\text{Ga}_{0.51}\text{P}/\text{GaAs}$ DHBT are presented in this chapter.

3.1.1 AlGaAs/GaAs sHPT

The $\text{Al}_{0.3}\text{Ga}_{0.7}\text{As}/\text{GaAs}$ HBT on K15 is an Npn transistor with a graded B-E junction. The layer structure is shown in Table 3.1 followed by the schematic device structure in Figure 3-1. Layer 1 of the structure is a thick (roughly $400\mu\text{m}$) GaAs substrate which is undoped to keep it semi-insulating. Alternatively, this could also be doped with Cr to settle any free carriers in it [1]. The sub-collector is highly doped to make low resistance n-type ohmic contacts. The collector is lightly doped to keep the breakdown voltage as low as possible during reverse-bias condition. This is followed by a heavily doped GaAs base to provide low base resistance and efficient p-type ohmic contacts [2]. The B-E junction is graded, hence a couple of thin AlGaAs layers on either side of the emitter are present for gradual grading of the junction and to minimize the conduction band discontinuity. The emitter itself is a wide-band gap $\text{Al}_{0.3}\text{Ga}_{0.7}\text{As}$ which is followed by GaAs on the top to facilitate the n-type ohmic contact.

Good ohmic contacts are required for good device performance. In theory, ‘ohmic’ refers to a linear I-V characteristic in both directions. However, in practice, the contact is usually acceptable if it can supply the required current density with a voltage drop that is very small compared to the drop across the active region of the device even though its behaviour may not be strictly linear. Other desirable properties of ohmic contacts include good adhesion to the semiconductor, smooth surface morphology, ability to bond gold wires to connect the device to external

circuitry and contact reliability. Therefore, a practical ohmic contact system often consists of a ‘wetting agent’ to promote adhesion, followed by the dopant species and finally a thick layer of Au for bonding purposes [3]. The ohmic contacts for AlGaAs/GaAs sHBT are shown in Figure 3-2.

Table 3.1: Layer structure for graded emitter/base junction AlGaAs/GaAs sHBT.

Layer	Material	Mole fraction (%)	Thickness (μm)	Doping (cm^{-3})	Type	Dopant	Comments
8	GaAs	-	0.19	5×10^{18}	n	Si	Cap layer
7	$\text{Al}_x\text{Ga}_{1-x}\text{As}$	30 - 0	0.02	5×10^{17}	n	Si	Grading layer
6	$\text{Al}_x\text{Ga}_{1-x}\text{As}$	30	0.15	5×10^{17}	n	Si	Emitter
5	$\text{Al}_x\text{Ga}_{1-x}\text{As}$	0 - 30	0.02	5×10^{17}	n	Si	Grading layer
4	GaAs	-	0.09	2×10^{19}	p	C	Base
3	GaAs	-	0.5	2×10^{16}	n	Si	Collector
2	GaAs	-	1.0	5×10^{18}	n	Si	Sub-collector
1	GaAs	-	400	U/D	S-I		Substrate

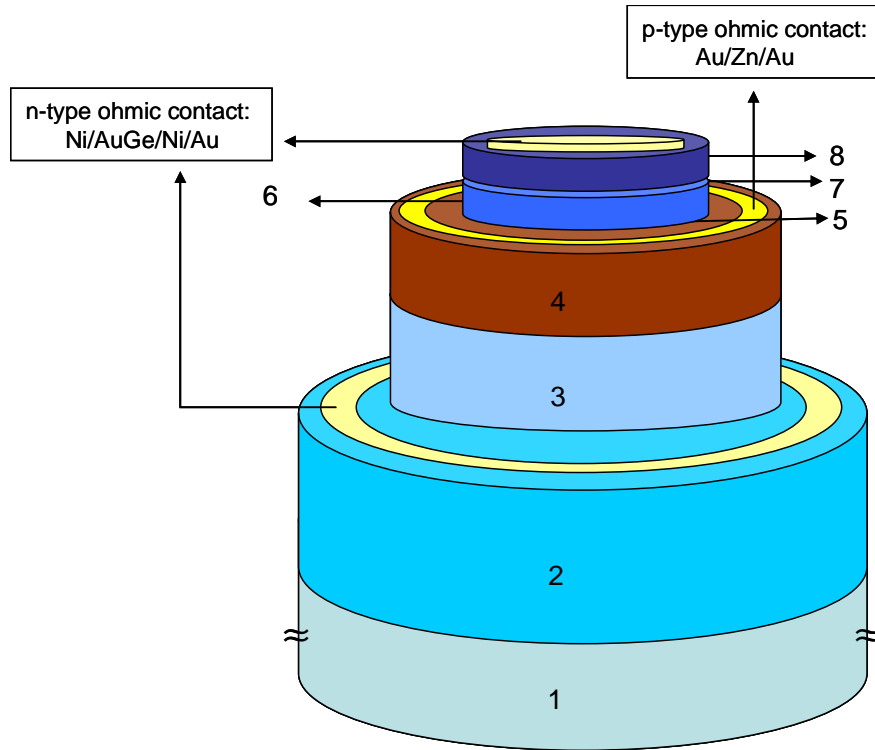


Figure 3-1. Schematic device structure of AlGaAs/GaAs sHBT with numbers (1-8) being referred to Table 3.1.

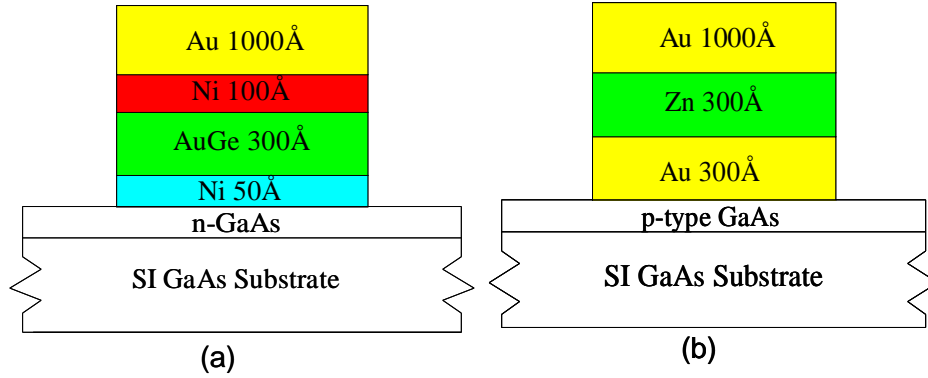


Figure 3-2. Typical metallization structure for (a) Ni/AuGe/Ni/Au on n-type GaAs, (b) Au/Zn/Au on p-type GaAs with a SI GaAs substrate

Ni/AuGe/Ni/Au is the most commonly used n-type contact to the GaAs system. However, this system has several frailties such as balling up during annealing as a result of liquid phase reactions, non-uniform contact resistivity and spiking [3]. An alternative which addresses many of these issues is the Pd/Ge/Au system [4, 5].

The usual p-type contact for GaAs is the Au/Zn/Au system where Zn atoms act as acceptors. In devices such as HBTs the base is very thin and junction shorting due to Au spiking is often more of a concern than the resistivity, especially for high temperature or high current applications. In this case, Pt/Ti/Au can also be used as an alternative [6]. The micrograph of the fabricated $\text{Al}_{0.3}\text{Ga}_{0.7}\text{As}/\text{GaAs}$ HPT is shown in Figure 3-3. The base-emitter and the base- collector junction areas are calculated to be $2.3 \times 10^4 \mu\text{m}^2$ and $1.4 \times 10^5 \mu\text{m}^2$ respectively.

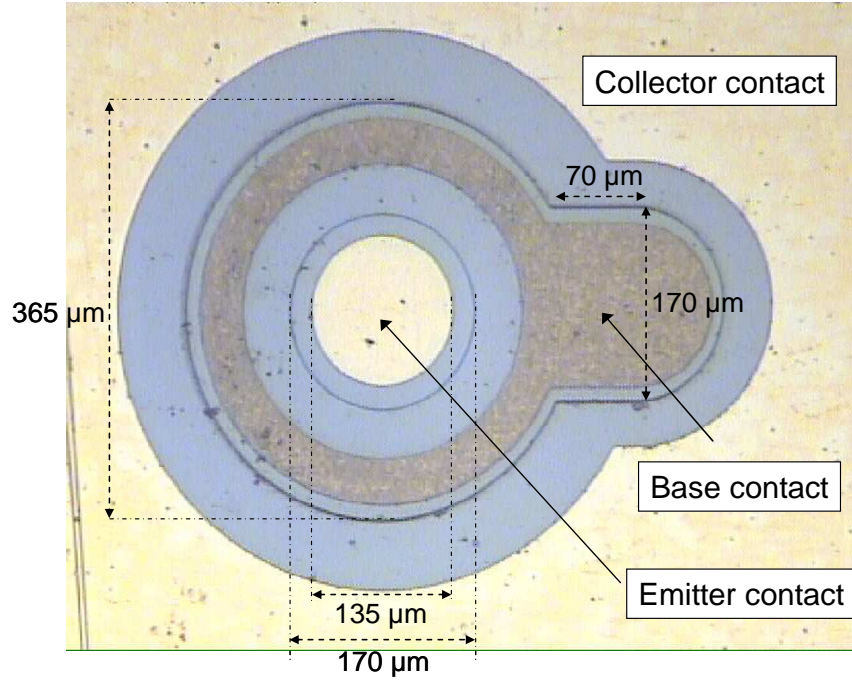


Figure 3-3. Micrograph of a fabricated Npn $Al_{0.3}Ga_{0.7}As/GaAs$ HPT on K15 (emitter contact diameter = $135 \mu m$).

3.1.2 $InP/InGaAs$ sHPT

The InP-based structure was grown by the MOCVD technique on a Fe-doped SI substrate. The base was Zn-doped and the detailed layer structure is given in Table 3-2. The B-E and B-C junction areas are $2.3 \times 10^4 \mu m^2$ and $1.4 \times 10^5 \mu m^2$ respectively.

Table 3.2: Layer structure for lattice-matched $InP/In_{0.47}Ga_{0.53}As$ HPT.

Layer	Material	Dopant	Thickness(μm)	Doping (cm^{-3})
Cap	n^+ - InGaAs	Si	0.1	2×10^{19}
Emitter Cap	n^+ -InP	Si	0.05	2×10^{19}
Emitter	n- InP	Si	0.1	3×10^{17}
Spacer	Ud-InGaAs	ud	0.01	ud
Base	p^+ -InGaAs	Zn	0.1	2×10^{19}
Collector	n-InGaAs	Si	0.4	5×10^{16}
Sub-Collector	n^+ -InGaAs	Si	0.4	2×10^{19}
Buffer	ud-InP	Ud	0.5	ud
Substrate	SI-InP	Fe		

The metal system for ohmic contacts for the n^+ - InGaAs layer is based on Ti/Au composite. A thickness of 500 Å and 1000 Å was used for Ti and Au metals, respectively. The advantage of using Ti/Au is that no alloying is required and they can be used to contact both highly doped n- and p- type InGaAs structures, reducing the number of processing steps required [7]. Ti/Au has also been applied to the n-type InP layer. It has been shown through bias stress measurements, that Ti/Au contacts are more reliable and do not degrade with time at elevated temperatures when compared with conventional Au/Zn/Au contacts for p-type metal contacts in HPT devices [8]. The micrograph of the fabricated device is shown in Figure 3-4.

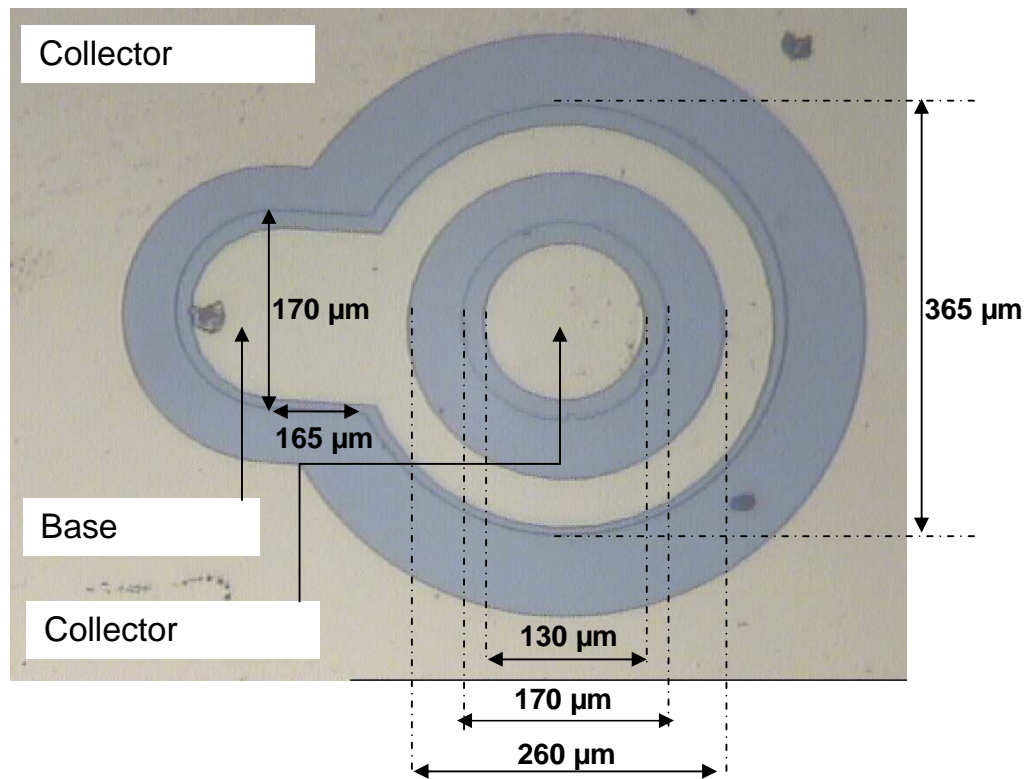


Figure 3-4. Micrograph of a fabricated Npn $InP/In_{0.47}Ga_{0.53}As$ HPT on MR2021 (emitter contact diameter = 130 μm).

3.1.2 InGaP/GaAs DHBT

The microwave device under review is a double InGaP/GaAs HBT with an E-B area $16 \times 20 \mu m^2$ and B-C area of $16 \times 26 \mu m^2$. The design provides high breakdown

and low turn-on voltage. The epitaxial layer structure and the detailed doping profile of the device is shown in Figure 3-4 and Table 3.2 respectively [9].

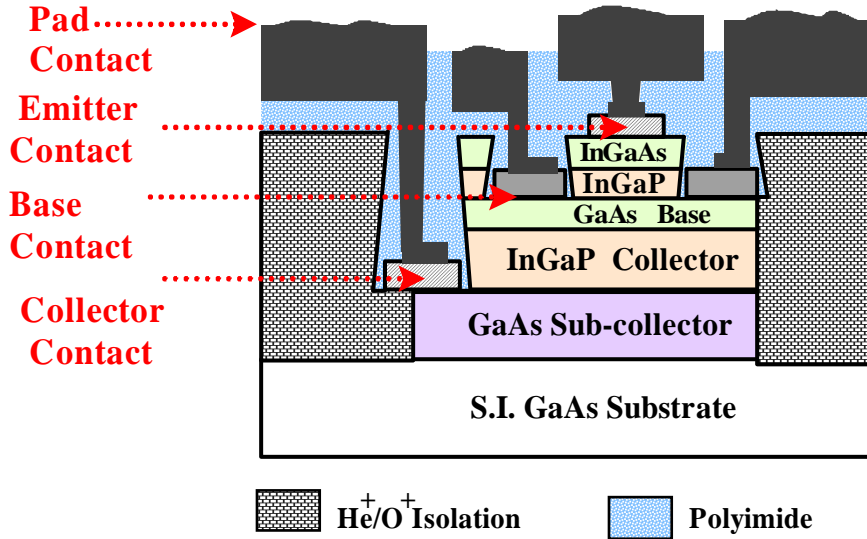


Figure 3-5. Epitaxial structure of the InGaP/GaAs DHBT.

Material	Thickness (Å)	Doping (cm ⁻³)	Dopant	Comments
n ⁺ -InGaAs	300	1x10 ¹⁸	Si	Cap layer
n ⁺ -GaAs-InGaAs	300	1x10 ¹⁸	Si	
n ⁺ -GaAs	1000	8x10 ¹⁸	Si	
N ⁺ -In _{0.49} Ga _{0.51} P	300	6x10 ¹⁸	Si	
n-In _{0.49} Ga _{0.51} P	1000	5x10 ¹⁷	Si	Emitter
p ⁺ -GaAs	800	2x10 ¹⁹	C	Base
n ⁻ -GaAs	300	1x10 ¹⁶	Si	Spacer
n ⁺ -InGaP	50	2x10 ¹⁸	Si	Doping spike
n ⁻ -In _{0.49} Ga _{0.51} P	4650	3x10 ¹⁶	Si	Collector
n ⁺ -GaAs	7000	5x10 ¹⁸	Si	Sub-Collector
S.I. GaAs	635μm	u/d	-	Substrate

Table 3.2: Doping profile of the InGaP/GaAs DHBT.

In the doping profile, the substrate is semi-insulating GaAs. This acts as a dielectric and stops carriers from going down and being confined to the collector. In addition to base, emitter and collector layers, highly doped layers are deposited either side of the

collector and emitter to facilitate an ohmic contact, these being placed on the contact layers after exposure by photolithography. The collector is lightly doped to reduce B-C capacitance and increase the cut-off frequency of the device. The spacer layer helps to lower the conduction band spike and lower the width of this barrier, thus improving the tunnelling transmission across it [10]. The micrograph of the device is shown in Figure 3-6 and the detailed view of the active region of the device is given in Figure 3-7.

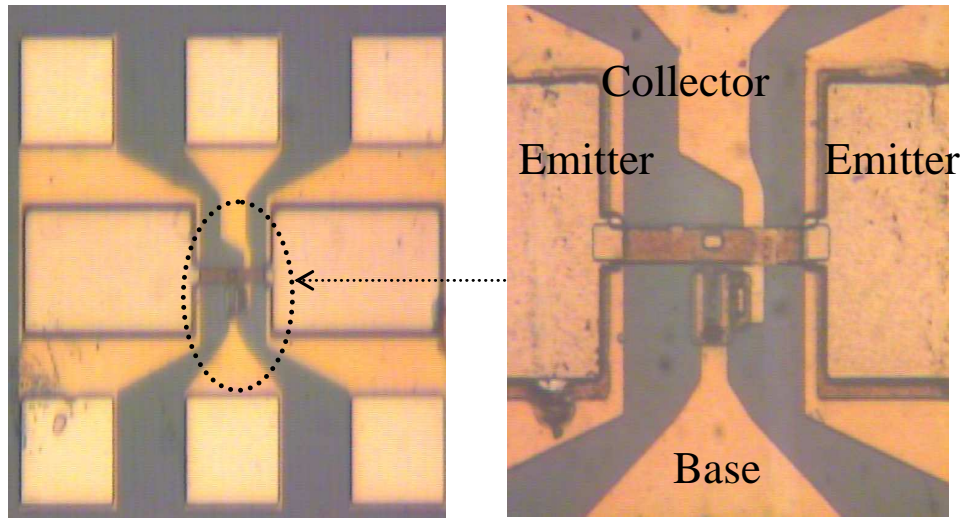


Figure 3-6. Micrograph of the InGaP/GaAs DHBT under review.

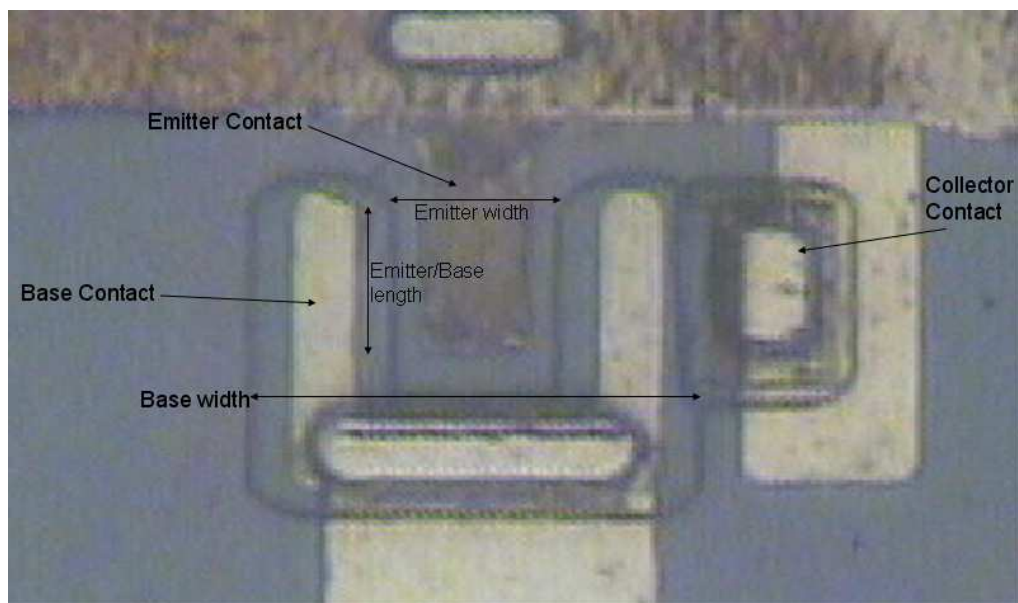


Figure 3-7. Active region of the device with marked lengths, Emitter width = 20 μm , Emitter/base length = 16 μm and Base width = 26 μm .

3.2 Laser Operation and Characterisation

LASER is the acronym for ‘light amplification by stimulated emission of radiation’. Semiconductor lasers are devices of great importance to optical communication systems due to their small size, high efficiency and high speed of direct modulation. The operating principle for laser is not very different from that for a light emitting diode (LED). For the laser to work, in addition to the injection provided by the forward biased p-n junction, there are requirements of stimulated emission and optical feedback [11]. A necessary condition for lasing is the separation of quasi-Fermi levels (corresponding to the non-equilibrium concentrations of electrons and holes) must exceed the energy of the emitted radiation, i.e. stimulated emission in excess of absorption occurs when a photon is likely to cause a downward transition of an electron from the conduction band with the emission of a photon of the same energy and phase, than the upward transition from the valence to conduction band with the absorption of a photon [12]. This downward transition from the conduction to valence band with absorption of the photon is known as negative absorption.

When forward bias is applied to the p-n junction, a current will flow through it and non-radiative and radiative recombination processes take place according to the energy-band structure of the semiconductors. If the forward bias is high enough such that the injected carrier density creates a population inversion over a diffusion length, then over this region, the carriers will recombine radiatively producing spontaneous emitted photons. In addition, the cleaved walls at the two ends of the semiconductor structure act as a mirror, resulting in optical feedback. The spontaneous emitted photons can stimulate upward and downward transitions resulting in new stimulated emitted photons. Solid-state lasers are made of materials of which the stimulated emission is possible; furthermore, if the rate of such stimulated emission is sufficiently high, the medium exhibits gain and at that point lasing starts. The current at which the gain exceeds losses within the active region, or spontaneous incoherent emission is replaced by stimulated emission of radiation, is known as the threshold current [13, 14] .

3.3 Experimental Setup

Laser diodes were inserted into a case with proper BNC electrical contacts for the input electrical signal. The temperature of the laser diodes was kept constant at room temperature by not using it for extended periods of time. This was done for the reason that the semiconductor band gap varies with the change in temperature. This can affect the conducting wavelength of a laser, which will result in variation of absorption within the semiconductor. The input pulse signal is driven from a HP 8082A pulse generator. The amount of input current to drive the laser diode is varied by changing the DC offset voltage taken from pulse generator and accurately monitored by using an oscilloscope.

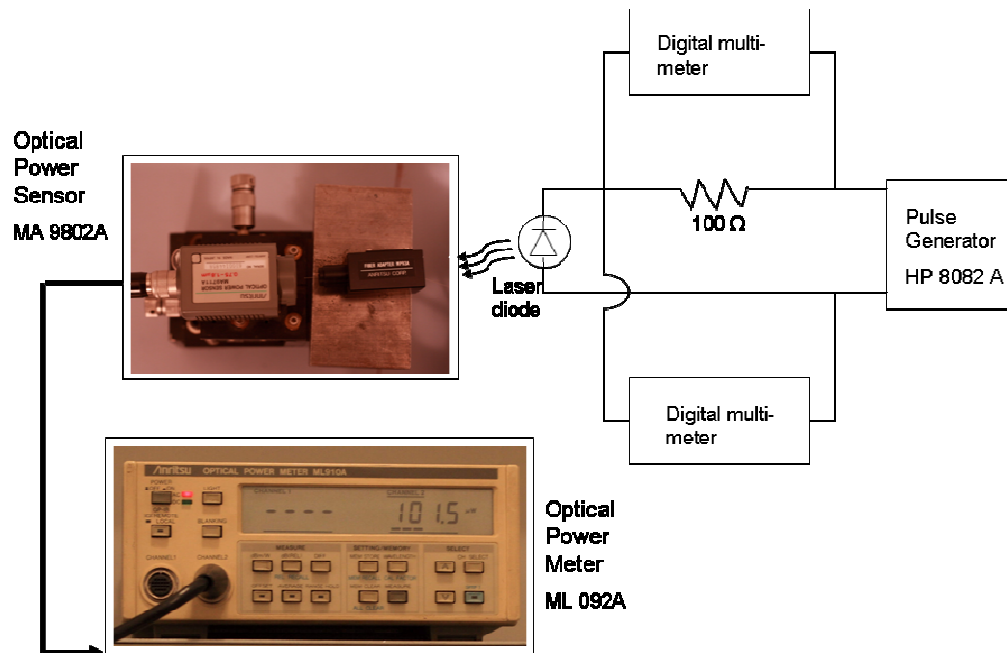


Figure 3-8. Block diagram of the setup to characterise laser diodes.

In order to monitor the amount of current (through) and voltage (across) the laser diode (LD), two digital millimetres were used as depicted in Figure 3-8. The amount of power emitted by the LD (at the end of the optical fibre) is recorded for a specific voltage drop across the LD, which was then referred to carefully estimate the power falling on the base region of the phototransistor. For instance, a 635 nm Sanyo DL-3148-033 AlGaAs/GaAs laser diode with maximum power output of 5 mW is used to

characterise the phototransistors for 635 nm. Due to the orientation of the experiment set-up, the power falling on HBT cannot be measured for every single different value. In order to measure how much power is expected for laser emission, an output chart was maintained which is shown in Figure 3-9. It can be observed that the laser diode starts lasing approximately at 1.5V and the threshold current is 25.6 mA.

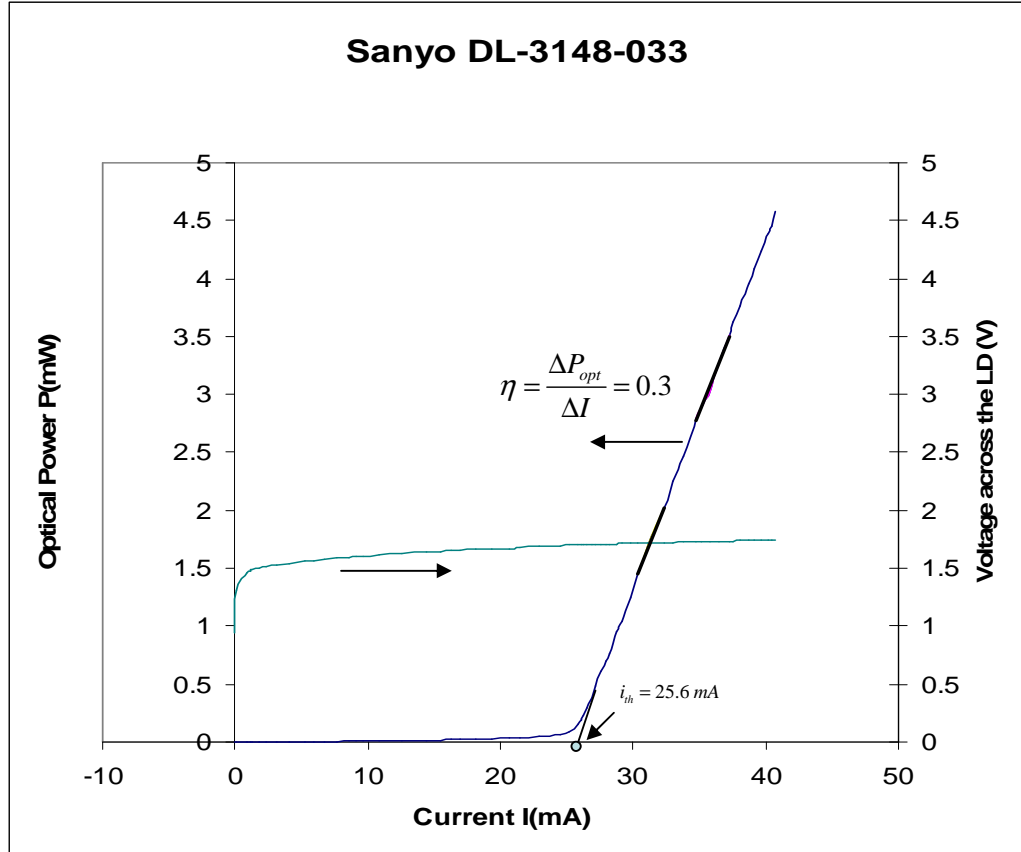


Figure 3-9. Measured output characteristics for Sanyo DL-3148-033 laser diode.

The HPT wafers under investigation were set on a four DC-probe station. Three probes were specifically connected to the HPT terminal points and the fourth one was connected to optical fibre to illuminate the device base terminal with incident optical radiation. The LD is aligned to a multimode optical fibre (50μm core diameter) using collimating and focusing lenses. The optical radiation at the end of optical fibre is measured with an Anritsu optical power sensor MA 9802A, which is connected to an Anritsu optical power meter ML 092A.

The input signal to the laser is driven by a HP 8082A pulse generator and the input current is modified by changing the DC offset voltage of the signal from the pulse generator. The block diagram of the experimental set up is shown in Figure 3-9. L1 is a collimating lens and is used to obtain a parallel beam which is focused on the optical fibre through focusing lens L2. The end of the optical fibre is placed at the focal length of L2 ($f_{o, L2}$) for optimal alignment.

The semiconductor parameter analyzer (SPA) is capable of accurately measuring and graphically displaying DC characteristics of semiconductor devices. By appropriate programming of the SPA, the measured data are recorded in spreadsheet format and a network connection in the SPA allows the saving of data in any network location. For instance, voltage sweeping in the collector probe at fixed steps of current in the base probe with the emitter probe grounded, gives the current-voltage (I-V) characteristics of a transistor under investigation.

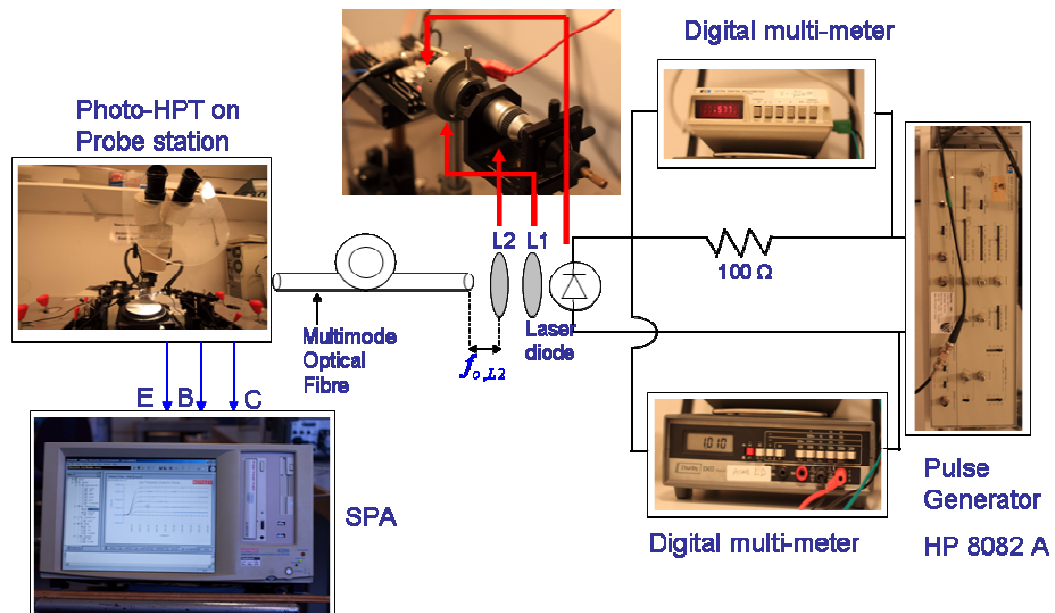


Figure 3-10. Block diagram of experimental setup to obtain the DC electrical characteristics and the SR of HPTs.

References

- [1] D. Kren, "High Carbon-Doped Base HBTs-Growth and Processing Engineering," Ph.D thesis, King's College London, 1995.
- [2] C. R. Abernathy, S. J. Pearton, F. Ren, W. S. Hobson, T. R. Fullowan, A. Katz, A. S. Jordan, and J. Kovalchick, "Carbon doping of III-V compounds grown by MOMBE," *Proceedings of the Second International Conference on Chemical Beam Epitaxy and Related Growth Techniques - (ICCBE-2), December 11, 1989 - December 13, 1989*
- [3] S. A. Bashar, "Study of Indium Tin Oxide (ITO) for Novel Optoelectronic Devices," Ph.D thesis, King's College London, 1998.
- [4] J. T. Lai and J. Y. Lee, "Redistribution of constituent elements in Pd/Ge contacts to n-type GaAs using rapid thermal annealing," *Journal of Applied Physics*, vol. 76, pp. 1686-1690, 1994.
- [5] T. Sanada and O. Wada, "Ohmic Contacts to p-GaAs with Au/Zn/Au Structure," *Japanese Journal of Applied Physics*, vol. 49, pp. 491-494, 1980.
- [6] A. Katz, S. N. G. Chu, B. E. Weir, C. R. Abernathy, W. S. Hobson, S. J. Pearton, and W. Savin, "Rapid isothermal processing of Pt/Ti contacts to p-type III-V binary and related ternary materials," *IEEE Transactions on Electron Devices*, vol. 39, pp. 184-192, 1992.
- [7] S. Subramaniam, "Ion Implant Isolation of InP/InGaAs HBTs," Ph.D thesis, The University of Manchester, 2005.
- [8] F. Amin, "Design, Characterisation and Reliability of Ohmic Contacts for Heterojunction Bipolar Transistor Applications," Ph.D thesis, King's College London, 2001.
- [9] S. Chitrashekaraiah, C. N. Dharmasiri, and A. A. Rezazadeh, "An automated small-signal parameter extraction technique for HBTs using ICCAP," presented at 2004 High Frequency Postgraduate Student Colloquium, 6-7 Sept. 2004, Piscataway, NJ, USA, 2004.
- [10] A. J. Seeds and K. J. Williams, "Microwave photonics," *Journal of Lightwave Technology*, vol. 24, pp. 4628-41, 2006.
- [11] J. H. J. Wilson, *Optoelectronics: An Introduction*, 3rd ed: Prentice Hall, 1998.

- [12] H. C. Casey and M. B. Panish, "Part A: Fundamental Principles," in *Heterostructure Lasers*: Academic Press, USA 1978.
- [13] S. M. Sze, *Physics of Semiconductor Devices*, 2nd ed. USA: John Wiley & Sons, 2001.
- [14] M. S. Tyagi, *Introduction to Semiconductor Materials and Devices*: John Wiley & Sons, 1991.

Chapter 4

Spectral Response Modelling of HPTs

A key performance parameter of HPTs is their spectral response (SR) which is critical to their usage in optical applications. The modelling of SR for photodiodes has been extensively reported [1-5], however modelling of absolute spectral response of HPTs has been limited to relative or normalised cases [6-8]. This deficiency in the modelling of absolute SR is related to some simplistic assumptions taken from photodiodes and then applying these to HPTs modelling. For example, collection efficiency (η_c), which determines the amount of photons absorbed within the active structure of a phototransistor, has been considered to be unity in all previous studies [6, 8, 9] which is, largely, not the case. In p-i-n photodiodes, η_c can be taken as unity due to a large intrinsic absorption layer between p and n semiconductors. However, in surface-illuminated HPTs, η_c may not be unity due to the limitations in the vertical depth of the absorbing (base-collector depletion) region for efficient transistor action. Material properties, carrier concentrations, temperature of operation and incident photon energy may also affect η_c , thus affecting the prediction of the spectral response. Hence, a careful analysis of η_c is imperative in order to accurately model the spectral response of HPT devices.

Another parameter which affects the optical absorption significantly is the variations of absorption coefficient (α) with doping level in the device but this effect is usually not taken into account in the published literature [9, 10]. These variations, in conjunction with different rates of recombination in various layers of the transistor can make the theoretical results deviate considerably from the experimental data. Therefore, it is imperative that these aspects should be taken into account during the construction of the optical flux absorption profile (PAP) of detectors. Furthermore, subtle variations in refractive index caused by changes in the incident energy should also be incorporated. Other important parameters in the characterisation of HPTs are optical gain and noise-equivalent power (NEP). Optical gain incorporates internal

gain and the coupling efficiency of the transistor for SR modelling. NEP, along with responsivity, takes into account the leakage currents in phototransistors [11]. A thorough understanding of these parameters is paramount to the correct prediction of optical characteristics of HPTs and it is highly beneficial in the design optimisation of future phototransistors.

In this chapter, an advanced optical absorption model for single-HPTs (sHPTs) is proposed. This is then used to predict the SR and optical characteristics of an N-p-n $\text{Al}_{0.3}\text{Ga}_{0.7}\text{As}/\text{GaAs}$ HPT in two-terminal (floating base) mode. The simulated results are compared to measured data at 635 nm, 780 nm, 808 nm and 850 nm wavelengths. The generic absorption model considered should be valid for all material systems (e.g. $\text{InP}/\text{In}_{0.53}\text{Ga}_{0.47}\text{As}$) involving HPTs with minor modifications according to the material system. All these considerations have been taken into account to model the SR for $\text{InP}/\text{In}_{0.53}\text{Ga}_{0.47}\text{As}$ devices and this is compared with the measured data at 980 nm, 1310 nm and 1550 nm wavelengths.

4.1 Methodology

The spectral response and optical characteristics of N-p-n $\text{Al}_{0.3}\text{Ga}_{0.7}\text{As}/\text{GaAs}$ and $\text{InP}/\text{In}_{0.53}\text{Ga}_{0.47}\text{As}$ HPTs have been modelled by accurately predicting the proportion of photogenerated carriers produced by the incident optical signal in the base, collector and sub-collector regions of the device layer (Figure 4-1). The photocarriers lost due to recombination have been taken into account [12] and the net photogenerated carriers have then been linked to the input base current for operation of the transistor in forward-active mode. This allows the prediction of optical characteristics and SR of phototransistors. Optical flux absorption and propagation through the device layers have been analysed in detail, such that η_c and the effect of doping on absorption characteristics in various layers are incorporated for modelling. A numerical computing language (MATLAB) was used to carry out the simulations.

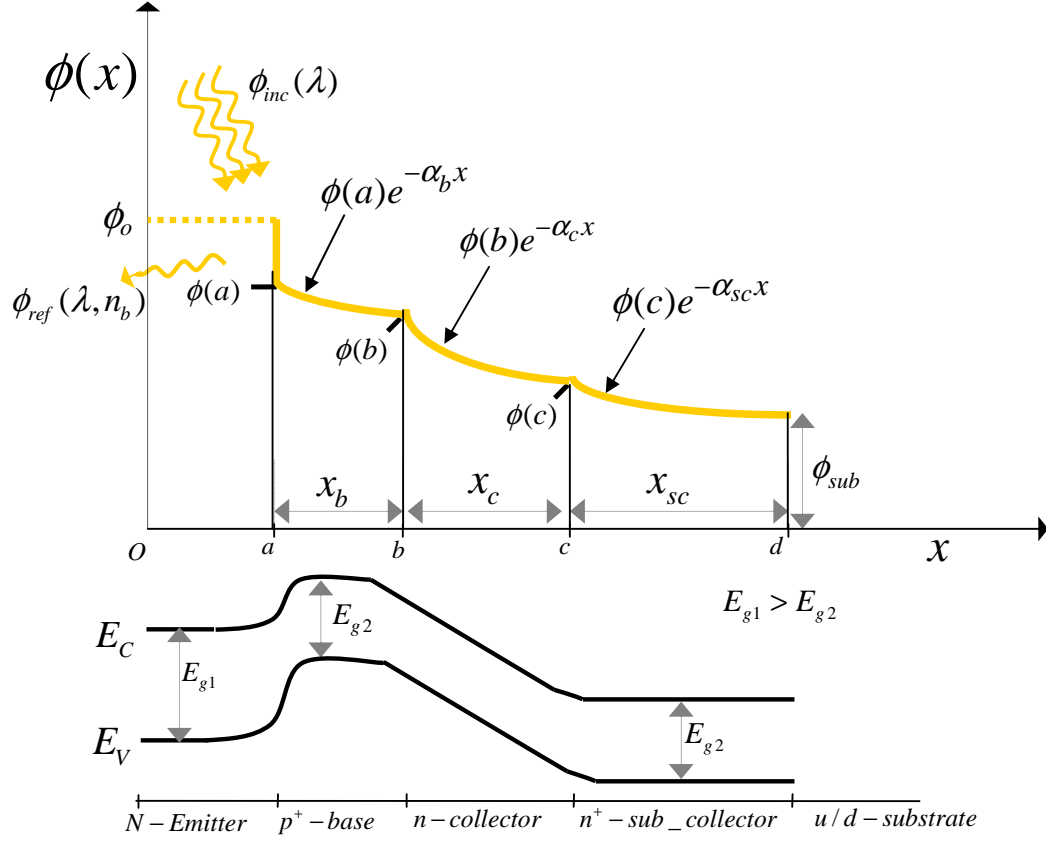


Figure 4-1. Schematic of optical flux absorption and propagation in various layers of an N-p-n HPT along with the schematic energy band diagram.

4.2 Optical Flux Absorption

Optical flux absorption is a material and wavelength-dependent phenomenon. The absorption process in various layers of an HPT depends on both the band gap of the material and the wavelength of the incident radiation. The devices under review in this section contain a single heterostructure between the base and the emitter layers. The wide band gap emitter is considered transparent, for the wavelength of interest, and the incident signal passes through the emitter and the absorption of optical power is initiated from the base layer as shown in Figure 4-1. Fresnel reflection at the air-emitter interface is thus irrelevant here as the base of the HPT is illuminated directly. The bulk collector is depleted due to a large built-in potential between the highly doped p-type base layer and a low doped n-type collector layer. From Figure 4-1, the optical absorption in the active layers of transistor has been modelled by (4.1) to (4.4).

$$\phi_{abs1} = 0 \quad (4.1)$$

$$\begin{aligned} \phi_{abs2}(\lambda, N_A) &= (\phi_{inc} - \phi_{ref}) \left[1 - e^{-(b-a)\alpha_b} \right] \\ \phi_{abs2}(\lambda, N_A) &= \phi(a) \left[1 - e^{-x_b\alpha_b} \right] \end{aligned} \quad (4.2)$$

$$\begin{aligned} \phi_{abs3}(\lambda, N_d) &= (\phi_{inc} - \phi_{ref}) \left[1 - e^{-(c-b)\alpha_c} \right] e^{-(b-a)\alpha_b} \\ \phi_{abs3}(\lambda, N_d) &= \phi(a) \left[1 - e^{-x_c\alpha_c} \right] e^{-x_b\alpha_b} \end{aligned} \quad (4.3)$$

$$\begin{aligned} \phi_{abs4}(\lambda, N_d^+) &= (\phi_{inc} - \phi_{ref}) \left[1 - e^{-(d-c)\alpha_{sc}} \right] e^{-(b-a)\alpha_b - (c-b)\alpha_c} \\ \phi_{abs4}(\lambda, N_d^+) &= \phi(a) \left[1 - e^{-x_{sc}\alpha_{sc}} \right] e^{-x_b\alpha_b - x_c\alpha_c} \end{aligned} \quad (4.4)$$

where ϕ_{abs1} , ϕ_{abs2} , ϕ_{abs3} and ϕ_{abs4} are the flux (photons/sec) absorbed in the emitter, base, collector and sub-collector of the transistor respectively. α_b , α_c and α_{sc} are the absorption coefficients (cm^{-1}) for the base, collector and sub-collector layers respectively. x_b , x_c and x_{sc} are the widths of the base, collector and sub-collector layers respectively. $\phi(a) = \phi_{inc}(\lambda) - \phi_{ref}(\lambda, n_b)$ is the value of flux at $x = a$, $\phi_{inc}(\lambda) = P_{in}/E_{ph}$ is the incident flux radiation and $\phi_{ref}(\lambda, n_b) = \phi_{inc}(\lambda)[1 - R_f(n_b)]$ is the reflected flux radiation from the base surface. $E_{ph} = hc/\lambda$ is the incident photon energy, and R_f is the Fresnel reflection coefficient [15]:

$$R_f(\lambda) = \left[\frac{(n_b - n_o)}{(n_b + n_o)} \right]^2 \quad (4.5)$$

where, n_b and n_o are the refractive indexes of the base layer and free space respectively, c is the velocity of light, h is Planck's constant and λ is the wavelength of the incident photons.

The reflected flux from the surface of the semiconductor layer can be minimized by using an antireflective coating. However, the devices under investigation did not have the coating so the effect of this has been incorporated into the analysis.

Experimentally measured data, from the literature [13-17], of optical properties for InP, InGaAs, AlGaAs and GaAs are shown in Figure 4-2.

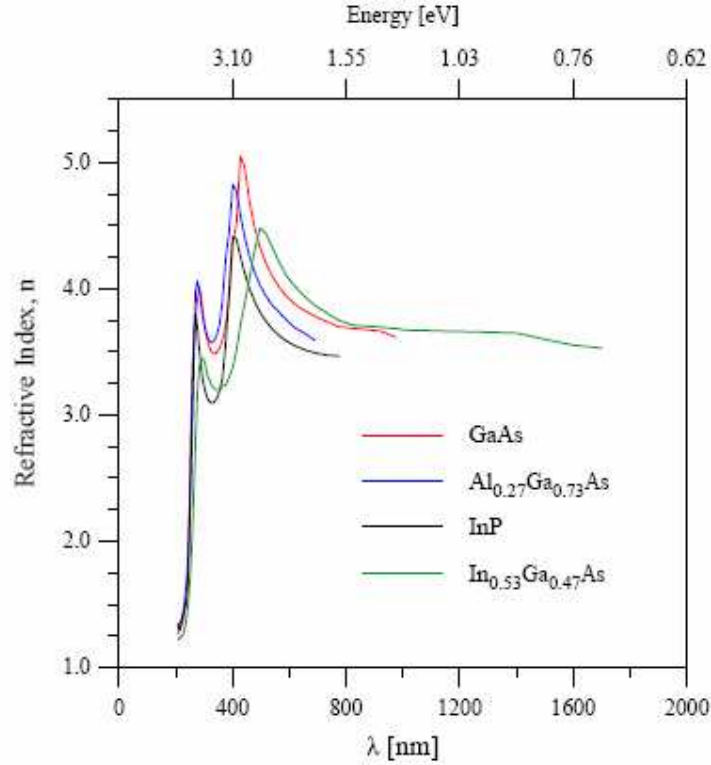


Figure 4-2. Measured refractive indices of various semiconductors as a function of incident wavelength. After [18].

From Figure 4-2 it is observed that for both the InP/InGaAs and AlGaAs/GaAs system, the refractive index for the narrower band gap material is greater than that of the large band gap counterpart for wavelengths beyond 400nm. This property is often used to design semiconductor optical waveguides, rather like optical fibers, to confine light inside a narrow band gap material which is inserted between two layers of large band gap material. Indeed, this property is often a prime advantage for edge coupled optical detectors such as double heterojunction phototransistors made from the InP/InGaAs system [18].

4.3 Absorption Coefficient

The absorption coefficient for various undoped material systems have been shown in Figure 4-3. It is useful to note that band gap variations occur with changes in the

doping concentration. At high doping concentrations, majority and minority band edges tend to undergo a noticeable shift,

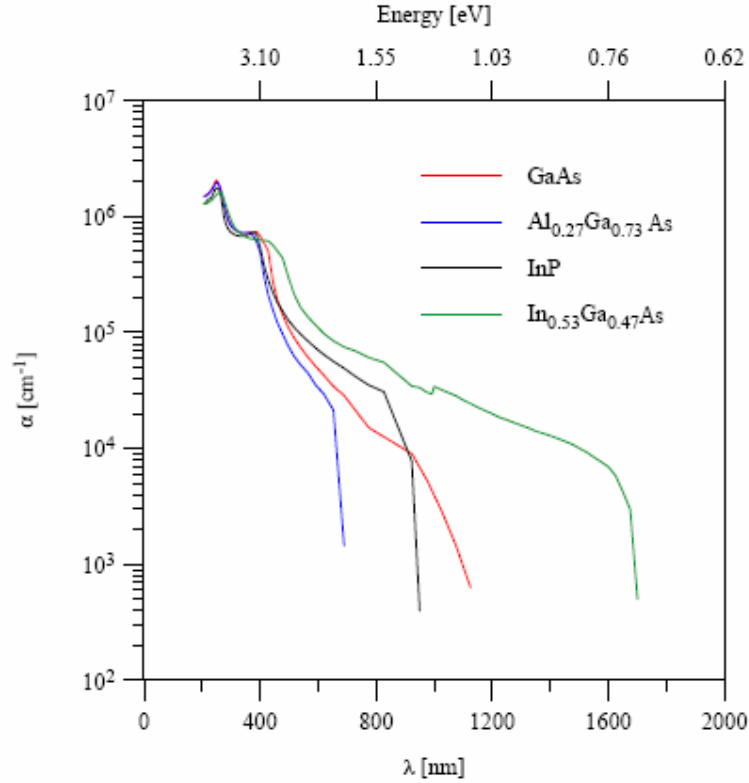


Figure 4-3. Measured absorption coefficients of various undoped semiconductor materials as function of incident wavelengths. After [18].

resulting in the reduction in the band gap of material. This is usually associated with band gap narrowing (BGN) and can have sizable impact on device characteristics. BGN affects the HPT's intrinsic characteristics as well as the absorption pattern for its various layers.

The absorption constant varies for various doping concentrations and should be accounted for in the development of the flux absorption profile. This effect is more obvious for the incident wavelengths closer to the band gap of the material. At smaller wavelengths, the effect is minimal due to the higher energy of incident photons resulting in an absorption coefficient less receptive to the incident wavelength. A detailed analysis for GaAs-based HPTs shows a considerable shift in α with different carrier concentrations and the relevant data is shown in Figure 4-4. This is a plot of absorption coefficients (for all three layers) from 800-885nm which

has been extracted from the published data [19] . From Figure 4-3 it can be seen clearly that the absorption coefficient varies for different doping levels at wavelengths closer to the band gap of GaAs (870nm). However, for wavelengths lower than 800nm the effect of doping on absorption coefficient is minimal which results in a constant value of absorption coefficient ($\alpha = 3.42 \times 10^4 \text{ cm}^{-1}$) for base, collector and sub-collector [13]. The doping dependence of absorption coefficient for the InP/InGaAs system is rather minute. A slight variation in the absorption coefficient with different carrier concentration has been seen and taken into account for the device modelling. The values are given in Table 5.2.

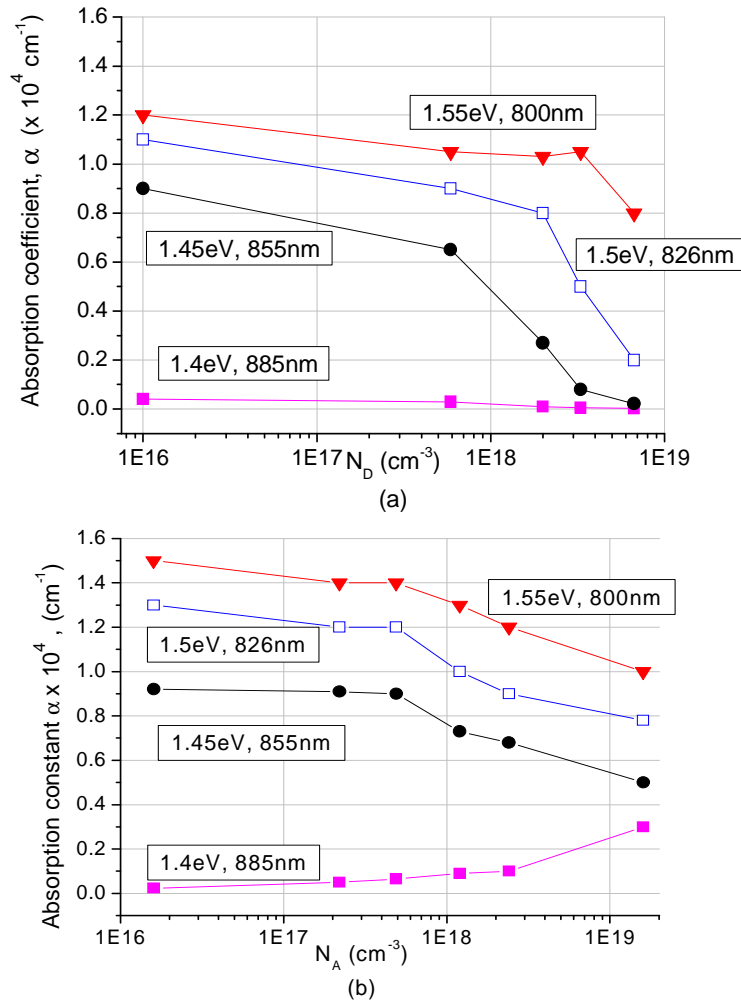


Figure 4-4. Variation of absorption coefficient, α , with doping concentrations for both (a) n- and (b) p-GaAs layers.

4.4 Collection Efficiency, η_c

η_c relates the amount of optical flux entering the base layer to the actual amount of useful flux absorbed by the device and this has been modelled by (4.6) [20]:

$$\eta_c = 1 - \frac{\phi(d)}{\phi(a)} \quad (4.6)$$

where $\phi(a)$ is the flux at the surface of the base layer and $\phi(d)$ is the value of flux at the end of the highly doped sub-collector layer (Figure 4-1). The collection efficiency, also referred to as conversion efficiency, depends on various factors such as incident signal wavelength, semiconductor doping, device material and layer widths. Maximum η_c can be achieved if all the flux is absorbed in the base, collector and the sub-collector of HPT layers and no photons propagate through to the substrate. However, due to the thickness limitation of the device layers, some flux may propagate through to the highly resistive substrate. As mentioned before, the flux absorbed in the substrate will not contribute towards the photoresponse and this will lower the responsivity, thus making η_c a vital parameter in accurate SR prediction.

4.5 Spectral Response, SR

SR specifies the responsivity of a photodetector at every incident wavelength. The responsivity, by definition, is the ratio of photogenerated current (I_{ph}) to the incident optical power (P_{in}). The first step in the modelling of SR involves the estimation of total photogenerated current (I_{ph}) resulting from optical absorption, and can be represented as [20]:

$$I_{ph} = q\beta \int_0^d (1 - R_f) \phi_o \alpha e^{-\alpha x} dx \quad (4.7)$$

where β is the internal current gain of the transistor, q is the charge of electron and $(1 - R_f) \phi_o \alpha \exp(-\alpha x)$ is the optical generation rate [3, 4] in the active layers of the device. By definition, the SR can be written as:

$$R_{spec}(\lambda) = \frac{I_{ph}}{P_{in}} \quad (4.8)$$

$$\rightarrow R_{spec}(\lambda) = \frac{q\beta}{\phi(a) E_{ph}(\lambda)} \int_0^d (1 - R_f) \phi_o \alpha e^{-\alpha x} dx \quad (4.9)$$

where $(1-R_f)\Phi_o$ is the value of input flux at $x = a$ (Figure 4-1) so it can be represented by $\Phi(a)$ and $\Phi(a)E_{ph}$ is the input power (P_{in}) at the surface base layer. No input flux will be absorbed in the wide band gap emitter (due to the incident illumination arrangement of the set-up) and the flux absorbed in the semi-insulating substrate does not contribute towards the photoresponse and can be ignored in SR prediction. Now (4.9) can be expanded to:

$$R_{spec}(\lambda) = \frac{q\beta}{\phi(a) E_{ph}(\lambda)} \left[\begin{aligned} &\alpha_b \phi(a) \int_0^{b-a} e^{-\alpha_b x} dx \\ &+ \\ &\alpha_c \phi(b) \int_0^{c-b} e^{-\alpha_c x} dx \\ &+ \\ &\alpha_{sc} \phi(c) \int_0^{d-c} e^{-\alpha_{sc} x} dx \end{aligned} \right] \quad (4.10)$$

where $\phi(b)$ and $\phi(c)$ are the values of input flux at $x = b$ and $x = c$ respectively (Figure 4-1).

Optical absorption is a distance-dependent phenomenon and hence a change in the origin (in the lower-limit of integral) is necessary for accurate prediction of SR. This modification has been proposed to the absorption model presented in the earlier work [7, 8], which was only valid for relative spectral response estimation. The electron-hole pairs generated from photon absorption in the fully-depleted collector layer will be swept across by a strong electric field towards the sub-collector and base regions respectively. Therefore, it is assumed that no recombination will occur in the depleted collector. The generation-recombination in the active regions, surface

recombination and the leakage currents are considered to be the same as in the forward-active mode of transistor operation. These effects in the neutral emitter region can also be ignored because hole injection is efficiently suppressed by the use of a wide-band gap/small-band gap (AlGaAs/GaAs or InGaAs/InP) heterostructure [21].

The slow moving photocarriers generated in the sub-collector, however, go through the process of recombination in this region. The recombination model [12] employed for this region takes into account both Auger and non-radiative (trap-assisted) recombination under the low minority carrier injection approximation (which is applicable for the HPTs in two-terminal configuration). Under these conditions R_{spec} can be written as:

$$R_{spec}(\lambda) = \frac{q\beta}{E_{ph}(\lambda)} \left\{ \left(1 - e^{-\alpha_b x_b}\right) + \frac{\phi(b)}{\phi(a)} \left(1 - e^{-\alpha_b x_b}\right) + \frac{\phi(c)}{\phi(a)} \left(1 - \frac{e^{-\alpha_{sc} x_{sc}}}{\alpha_{sc} L_p + 1}\right) \right\} \quad (4.11)$$

where L_p is the hole minority carrier diffusion length in the sub-collector. The photogenerated holes in the base region modify the emitter-base junction for the current to flow similar to the holes injected from the electrical terminal in forward active mode of operation. Therefore, the recombination in the base layer has been ignored. The predicted spectral response using (4.11) is given in Figure 4-5 along with the measured results.

4.2 Modelled and Measured Results

In this section the modelling results for the SR including collection and quantum efficiency for both material systems (GaAs and InP) are given and discussed.

4.2.1 Short Wavelength Detection

This section will include SR modelling results and analysis for the $\text{Al}_{0.3}\text{Ga}_{0.7}\text{As}/\text{GaAs}$ HPT as used for short wavelength detection. Figure 4-5 shows the predicted SR for the $\text{Al}_{0.3}\text{Ga}_{0.7}\text{As}/\text{GaAs}$ HPT along with the modelled collection and

quantum efficiencies for the entire short-wavelength spectrum. Wavelengths increment of 50 nm are used for high granularity and accurate prediction. The measured values of

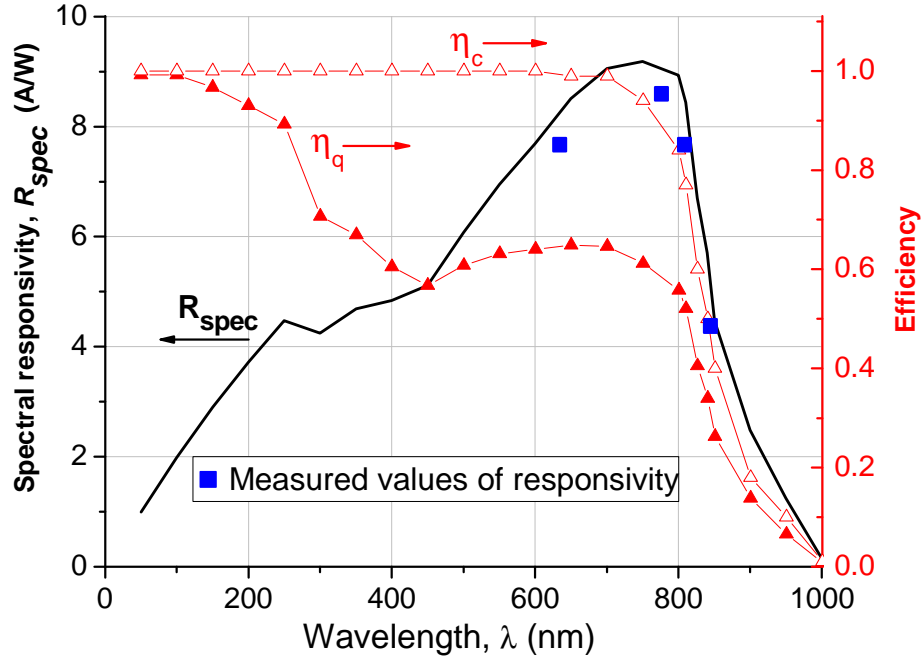


Figure 4-5. Simulated and measured (at 635 nm, 780 nm, 808 nm and 850 nm) spectral response for the $\text{Al}_{0.3}\text{Ga}_{0.7}\text{As}/\text{GaAs}$ HPT along with its collection efficiency, η_c and quantum efficiency, η_q ($V_{CE} = 2.5\text{V}$).

responsivity at 635 nm, 790 nm, 808 nm and 850 nm show very good agreement to the predicted data. The base region of the phototransistor under investigation has been illuminated directly and so it is assumed that no input flux gets absorbed in the emitter region. However, if modelling is performed for absorption through transparent contacts and a wide band gap emitter then the responsivity will be lower below 680 nm which corresponds to the band gap of the $\text{Al}_{0.3}\text{Ga}_{0.7}\text{As}$ emitter layer (1.8 eV). This will occur as most of the incident signal below 680 nm will be absorbed in the wide band gap emitter and does not go through amplification under the transistor action. Material properties such as absorption coefficient and refractive index used for simulation are taken from [13, 19]. In order to analyse the spectral response data in Figure 4-5, it has been divided into three wavelength regions:

- The first region (0-350 nm) shows increasing responsivity, R , and decreasing η_q . R rises with incident flux rate (photons/sec) which increases with wavelength for constant optical power. At the same time η_c tends to unity with photon absorption taking place in the base and collector layers. η_q decreases due to the increase in the refractive index of GaAs with increasing wavelengths [13].
- The second region (350-700 nm) shows rising R and nearly constant η_q . R rises as incident flux rate increases and η_c tends to unity. η_q remains fairly constant due to minimal variation of refractive index in this wavelength region for the GaAs base layer.
- The third region (700-1000 nm) is most significant since it contains the short wavelength of transmission (850 nm). Theoretically, the threshold wavelength for GaAs photodetectors should be around 870 nm. However, it can be seen in Figure 4-5 that R and η_q start decreasing well before 870 nm for two reasons. Firstly, band gap variation occurs with doping which lowers the threshold wavelength. This is incorporated by adding the effect of doping on the absorption coefficient for GaAs [19]. Secondly and more importantly, η_c falls significantly at around 775 nm which causes R and η_q to drop.

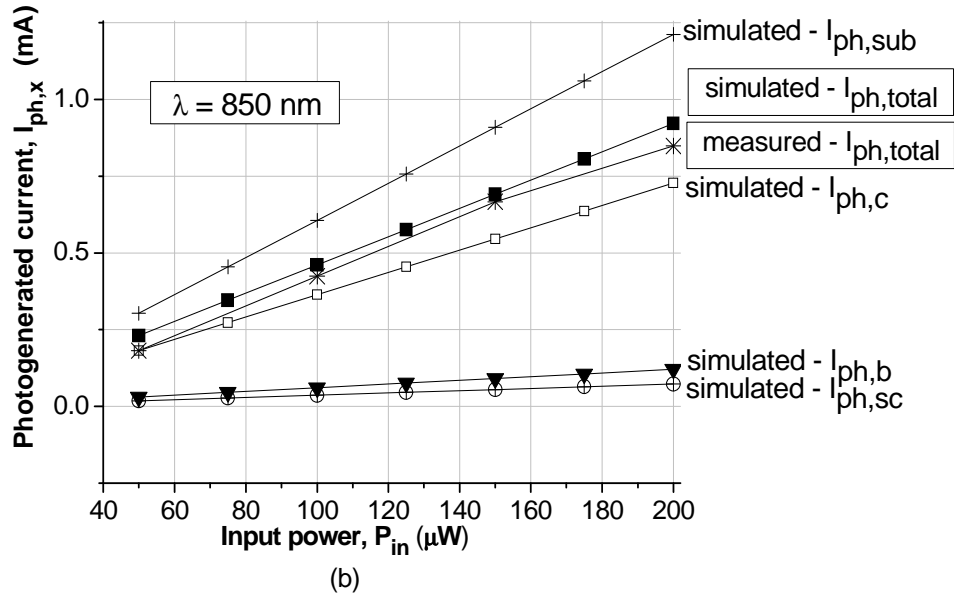
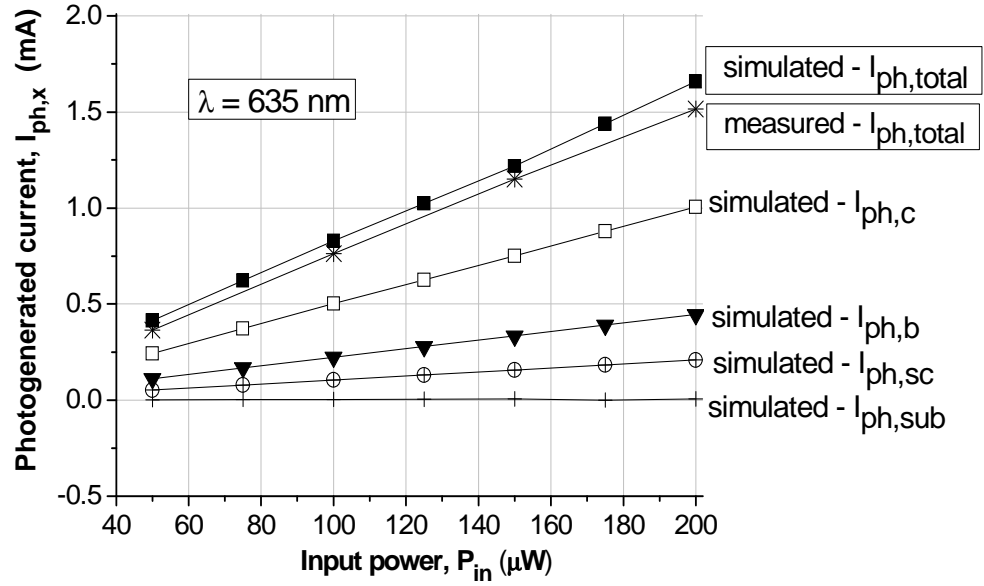


Figure 4-6. Measured and simulated photogenerated currents with input optical power for various $Al_{0.3}Ga_{0.7}As/GaAs$ HPT layers at (a) 635nm and (b) 850nm ($V_{CE} = 2.5$ V).

In order to analyse η_c , the responsivity of every absorbing layer should be taken into account. η_c is strictly wavelength and device vertical width dependent parameter. For the device under consideration, the vertical depth is constant so the effect of incident wavelength is studied for investigation of η_c . Two wavelengths, 635nm and 850 nm, are used for the analysis of collection efficiency. Figure 4-6 shows the current-power

relationship of each layer at various incident powers. The total photogenerated current ($I_{ph,total}$) at 635nm is higher than that at 850 nm for the same input power. This is due to the increased photo-absorption in the substrate at 850 nm which does not contribute towards the photoresponse. In other words, η_c at 635 nm is very close to unity since a very small amount of flux propagates through to the substrate, resulting in a high responsivity. However at 850 nm, η_c slumps to less than 50% as flux absorption in the substrate dominates. Thus, both responsivity and quantum efficiency suffer as a consequence and this is clearly illustrated through Figures 4-5 and 4-6. Collection efficiency has been modelled, in terms of flux propagation through the device, by (4.6). However, it can also be written in terms of responsivities of each absorbing layer and is modelled as:

$$\eta_c(\lambda) = \frac{R_b(\lambda) + R_{cl.}(\lambda) + R_{scl.}(\lambda)}{R_b(\lambda) + R_{cl.}(\lambda) + R_{scl.}(\lambda) + R_{sub}(\lambda)} \quad (4.12)$$

where R_b , $R_{cl.}$, R_{scl} and R_{sub} are the responsivity contribution of base, collector, sub-collector and substrate respectively (R_{sub} not contributing towards the photoresponse). In order to achieve higher collection efficiency and in turn higher responsivity at 850 nm, the device layers should be re-designed. However, this directly affects the performance of the phototransistor and therefore careful optimization is necessary to design an optimal phototransistor.

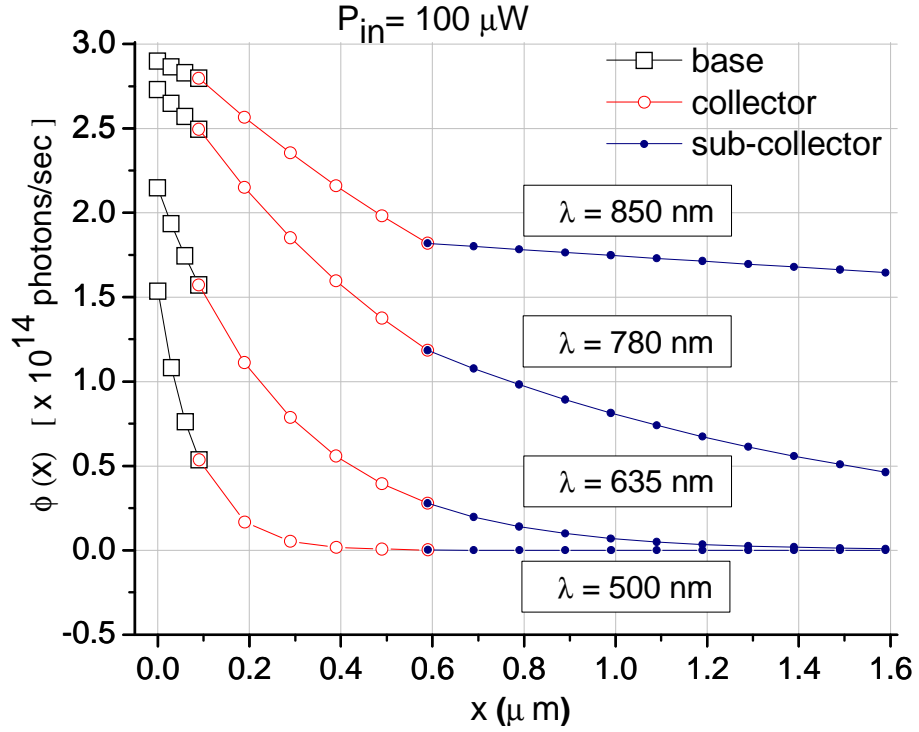


Figure 4-7. Optical flux absorption profile for the $Al_{0.3}Ga_{0.7}As/GaAs$ HPT at various incident wavelengths for incident power of $100 \mu W$.

The optical flux absorption profile for the $Al_{0.3}Ga_{0.7}As/GaAs$ sHPT at 500 nm, 635 nm, 780 nm and 850 nm has been constructed in Figure 4-7. The photo-absorption in each layer at 850 nm varies due to different absorption coefficients and absorption widths of the device layers. The rapid absorption in the collector layer results from a larger absorption coefficient ($\alpha_c = 8.5 \times 10^3 \text{ cm}^{-1}$) than that of the base ($\alpha_b = 5 \times 10^3 \text{ cm}^{-1}$) and the sub-collector ($\alpha_{sc} = 0.2 \times 10^3 \text{ cm}^{-1}$). However, at 635 nm and 500 nm the absorption coefficient is independent of doping and thus can be modelled as a single-exponential [19]. At 780 nm, the response tends to shift from single-exponential to layer dependent absorption and the variation in α is minute.

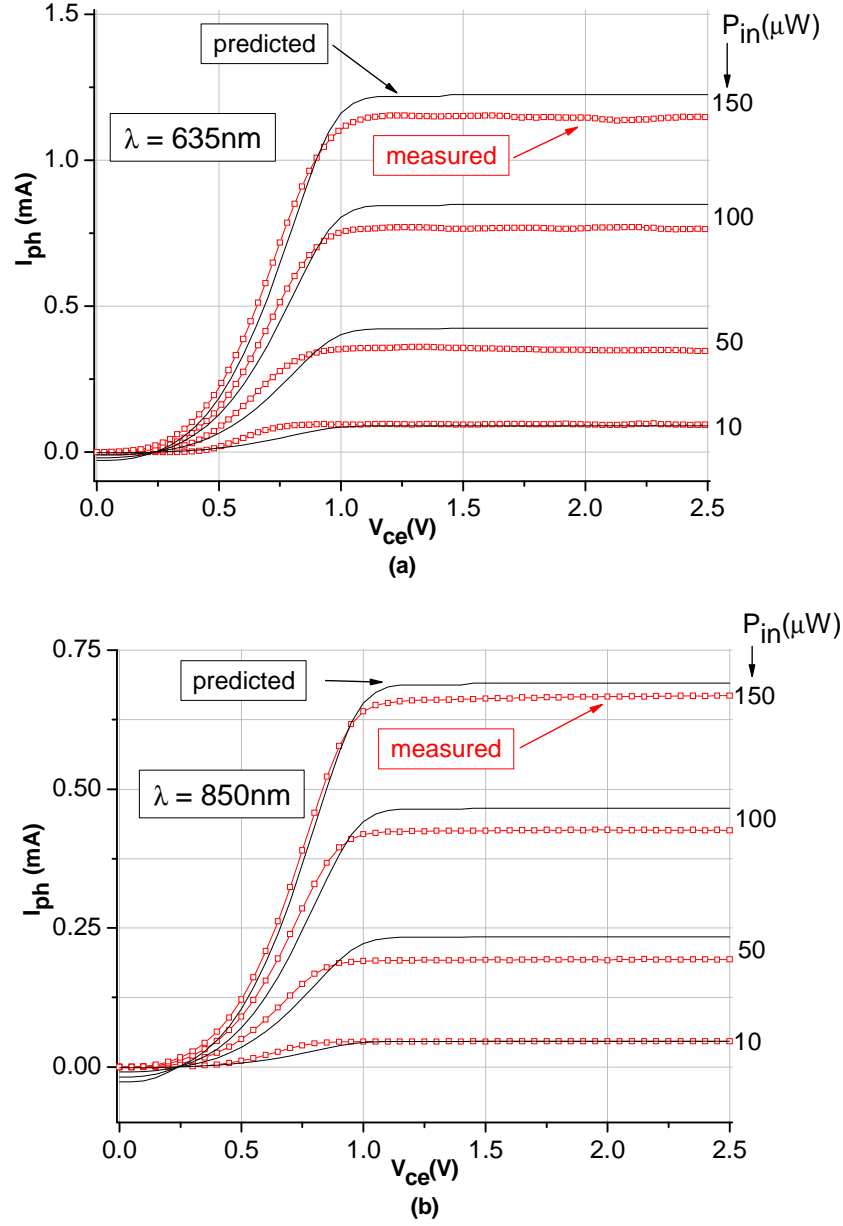


Figure 4-8. Measured and modelled output characteristics of the $Al_{0.3}Ga_{0.7}As/GaAs$ HPT at various input optical power for (a) 635nm and (b) 850nm.

Finally, the optical characteristics for the $Al_{0.3}Ga_{0.7}As/GaAs$ HPT at 635 nm and 850 nm are shown in Figure 4-8. The detailed absorption model, presented in this work, allows the accurate prediction of photocarriers in the active layers of the phototransistor which, when related to the base current of transistor in the forward active mode, enables the prediction of optical characteristics. A detailed MATLAB

program used to predict optical characteristics is presented in Appendix D of the thesis. Close agreement between the measured and predicted photocurrents is observed as the effect of doping and change in the collection efficiency are incorporated for the absorption model. Some discrepancy between the measured and predicted optical characteristics may be due to slight doubt in the coupling of optical fibre to the device.

4.2.2 Long Wavelength Detection

GaAs-based material systems can only detect signals for wavelengths shorter than about 870 nm. Therefore, for Long and medium wavelength detection InGaAs based device are usually used. The device under investigation is a lattice matched InP/In_{0.47}Ga_{0.53}As system and the SR model has been used to calculate the responsivity of these devices.

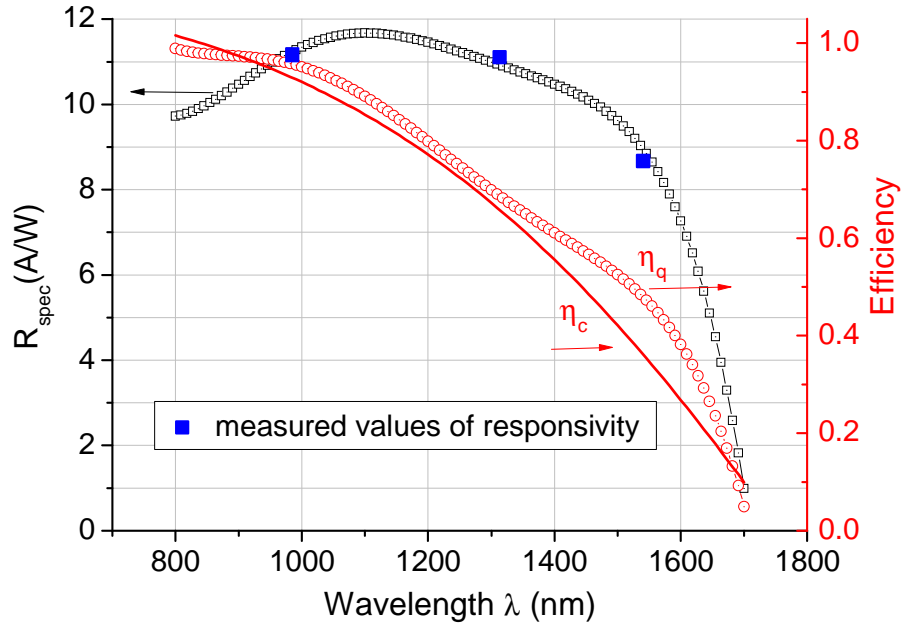


Figure 4-9. Simulated and measured (at 980 nm, 1310 nm and 1550 nm) spectral response for the InP/In_{0.47}Ga_{0.53}As HPT along with its collection efficiency, η_c and quantum efficiency, η_q ($V_{CE} = 2$ V).

Figure 4-9 shows the predicted SR for the InP/In_{0.47}Ga_{0.53}As HPT along with the modelled collection and quantum efficiencies for the long wavelength spectra. The

measured values of responsivity at 980 nm, 1310 nm and 1550 nm have also been shown on the plot and show good agreement with the theoretical data. The InP emitter is considered transparent and the absorption starts from the base region. In principle, two terminologies can be used to state this claim. First, if the emitter contact is made transparent (window effect) then there is selective absorption depending on the wavelength of the incident radiation [11, 18]. This implies that if the energy of the incident photon is smaller than the energy-gap of emitter, then the radiation will reach the base unattenuated (no photo-absorption occurs in the wide band gap emitter). A second possible alternative is to illuminate the base layer directly with external radiation to excite the carriers. As per the design of HPTs and experimental orientation, the second scheme is employed in this work. From Figure 4-9, it can be inferred that the responsivity is higher in the 980-1300 nm wavelength region as the absorption coefficient is higher and the photon influx is constantly increasing. Responsivity gradually lowers with increasing wavelengths and the cut-off wavelength of detection for the device under investigation is around 1700 nm.

Collection efficiency on the other hand falls sharply as the wavelength increases, unlike the GaAs-based devices discussed in section 4.2.2. This is mainly due to the fact that the layer structure is different for both devices and therefore a direct comparison is not appropriate. However, it gives a good reference for the devices having a smaller absorption layer width resulting in lower collection efficiency. The quantum efficiency is also been shown in Figure 4-9 and it decreases gradually with wavelength due to the decrease in both photo-generated current and with increasing wavelengths and the collection efficiency.

The optical flux absorption profile of the InP/In_{0.47}Ga_{0.53}As HPT is shown in Figure 4-10. The absorption at 800nm and 980nm is same for the three absorbing layers as the absorption coefficient for the layers is constant ($\alpha(800\text{nm}) = 6\mu\text{m}^{-1}$ and $\alpha(980\text{nm}) = 4\mu\text{m}^{-1}$) [18]. However, the effect of change in absorption coefficient at 1310nm and 1550nm is obvious from Figure 4-10. In this case, the absorption is layer dependent and the absorption coefficients for base, collector and sub-collector at 1300 (1550) nm are $1.55 (0.85)\mu\text{m}^{-1}$, $1.16 (0.68)\mu\text{m}^{-1}$ and $1.16 (0.68)\mu\text{m}^{-1}$ respectively [16]. With reference to Figure 4-1, the flux propagation, $\Phi(x)$ in

different layers of the device can be written as (4.13) and has been used to model the optical PAP in Figure 4-10.

$$\phi(x) = (\phi_{inc} - \phi_{ref}) \begin{cases} \exp(-\alpha_b x) & ; 0 \leq x \leq x_b \\ \exp(-\alpha_c x) - \exp(-\alpha_b x_b - \alpha_c x) & ; x_b < x \leq x_b + x_c \\ \exp(-\alpha_c x_c - \alpha_{sc} x) - \exp(-\alpha_b x_b - \alpha_c x_c - \alpha_{sc} x) & ; x_b + x_c < x \leq x_b + x_c + x_{sc} \\ 0 & ; x_b + x_c + x_{sc} < x \end{cases} \quad (4.13)$$

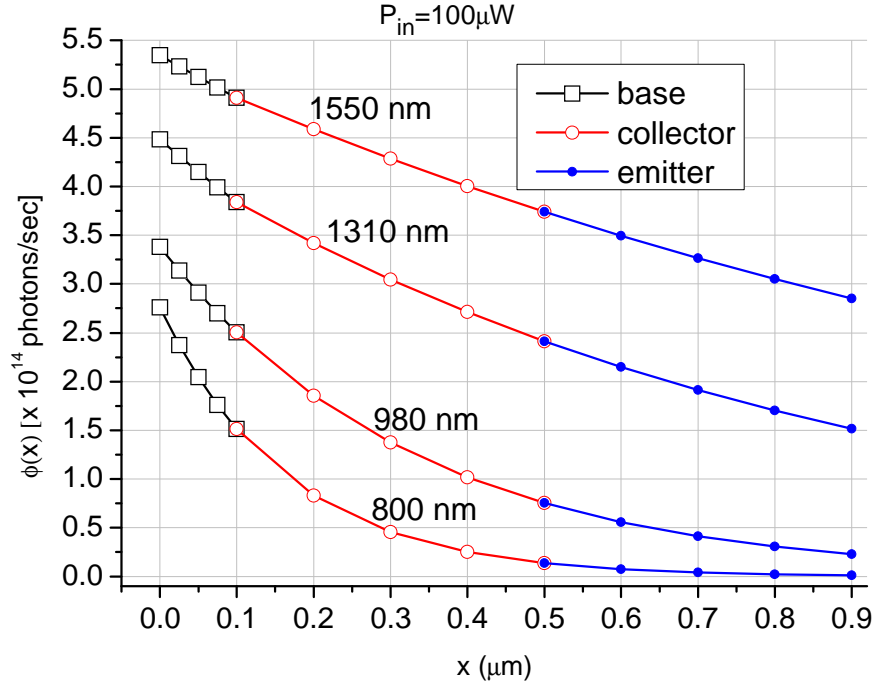


Figure 4-10. Optical flux absorption profile for the InP/In_{0.47}Ga_{0.53}As HPT at various incident wavelengths for incident power of 100 μW.

Figure 4-11 shows the photogenerated current at different input optical powers. Close agreement between the measured and predicted photocurrents is observed due to the detailed absorption analysis performed for these devices. It can be seen that the turn-on voltage for these devices is significantly lower than those of GaAs-based devices seen in Section 4.2.1. This mainly occurs due to the inherent advantage of the InP/InGaAs material system with a smaller base region band gap resulting in lower turn-on voltage and offset voltage and in turn lower power dissipation in MMIC circuits [22].

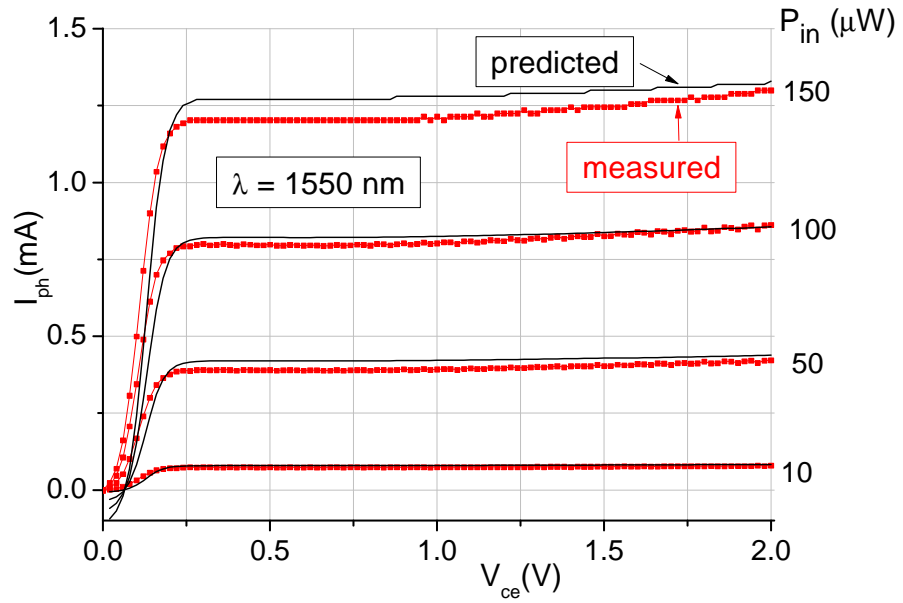
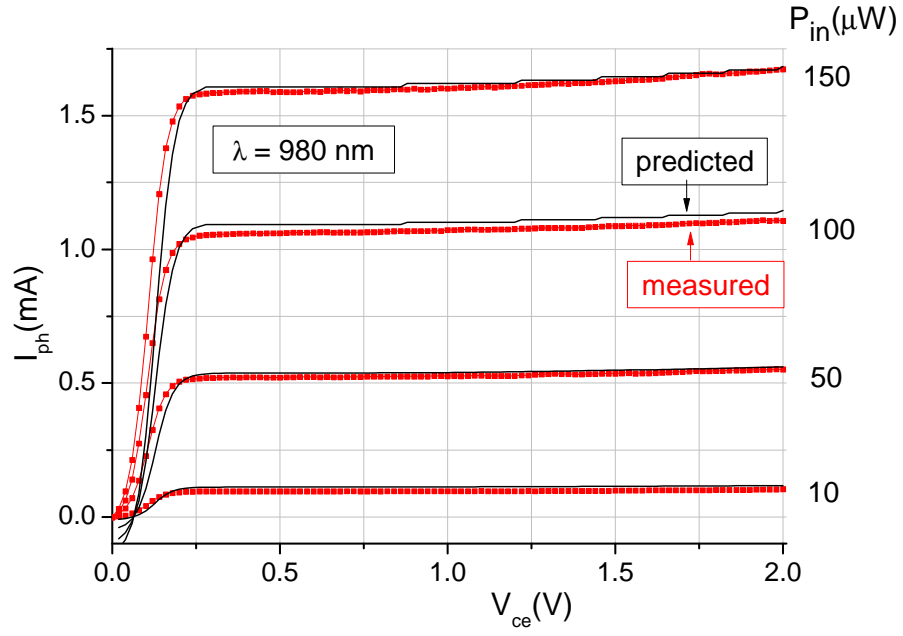


Figure 4-11. Measured and modelled output characteristics of the *InP/In_{0.47}Ga_{0.53}As* HPT at various input optical power for (a) 980nm and (b) 1550nm.

References

- [1] A. M. Bouhdada, R. Vigue, F. Faurie, J.-P., "Modeling of the spectral response of PIN photodetectors impact of exposed zone thickness, surface recombination velocity and trap concentration," *Microelectronics Reliability*, vol. 44, pp. 223-8, 2004.
- [2] M. B. Hanzaz, A. Monroy, E. Munoz, E. Gibart, P. Omnes, F., "Modeling of the spectral response of $\text{Al}_x\text{Ga}_{1-x}\text{N}$ p-n junction photodetectors," *European Physical Journal, Applied Physics*, vol. 11, pp. 29-34, 2000.
- [3] J. A. R. Gonzalez-Cuevas, Tamer F. Abedin, M. Nurul Elsayed-Ali, Hani E., "Modeling of the temperature-dependent spectral response of $\text{In}_{1-x}\text{Ga}_x\text{Sb}$ infrared photodetectors," *Optical Engineering*, vol. 45, pp. 044001, 2006.
- [4] H. Zheng, K. Yong, T. Ying-Wen, L. Xue, and F. Jia-Xiong, "Study on the spectral response of the Schottky photodetector of GaN," *Chinese Physics*, vol. 15, pp. 1325-9, 2006.
- [5] K.-S. Lai, J.-C. Huang, and K. Y.-J. Hsu, "Design and properties of phototransistor photodetector in standard 0.35- μm SiGe BiCMOS technology," *IEEE Transactions on Electron Devices*, vol. 55, pp. 774-81, 2008.
- [6] L. E. M. de Barros, Jr. Paoletta, A. Frankel, M.Y. Romero, M.J. Herczfeld, P.R. Madjar, A., "Photoresponse of microwave transistors to high-frequency modulated lightwave carrier signal," *IEEE Transactions on Microwave Theory and Techniques*, vol. 45, pp. 1368-74, 1997.
- [7] S. A. Bashar and A. A. Rezazadeh, "Characterisation of transparent ITO emitter contact InP/InGaAs heterojunction phototransistors," presented at Proceedings of the 3rd IEEE International Workshop on High Performance Electron Devices for Microwave and Optoelectronic Applications, EDMO 95, 27 Nov. 1995, London, UK, 1995.
- [8] S. A. Bashar and A. A. Rezazadeh, "Fabrication and spectral response analysis of AlGaAs/GaAs and InP/InGaAs HPTs with transparent ITO emitter contacts," *IEE Proceedings-Optoelectronics*, vol. 143, pp. 89-93, 1996.
- [9] A. A. de Salles, A. S. Hackbart, and L. N. Spalding, "A simple model for the GaAs HBT high-frequency performance under optical illumination," *Microwave and Optical Technology Letters*, vol. 7, pp. 392-5, 1994.

- [10] R. F. Sridhara, S.M. Roenker, K.P. Pan, N. Elliott, J., "Performance enhancement of GaInP/GaAs heterojunction bipolar phototransistors using dc base bias," *Journal of Lightwave Technology*, vol. 16, pp. 1101-6, 1998.
- [11] H. A. Khan, A. A. Rezazadeh, and S. C. Subramaniam, "Spectral response modelling of heterojunction phototransistors for short wavelength transmission," presented at 2008 European Microwave Integrated Circuit Conference, EuMIC 2008, October 27, 2008 - October 31, 2008, Amsterdam, Netherlands, 2008.
- [12] N. Chand, P. A. Houston, and P. N. Robson, "Gain of a Heterojunction Bipolar Phototransistor," *IEEE Transactions on Electron Devices*, vol. ED-32, pp. 622-627, 1985.
- [13] G. B. Lush, "Properties of GaAs," in *EMIS data review series*, 2nd ed: Inspec publications, 1990, pp. 513-528.
- [14] "Optical Functions of Intrinsic InP : General Remarks," in *Properties of Indium Phosphide*: INSPEC, EMIS Data Review Series No. 6, 1991, pp. 105 - 137.
- [15] S. Adachi, "Optical Functions of InGaAsP : Tables," in *Properties of Indium Phosphide*: INSPEC, EMIS Data Review Series No. 6, 1991, pp. 416 - 428.
- [16] D. A. Humphreys, R. J. King, D. Jenkins, and A. J. Moseley, "Measurement of absorption coefficients of Ga_{0.47}In_{0.53}As over the wavelength range 1.0-1.7 μ m," *Electronics Letters*, vol. 21, pp. 1187-9, 1985.
- [17] D. E. Aspnes, S. M. Kelso, R. A. Logan, and R. Bhat, "Optical properties of Al_xGa_{1-x}As," *Journal of Applied Physics*, vol. 60, pp. 754-67, 1986.
- [18] S. A. Bashar, "Study of Indium Tin Oxide (ITO) for Novel Optoelectronic Devices," Ph.D thesis, King's College London, 1998.
- [19] H. C. J. Casey, D. D. Sell, and K. W. Wecht, "Concentration dependence of the absorption coefficient for n- and p-type GaAs between 1.3 and 1.6 eV.," *Journal of Applied Physics*, vol. 46, pp. 250-257, 1975.
- [20] H. A. Khan and A. A. Rezazadeh, "Spectral response modelling of GaAs-based heterojunction phototransistors for short wavelength detection," *Optoelectronics, IET*, vol. 4, pp. 57-63, 2010.
- [21] S. Tiwari, S. L. Wright, and A. W. Kleinsasser, "Transport and related properties of (Ga,Al)As/GaAs double heterostructure bipolar junction

transistors," *IEEE Transactions on Electron Devices*, vol. ED-34, pp. 185-98, 1987.

- [22] H. Sheng, "Modelling, Fabrication and Characterisation of InP-HBTs for Future High-Speed, Low-Power Optical Telecommunications," Ph.D thesis, King's College London, 2000.

Chapter 5

Analytical Modelling of the Spectral Response

A renewed interest in HPTs has been seen in the past decade for their use in the front-end of optoelectronic monolithic microwave/millimetre-wave integrated circuit (OEMMIC) optical receivers based on HBTs [1-5]. Monolithic integration implies that the detectors (HPTs/photodiodes) and amplifiers (HBTs) share common epitaxial layers or device layers are grown on top of each other [6]. The latter process is cost ineffective which makes it unattractive for industrial manufactures of photoreceivers. On the other hand, in the shared epitaxial structures, the compatibility of HPTs with HBTs in fabrication methods makes them highly attractive in the manufacturing of high-speed photoreceivers. However, the inevitable design tradeoffs degrade the receiver performance[7, 8]. Hence, there is a need to critically analyse several important parameters of these devices which can further revolutionise their use and extend their range of functionality from ordinary sensors to high speed optical networks.

To date, most receiver designs have employed p-i-n photodiodes as photodetectors. However, these devices exhibit no internal (intrinsic) gain and the increased capacitance due to large intrinsic absorption layer is known to be the limiting factor for high frequency operation of the photoreceivers. Metal-semiconductor-metal (MSM) photodiodes, on the other hand, have low capacitance per unit area relative to p-i-n photodiodes (due to a Schottky-like contact) which make them suitable for high frequency operation [10]. However, their temperature instability, lack of internal gain and complicated epitaxial growth and fabrication process make their use limited [11, 12]. The advantage of HPTs over avalanche photodiodes (APDs) is evident from their low noise operation along with their relatively simple biasing conditions as compared to APDs. Other devices such as MESFETs and HEMTs have also been considered for photoreceivers but their high frequency operation (millimetre-wave

and beyond) still remains an issue [13]. In summary, HPTs provide an exciting alternative to the above mentioned devices for the manufacture of high speed optical receivers based on HBTs [14, 15].

Spectral responsivity modelling for photodiodes has been extensively investigated and reported [16-19]. Bouhdada *et al.* [16] have modelled the responsivity of p-i-n photodiodes with the impact of surface recombination velocity. Hanzaz *et al.* [17] have performed the same task for $\text{Al}_x\text{Ga}_{1-x}\text{N}$ p-n junction photodiodes and have also discussed the influence of doping on the exposed zone thickness. A spectral response model for Schottky photodiodes has been reported by Zheng *et al.* [18] and the temperature dependent model for infrared photodiodes has been analysed by Gonzales-Cuevas *et al.* [19]. In contrast, analytical modelling of the spectral response for HPTs is rather limited. Chand *et al.* [20] have formulated analytical expressions for responsivity, however the boundary conditions in their investigation are highly implausible for efficient HPT operation and no experimental comparison has been provided. Several other attempts at predicting SR have been either limited to the relative or normalized response [21, 22] or they require prior knowledge of device electrical characteristics [23, 24].

In this chapter, we formulate expressions for flux dependent collector current, and in turn responsivity for HPTs along with a detailed analysis on $\text{Al}_{0.3}\text{Ga}_{0.7}\text{As}/\text{GaAs}$ and $\text{InP}/\text{In}_{0.47}\text{Ga}_{0.53}\text{As}$ HPTs. This analysis gives insight into the direct influence of different parameters (base width, carrier concentration etc.) on the device performance, thus, providing a valuable optimization tool for the future design of HPTs in optical receivers.

5.1 Device Modelling

The SR model is based on a formulation of the semiconductor continuity equations with suitable boundary conditions at the junctions of the active device layers. The SR modelling must take into account all of the related physical parameters. The effect of doping on the absorption coefficient at near band gap wavelengths has been taken into account along with the subtle variation of refractive index caused by the changes

in incident photon energies. The schematic for a phototransistor ($\text{Al}_{0.3}\text{Ga}_{0.7}\text{As}/\text{GaAs}$ HPT) structure is shown in Figure 5-1.

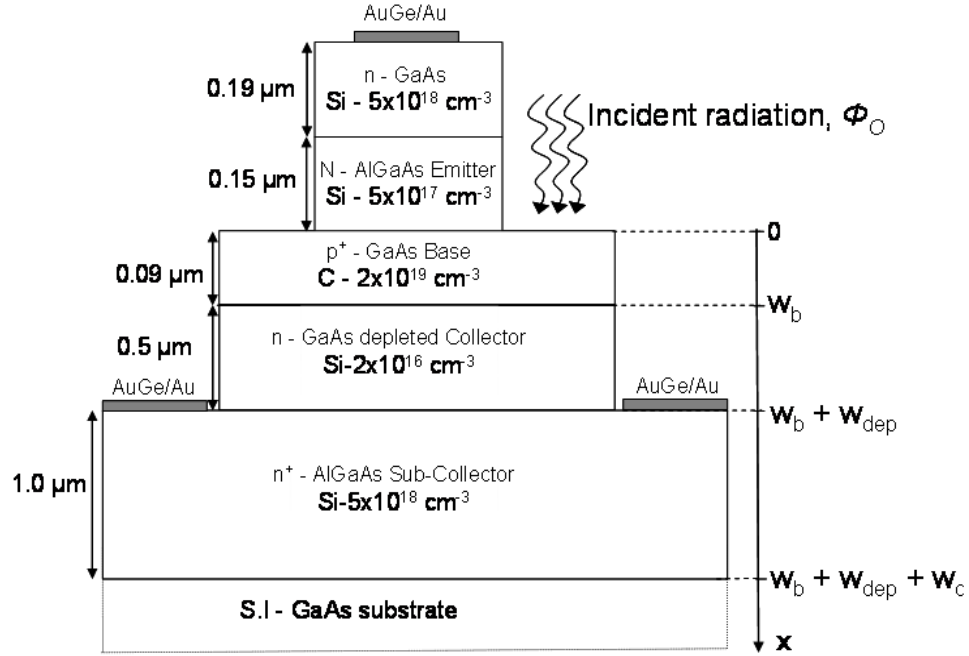


Figure 5-1. Schematic device structure of the $\text{Al}_{0.3}\text{Ga}_{0.7}\text{As}/\text{GaAs}$ HPT showing the incident radiation on the base region.

The base surface of the device has been illuminated using an optical fibre and the incident flux is absorbed through the optical window between emitter and collector contacts. The photo-absorption occurring in the base-collector depletion region and within the diffusion lengths of minority carriers will contribute towards the photoresponse. The steady state continuity equations governing the distribution of minority carriers for low-injection state will be discussed in the next section. These incorporate drift and diffusion mechanism of excess minority carriers along with the photo-generation and recombination effects.

5.1.1 Semiconductor Continuity Equation

The basic continuity equation for semiconductor device operation describes the behaviour of carriers in the semiconductor under the influence of an external electric field that cause the deviation from thermal-equilibrium conditions [25]. When excess

carriers are introduced in a region of a semiconductor, their concentration will be affected by recombination and by flowing out of the volume, if an electrical contact is provided. Similarly, the numbers of carriers inside the volume can be increased by photogeneration as well as by flux of carriers into the volume [26]. The rate at which the electron (hole) concentration changes in the p (or n) type semiconductor is given by (5.1) and (5.2) [27]:

$$\frac{\delta n}{\delta t} = G_n - R_n + \nabla \cdot \frac{J_n}{q} \quad (5.1)$$

$$\frac{\delta p}{\delta t} = G_p - R_p - \nabla \cdot \frac{J_p}{q} \quad (5.2)$$

where, G_n and G_p are the electron and hole generation rate, respectively, caused by external influence such as the optical excitation or impact ionization under large electric fields. The electron (or hole) recombination rate in a p (or n) type semiconductor is R_n (R_p). The electron (hole) concentration, n (or p) increases with time, t if more electron (holes) are generated than destroyed. J_n and J_p are the electron and hole current densities respectively consisting of a diffusion current due to a gradient in the density (from higher to lower concentrations due to Fick's Law) and a drift current due to the applied electric field, E [28]:

$$J_n = q\mu_n nE + qD_n \frac{dn}{dx} \quad (5.3)$$

$$J_p = q\mu_p pE - qD_p \frac{dp}{dx} \quad (5.4)$$

The diffusion coefficient (D) and the mobility (μ) for both electrons and holes are related by the Einstein relationship [29]:

$$D_n = \frac{kT}{q} \mu_n \quad (5.5)$$

$$D_p = \frac{kT}{q} \mu_p \quad (5.6)$$

where q is unit charge, k is Boltzmann constant and T is the absolute temperature.

The continuity equations in (5.1) and (5.2) become,

$$\frac{\delta n}{\delta t} = G_n - R_n + \mu_n n \frac{\partial E}{\partial x} + \mu_n E \frac{\partial n}{\partial x} + D_n \frac{\partial^2 n}{\partial x^2} \quad (5.7)$$

$$\frac{\delta p}{\delta t} = G_p - R_p - \mu_p p \frac{\partial E}{\partial x} - \mu_p E \frac{\partial p}{\partial x} + D_p \frac{\partial^2 p}{\partial x^2} \quad (5.8)$$

5.1.2 Basic Assumptions

Equations (5.7) and (5.8) are applicable for a three-dimensional analysis of transistor operation. To describe the electrical characteristics of practical transistors reasonably accurately, a one-dimensional approach is sufficient, although even this is complicated [28]. Consequently, for compact device modelling, certain assumptions can be made to simplify the mathematics considerably, for instance in (5.7) and (5.8) steady state conditions can be applied which imply:

$$\frac{\delta n}{\delta t} = 0$$

and

$$\frac{\delta p}{\delta t} = 0$$

The HPTs under consideration are uniformly doped and therefore it can be assumed that there are no built-in electric fields outside the depletion regions. In addition, the doping in the bulk semiconductor regions is high enough to ensure high conductivity so that the voltages only drop across the depletion zones. This ensures that carriers move under the influence of diffusion only and the electric field can be set to zero.

5.1.3 Photogeneration

Photogeneration occurs in the semiconductor device due to incident optical illumination if the energy of the incident photons is larger than the band gap of the semiconductor material. It has been assumed that there is no (or very little compared to optical generation) thermal generation of carriers other than that due to optical absorption in the device active layers. The optical generation rate can be modelled by (5.9) [27]:

$$G(x) = \phi_o \alpha e^{-\alpha x} \quad (5.9)$$

where, ϕ_o is the incident flux density and α is the absorption coefficient of the semiconductor material.

5.1.4 Carrier Recombination

The recombination in a semiconductor material, on the other hand, is due to three processes. Taking the base region of an Npn HPT as an example, the three types of recombination can be written as [25]:

- **Radiative Recombination :** $R_{Rad} = B(np - n_i^2)$ (5.10)

- **SRH Recombination :** $R_{SRH} = \frac{pn - n_i^2}{\tau_{SRH} (n + p + 2n_i)}$ (5.11)

- **Auger Recombination :** $R_A = C(n + p)(np - n_i^2)$ (5.12)

where B , τ_{SRH} and C are the recombination coefficients.

5.1.4.1 Radiative Recombination

R_{rad} , also known as band-to-band recombination, occurs when an electron drops directly from the conduction into an unoccupied state in the valence band. This mostly occurs in direct band gap semiconductors. The emission occurs as a photon which has energy equivalent to the band gap of the semiconductor material. In an indirect band gap semiconductor, band-to-band transitions involve a large change in electron momentum, and the momentum conservation condition requires either emission or absorption of a phonon. Consequently, direct band to band recombination has a very low probability in indirect semiconductors [26] .

5.1.4.2 SHR Recombination

Impurity atoms (other than donors and acceptors) and some types of crystal defects in a semiconductor introduce localized energy levels deep in the band gap away from

the edges [26]. Indirect recombination takes place when an electron makes a transition to such an energy level, lying deep in the band gap, and it subsequently captures a hole from the valence band. In the process of electron-hole pair recombination, the energy equal to the difference between the electron and hole is released. This energy can be emitted as a photon (radiative recombination) or as dissipated energy to the lattice in the form of phonons. This mechanism of recombination through deep level centres has been investigated by Shockley, Reed and Hall [30, 31] and is also referred to as Shockley-Reed-Hall recombination (R_{SRH}).

5.1.4.3 Auger Recombination

Auger recombination is a three-particle process involving two electrons and a hole or two holes and an electron. The energy released by electron-hole pair recombination is imparted as kinetic energy to another free electron or hole. Auger process is non-radiative and this type of recombination is possible for both direct band to band and indirect recombination process involving traps [25].

During device operation, the minority electron concentration in the heavily doped p-type base layer is significantly larger than its thermal equilibrium value, i.e. n_i^2/N_A , where N_A is the base doping. Therefore n can be approximately equal to Δn , which denotes the excess electron concentration compared to its thermal equilibrium concentration. The majority carrier concentration, in contrast, does not significantly change from the thermal value. Therefore, the two approximations $n \approx \Delta n \ll N_A$ and $p \approx N_A$ when substituted in (5.10), (5.11) and (5.12) give:

- **Radiative Recombination :** $R_{Rad} = \Delta n(B.N_A) = \frac{\Delta n}{\tau_{Rad}}$ (5.13)

- **SRH Recombination :** $R_{SRH} = \frac{pn}{\tau_{SRH}(n+p)} = \frac{p\Delta n}{\tau_{SRH}(\Delta n+p)} = \frac{\Delta n}{\tau_{SRH}}$ (5.14)

- **Auger Recombination :** $R_A = C(n+p)(np - n_i^2) = \Delta n(C.N_A^2) = \frac{\Delta n}{\tau_A}$ (5.15)

Thus the total recombination effect can be summarized as;

$$R_n = R_{Rad} + R_{SRH} + R_A = \frac{\Delta n}{\tau_n} \quad (5.16)$$

$$\frac{1}{\tau_n} = \frac{1}{\tau_{Rad}} + \frac{1}{\tau_{SRH}} + \frac{1}{\tau_A} \quad (5.17)$$

where τ_{Rad} , τ_{SRH} , τ_A and τ_n are radiative recombination lifetime, Auger lifetime, SRH lifetime and the total effective minority electron recombination lifetime respectively.

5.1.5 Steady State Continuity Equations

After incorporating the effect of photogeneration, recombination and taking into account the basic assumptions described earlier the continuity equation under optical absorption can then be written as:

$$\text{For base region: } D_n \frac{d^2 n_p}{dx^2} - \frac{\Delta n}{\tau_n} + \phi_b \alpha_b \exp(-\alpha_b x) = 0 \quad (5.18)$$

$$\text{For sub-collector region: } D_p \frac{d^2 p_n}{dx^2} - \frac{\Delta p}{\tau_p} + \phi_c \alpha_c \exp(-\alpha_c x) = 0 \quad (5.19)$$

where D_n (or D_p) and τ_n (or τ_p) are the diffusion coefficient and lifetime for minority carrier electrons (or holes), respectively, in the p^+ -GaAs base (or n -GaAs sub-collector). n_p (or p_n) and n_{po} (or p_{no}) are the total and equilibrium electron (or hole) density contributions, respectively, in the base (or sub-collector) region. α_b and α_c are the optical absorption coefficients for the base and sub-collector layers respectively. ϕ_b and ϕ_c are the values of incident flux density at the emitter-base ($x = 0$) and collector-subcollector ($x = w_b + w_{dep}$) junctions respectively.

The steady state continuity equation governing the distribution of minority carrier electrons (low-injection state) in the base region is considered here for further analysis. The solution for the sub-collector region will follow a similar pattern and can be derived accordingly. Now, (5.18) can be written as:

$$\frac{d^2 n_p}{dx^2} - \frac{(n_p - n_{po})}{L_n^2} + \frac{\phi_b \alpha_b \exp(-\alpha_b x)}{D_n} = 0 \quad (5.20)$$

where $L_n = \sqrt{D_n \tau_n}$. Rearranging (5.20) gives,

$$\frac{d^2 n_p}{dx^2} - \frac{n_p}{L_n^2} = -\frac{\phi_b \alpha_b \exp(-\alpha_b x)}{D_n} - \frac{n_{po}}{L_n^2} \quad (5.21)$$

The general solution of this equation will be a combination of the complementary function and the particular integral format [32].

5.1.5.1 Complementary Function

In order to ascertain the complementary function of (5.21), the RHS is taken as zero [32]:

$$\frac{d^2 n_p}{dx^2} - \frac{n_p}{L_n^2} = 0 \quad (5.22)$$

This gives,

$$n_p[cf] = A \exp\left(-\frac{x}{L_n}\right) + B \exp\left(\frac{x}{L_n}\right) \quad (5.23)$$

5.1.5.2 Particular Integral

The RHS of (5.21) has a form of $C \exp(-\alpha x) + D$. This gives

$$n_p[pi] = C \exp(-\alpha x) + D \quad (5.24)$$

$$\frac{dn_p}{dx} = -C \alpha \exp(-\alpha x) \quad (5.25)$$

$$\frac{d^2 n_p}{dx^2} = C \alpha^2 \exp(-\alpha x) \quad (5.26)$$

Inserting (5.24)-(5.26) in (5.21),

$$C \alpha^2 \exp(-\alpha x) - \frac{C \exp(-\alpha x) + D}{L_n^2} = -\frac{\phi_b \alpha_b \exp(-\alpha_b x)}{D_n} - \frac{n_{po}}{L_n^2} \quad (5.27)$$

By comparing similar terms,

$$\exp(-\alpha x) \left[C \alpha^2 - \frac{C}{L_n^2} \right] = -\frac{\phi_b \alpha_b}{D_n} \exp(-\alpha_b x) \text{ and } -\frac{D}{L_n^2} = -\frac{n_{po}}{L_n^2} \quad (5.28)$$

$$\rightarrow D = n_{po} \quad (5.29a)$$

$$\rightarrow C = -\frac{\phi_b \alpha_b L_n^2}{(L_n^2 \alpha_b^2 - 1) D_n} = -\frac{\phi_b \alpha_b \tau_n}{L_n^2 \alpha_b^2 - 1} \quad (5.29b)$$

Hence the general solution of minority electrons in the base region is the sum of the complementary function and the particular integral which is given as:

$$n_p(x) = \left[\begin{array}{l} n_p[cf] = A \exp\left(-\frac{x}{L_n}\right) + B \exp\left(\frac{x}{L_n}\right) \\ + \\ n_p[pi] = C \exp(-\alpha x) + D \end{array} \right] \quad (5.30)$$

By incorporating the values of C and D from (5.29) into (5.30), the general solution can be written as:

$$n_p(x) = A \exp\left(-\frac{x}{L_n}\right) + B \exp\left(\frac{x}{L_n}\right) - \frac{\phi_b \alpha_b L_n^2}{(L_n^2 \alpha_b^2 - 1) D_n} \exp(-\alpha_b x) + n_{po} \quad (5.31)$$

5.1.5.3 Accurate Boundary Conditions

In (5.31) there are still two unknowns, A and B and therefore further investigation is required to ascertain their values. In order to achieve this, the boundary conditions for the base layer will be used which are:

$$n_p(x=0) = n_p(0) = \frac{\phi_o(1-R_f)}{z(\alpha)s_n} = \frac{\phi_b}{z(\alpha)s_n} \quad (5.32a)$$

$$\begin{aligned} n_p(x=w_b) = n_p(w_b) &= \frac{\phi_b}{z(\alpha)s_n} \exp(-\alpha_b x_b) + n_{po} \\ &= n_p(0) \exp(-\alpha_b x_b) + n_{po} \end{aligned} \quad (5.32b)$$

where R_f is the Fresnel reflection coefficient and s_n is the surface recombination velocity of electrons in p⁺-GaAs base. The surface recombination will be higher at

lower wavelengths as more carriers are generated near the surface. This phenomenon is modelled by a wavelength dependent surface recombination parameter $z(\alpha)$. The excess minority carriers at the E-B junction is dependent on the input flux as no electrical contact is provided at the base terminal. Unity generation is assumed for input flux which is limited by surface recombination of the photocarriers. Optical flux is exponentially absorbed in the base region and the excess minority electron contribution at $x = w_b$ can be modelled by (5.32b) which also involves the equilibrium electron contribution. From (5.31), and (5.32a),

$$\begin{aligned} n_p(0) &= A + B - C + n_{po} \\ \rightarrow \quad A + B &= n_p(0) + C - n_{po} \end{aligned} \quad (5.33)$$

From (5.31) and (5.32b):

$$\begin{aligned} n_p(w_b) &= A \exp\left(-\frac{w_b}{L_n}\right) + B \exp\left(\frac{w_b}{L_n}\right) - C \exp(-\alpha w_b) + n_{po} \\ n_p(0) \exp(-\alpha_b x_b) + n_{po} &= A \exp\left(-\frac{w_b}{L_n}\right) + B \exp\left(\frac{w_b}{L_n}\right) - C \exp(-\alpha_b w_b) + n_{po} \\ \rightarrow \quad A \exp\left(-\frac{w_b}{L_n}\right) + B \exp\left(\frac{w_b}{L_n}\right) &= C \exp(-\alpha_b w_b) + n_p(0) \exp(-\alpha_b x_b) \end{aligned} \quad (5.34)$$

In order to find the values for A and B , (5.33) and (5.34) can be solved using matrices. Now (5.33) and (5.34) can be written in terms of matrices as:

$$\begin{pmatrix} \exp\left(-\frac{w_b}{L_n}\right) & \exp\left(\frac{w_b}{L_n}\right) \\ 1 & 1 \end{pmatrix} \begin{bmatrix} A \\ B \end{bmatrix} = \begin{bmatrix} C \exp(-\alpha_b w_b) + n_p(0) \exp(-\alpha_b w_b) \\ C + n_p(0) - n_{po} \end{bmatrix} \quad (5.35)$$

$$\begin{bmatrix} A \\ B \end{bmatrix} = \begin{pmatrix} \exp\left(-\frac{w_b}{L_n}\right) & \exp\left(\frac{w_b}{L_n}\right) \\ 1 & 1 \end{pmatrix}^{-1} \begin{bmatrix} C \exp(-\alpha_b w_b) + n_p(0) \exp(-\alpha_b w_b) \\ C + n_p(0) - n_{po} \end{bmatrix} \quad (5.36)$$

$$\begin{bmatrix} A \\ B \end{bmatrix} = \frac{1}{-2 \sinh \frac{w_b}{L_n}} \begin{pmatrix} 1 & -\exp\left(\frac{w_b}{L_n}\right) \\ -1 & \exp\left(-\frac{w_b}{L_n}\right) \end{pmatrix} \begin{bmatrix} C \exp(-\alpha_b w_b) + n_p(0) \exp(-\alpha_b w_b) \\ C + n_p(0) - n_{po} \end{bmatrix} \quad (5.37)$$

where,

$$\begin{pmatrix} \exp(-\frac{w_b}{L_n}) & \exp(\frac{w_b}{L_n}) \\ 1 & 1 \end{pmatrix}^{-1} = \frac{1}{-2 \sinh \frac{w_b}{L_n}} \begin{pmatrix} 1 & -\exp(\frac{w_b}{L_n}) \\ -1 & \exp(-\frac{w_b}{L_n}) \end{pmatrix}$$

Identities, $\exp(nx) = \cosh nx + \sinh nx$ and $\exp(-nx) = \cosh nx - \sinh nx$ have been used to simplify the matrices. Now multiplying the matrices in (5.37) gives (5.38):

$$\begin{bmatrix} A \\ B \end{bmatrix} = \frac{1}{-2 \sinh \frac{w_b}{L_n}} \begin{bmatrix} C \exp(-\alpha_b w_b) + n_p(0) \exp(-\alpha_b w_b) - C \exp(\frac{w_b}{L_n}) \dots \\ -n_p(0) \exp(\frac{w_b}{L_n}) + n_{po} \exp(\frac{w_b}{L_n}) \\ -C \exp(-\alpha_b w_b) - n_p(0) \exp(-\alpha_b w_b) + C \exp(-\frac{w_b}{L_n}) \dots \\ +n_p(0) \exp(-\frac{w_b}{L_n}) - n_{po} \exp(-\frac{w_b}{L_n}) \end{bmatrix} \quad (5.38)$$

After multiplying A with $\exp(-x/L_n)$ and B with $\exp(x/L_n)$ and adding them together so that the sum takes form of (5.31), one can obtain:

$$\begin{bmatrix} A \exp(-\frac{x}{L_n}) \\ B \exp(\frac{x}{L_n}) \end{bmatrix} = \frac{1}{-2 \sinh \frac{w_b}{L_n}} \left\{ \begin{array}{l} C \left[\exp(-\alpha_b w_b - \frac{x}{L_n}) - \exp(\frac{w_b - x}{L_n}) \right] + \dots \\ n_p(0) \left[\exp(-\alpha_b w_b - \frac{x}{L_n}) - \exp(\frac{w_b - x}{L_n}) \right] + n_{po} \exp(\frac{w_b - x}{L_n}) \\ C \left[\exp(\frac{x - w_b}{L_n}) - \exp(-\alpha_b w_b + \frac{x}{L_n}) \right] + \dots \\ n_p(0) \left[\exp(\frac{x - w_b}{L_n}) - \exp(-\alpha_b w_b + \frac{x}{L_n}) \right] - n_{po} \exp(\frac{x - w_b}{L_n}) \end{array} \right\} \quad (5.39)$$

$$A \exp(-\frac{x}{L_n}) + B \exp(\frac{x}{L_n}) = \frac{1}{-2 \sinh \frac{w_b}{L_n}} \left\{ \begin{array}{l} C [\exp(\frac{x - w_b}{L_n}) - \exp(-\frac{x - w_b}{L_n})] - \dots \\ C \exp(-\alpha_b w_b) [\exp(\frac{x}{L_n}) - \exp(-\frac{x}{L_n})] + \dots \\ n_p(0) [\exp(\frac{x - w_b}{L_n}) - \exp(-\frac{x - w_b}{L_n})] - \dots \\ n_p(0) \exp(-\alpha_b w_b) [\exp(\frac{x}{L_n}) - \exp(-\frac{x}{L_n})] - \dots \\ n_{po} [\exp(\frac{x - w_b}{L_n}) - \exp(-\frac{x - w_b}{L_n})] \end{array} \right\} \quad (5.40)$$

$$A \exp\left(-\frac{x}{L_n}\right) + B \exp\left(\frac{x}{L_n}\right) = \frac{1}{-\sinh \frac{w_b}{L_n}} \left\{ \begin{aligned} & C \sinh\left(\frac{x-w_b}{L_n}\right) - C \sinh\left(\frac{x}{L_n}\right) \exp(-\alpha_b w_b) + n_p(0) \sinh\left(\frac{x-w_b}{L_n}\right) \\ & - n_p(0) \sinh\left(\frac{x}{L_n}\right) \exp(-\alpha_b w_b) - n_{po} \sinh\left(\frac{x-w_b}{L_n}\right) \end{aligned} \right\}$$

$$A \exp\left(-\frac{x}{L_n}\right) + B \exp\left(\frac{x}{L_n}\right) = \frac{1}{\sinh \frac{w_b}{L_n}} \left\{ \begin{aligned} & \sinh\left(\frac{x}{L_n}\right) \exp(-\alpha_b w_b) [C + n_p(0)] \\ & + \\ & \sinh\left(\frac{x-w_b}{L_n}\right) [n_{po} - C - n_p(0)] \end{aligned} \right\} \quad (5.41)$$

Now (5.31) can be written in the form:

$$n_p = A \exp\left(-\frac{x}{L_n}\right) + B \exp\left(\frac{x}{L_n}\right) - C \exp(-\alpha_b x) + n_{po} \quad (5.42)$$

and differentiating n_p w.r.t x gives,

$$\frac{dn_p}{dx} = \frac{1}{\sinh \frac{w_b}{L_n}} \left\{ \begin{aligned} & \frac{1}{L_n} \cosh\left(\frac{x}{L_n}\right) \exp(-\alpha_b w_b) [C + n_p(0)] \\ & + \\ & \frac{1}{L_n} \cosh\left(\frac{x-w_b}{L_n}\right) [n_{po} - C - n_p(0)] \end{aligned} \right\} + C \alpha_b \exp(-\alpha_b x) \quad (5.43)$$

$$\left. \frac{dn_p}{dx} \right|_{x=w_b} = \frac{1}{\sinh \frac{w_b}{L_n}} \left\{ \begin{aligned} & \frac{1}{L_n} \cosh\left(\frac{w_b}{L_n}\right) \exp(-\alpha_b w_b) [C + n_p(0)] \\ & + \\ & \frac{1}{L_n} [n_{po} - C - n_p(0)] \end{aligned} \right\} + C \alpha_b \exp(-\alpha_b w_b) \quad (5.44)$$

5.1.5.4 Fick's Law

For a given wavelength radiation the total electron current at the base-collector junction, $I_n(\lambda)$, can be evaluated using Fick's law [27]:

$$I_n(\lambda) = -q D_n A_{EB} \left. \frac{dn_p}{dx} \right|_{x=w_b} \quad (5.45)$$

Where A_{EB} is the E-B junction area. The current due to excess minority electrons in the base region has been formulated from (5.44) and (5.55), providing the following:

$$I_n(\lambda) = -\frac{qD_n A_{EB}}{L_n \sinh \frac{w_b}{L_n}} \left\{ \begin{array}{l} C[\alpha_b L_n \sinh(\frac{w_b}{L_n}) \exp(-\alpha_b w_b) + \cosh(\frac{w_b}{L_n}) \exp(-\alpha_b w_b) - 1] + \\ n_p(x=0)[\cosh(\frac{w_b}{L_n}) \exp(-\alpha_b w_b) - 1] + n_{po} \end{array} \right\} \quad (5.46)$$

The collector current due to excess minority holes in the sub-collector can similarly be modelled by following the procedure explained above and is written as:

$$I_p(\lambda) = \frac{qD_p A_C}{L_p \sinh(\frac{w_c}{L_p})} \left\{ \begin{array}{l} -C'[1 + \cosh(\frac{w_c}{L_p}) \exp(-\alpha_c w_c) + \sinh(\frac{w_c}{L_p}) \alpha_c L_p \exp(-\alpha_c w_c) \alpha_c L_p] + \\ p_n(x=w_b + w_{dep})[1 - \cosh(\frac{w_c}{L_p}) \exp(-\alpha_c w_c)] - p_{no} \end{array} \right\} \quad (5.47)$$

where

$$C' = \frac{\phi_c \alpha_c \tau_p}{\alpha_c^2 L_p^2 - 1}$$

5.1.6 Depleted Collector Absorption

The optical flux absorption in the B-C depletion region would give rise to a photogenerated current (I_{ph}) which can be modelled by (5.48). It is assumed that no generation, other than photo-generation through input flux, occurs in the depleted collector. The recombination is considered negligible due to a strong electric field created by the depleted ions in this space charge region:

$$I_{ph}(\lambda) = -qA_C \int_0^{w_{dep}} \Phi_{dep} \alpha_{dep} \exp(-\alpha_{dep} x) dx \quad (5.48)$$

$$I_{ph}(\lambda) = -qA_C \Phi_{dep} [1 - \exp(-\alpha_{dep} w_{dep})] \quad (5.49)$$

where Φ_{dep} is the input flux density at the edge of B-C depletion region, α_{dep} is the absorption coefficient in the depletion region and A_C is the area of the depleted collector.

5.1.7 Responsivity

The flux-dependent collector current (I_c) is the sum of individual current contributions in the base (I_n), depleted collector (I_{ph}) and sub-collector (I_p) regions. The responsivity (ratio of photogenerated current to the input optical power) is given by (5.51) [5]. This is a general expression for responsivity and can be used for any device materials provided one knows the details of device parameters.

$$I_c(\lambda) = I_n(\lambda) + I_p(\lambda) + I_{ph}(\lambda) \quad (5.50)$$

$$R(\lambda) = \frac{\lambda I_c(\lambda)}{hc\Phi_o(1 - R_f)} \quad (5.51)$$

5.2 Modelled and Measured Results

5.2.1 AlGaAs/GaAs HPTs

The theoretical responsivity for HPTs can be calculated by using (5.51) and inserting the necessary device and material parameters. A summary of the parameters used is given in Table 5-1.

Table 5-1: Material parameters used for AlGaAs/GaAs HPT simulation.

Parameter	Value (respectively)	Reference
D_n, D_p	50, 4 [cm ² s ⁻¹]	[33]
τ_n, τ_p	$1 \times 10^{-9}, 1.2 \times 10^{-9}$ [s]	[27, 34]
$L_n = (\tau_n D_n)^{1/2}, L_p = (\tau_p D_p)^{1/2}$	$2.2 \times 10^{-4}, 0.7 \times 10^{-4}$ [cm]	[25]
s_n, s_p	$3 \times 10^4, \sim 10^6$ [cm s ⁻¹]	[35, 36]
$n_{po} = n_i^2/N_A, n_{po} = n_i^2/N_D$	$2.2 \times 10^{-7}, 8.8 \times 10^{-7}$ [cm ⁻³]	[36]
$\alpha_b(635\text{nm}), \alpha_b(850\text{nm})$	$3.4 \times 10^4, 0.6 \times 10^4$ [cm ⁻¹]	[33, 37]
$\alpha_{dep}(635\text{nm}), \alpha_{dep}(850\text{nm})$	$3.4 \times 10^4, 0.9 \times 10^4$ [cm ⁻¹]	[33, 37]
$\alpha_c(635\text{nm}), \alpha_c(850\text{nm})$	$3.4 \times 10^4, 0.1 \times 10^4$ [cm ⁻¹]	[33, 37]
$\Phi(b)$ at 635nm, $\Phi(b)$ at 850nm	$2.2 \times 10^{14}, 2.9 \times 10^{14}$ [s ⁻¹]	Figure 4-7
$\Phi(dep)$ 635nm, $\Phi(dep)$ at 850nm	$1.6 \times 10^{14}, 2.8 \times 10^{14}$ [s ⁻¹]	Figure 4-7
$\Phi(c)$ 635nm, $\Phi(c)$ at 850nm	$0.3 \times 10^{14}, 1.8 \times 10^{14}$ [s ⁻¹]	Figure 4-7

It should be noted that the surface recombination reduces the responsivity and requires careful modelling. The recombination due to misfit dislocations at the

emitter-base heterostructure interface can be minimized by grading the heterojunction interface as used in this work. Despite the widely different surface preparation and measurement techniques, the surface recombination data for GaAs follows the same general trend of proportionality to bulk doping [35]. However, as the depth of incident irradiation is inversely proportional to the absorption coefficient, all high energy photons are absorbed near the surface, causing many of the generated carriers to be lost due to surface recombination. These photocarriers, close to the surface, are lost due to the high recombination velocity. Therefore, an additional surface recombination parameter $z(\alpha)$ is required to model this effect. $z(\alpha)$ is a simulation parameter and the value of $z(\alpha)$ is higher for lower wavelengths as more photocarriers are generated near the surface. Remarkably, the variation of surface recombination parameter follows a near exponential decay with increasing wavelengths which is consistent with power absorption in semiconductors. The variation of $z(\alpha)$ with various incident wavelengths has been modelled in Figure 5-2. Higher values of $z(\alpha)$ at lower wavelengths imply that a considerable amount of photogenerated carriers in the surface vicinity will be lost by recombination. Thus, these recombined carriers do not contribute to the photocurrent.

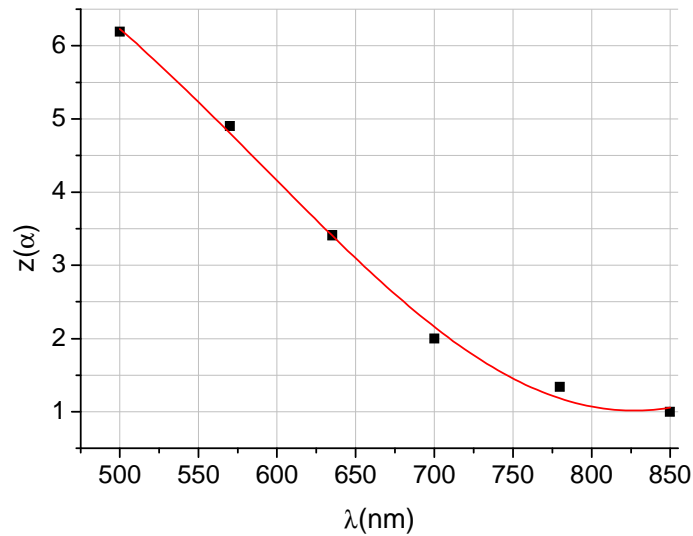


Figure 5-2. Simulated variation of surface recombination parameter $z(\alpha)$ with incident wavelengths for the $Al_{0.3}Ga_{0.7}As/GaAs$ HPT.

The modelled spectral response, using (5.51), along with the measured results at 635 nm, 780 nm, 808 nm, and 850 nm are shown in Figure 5-3. Matlab has been used

to obtain the predicted response using (5.51). The responsivity maximises at around 760 nm and tends to go down with increasing wavelengths due to a drop in the absorption coefficient.

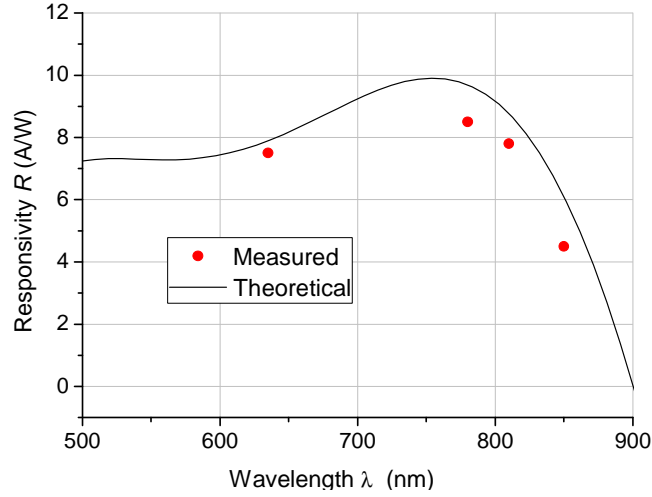


Figure 5-3. Measured and calculated spectral response of the $Al_{0.3}Ga_{0.7}As/GaAs$ HPT.

5.2.2 $InP/InGaAs$ HPTs

The generic model using flux-dependent continuity equations has been described in section 5.1, therefore the SR modelling of any other material system required detailed device structure and material parameters. For the $InP/In_{0.47}Ga_{0.53}As$ material system, the material parameters are given in Table 5-2.

Table 5.2: Material parameters used for $InP/InGaAs$ HPTs simulation.

Parameter	Value (respectively)	Reference
D_n, D_p	36.25, 2 $[cm^2s^{-1}]$	[38]
τ_n, τ_p	$4 \times 10^{-11}, 4 \times 10^{-11}$ [s]	[39]
$L_n = (\tau_n D_n)^{1/2}, L_p = (\tau_p D_p)^{1/2}$	$0.4 \times 10^{-4}, 0.09 \times 10^{-4}$ [cm]	[25]
s_n, s_p	$3 \times 10^4, \sim 10^6$ $[cm s^{-1}]$	[40]
$n_{po} = n_i^2/N_A, n_{po} = n_i^2/N_D$	$2 \times 10^4, 2 \times 10^4$ $[cm^{-3}]$	[26]
$\alpha_b(1310nm), \alpha_b(1550nm)$	$1.55 \times 10^4, 0.85 \times 10^4$ $[cm^{-1}]$	[41]
$\alpha_{dep}(1310nm), \alpha_{dep}(1550nm)$	$1.16 \times 10^4, 0.68 \times 10^4$ $[cm^{-1}]$	[41]
$\alpha_c(1310nm), \alpha_c(1550nm)$	$1.16 \times 10^4, 0.68 \times 10^4$ $[cm^{-1}]$	[41]
$\Phi(b)$ at 1310nm, $\Phi(b)$ at 1550nm	$4.5 \times 10^{14}, 5.3 \times 10^{14}$ $[s^{-1}]$	Figure 4-10
$\Phi(dep)$ 1310nm, $\Phi(dep)$ at 1550nm	$3.9 \times 10^{14}, 4.95 \times 10^{14}$ $[s^{-1}]$	Figure 4-10
$\Phi(c)$ at 1310, $\Phi(c)$ at 1550nm	$2.45 \times 10^{14}, 3.75 \times 10^{14}$ $[s^{-1}]$	Figure 4-10

The surface recombination parameter shows a similar trend to that for the GaAs device, however the value is slightly low at lower wavelengths as shown in Figure 5-4. This is attributed to the lack of intrinsic surface recombination in the lattice matched emitter and the base surface which in turn results in a lower recombination parameter.

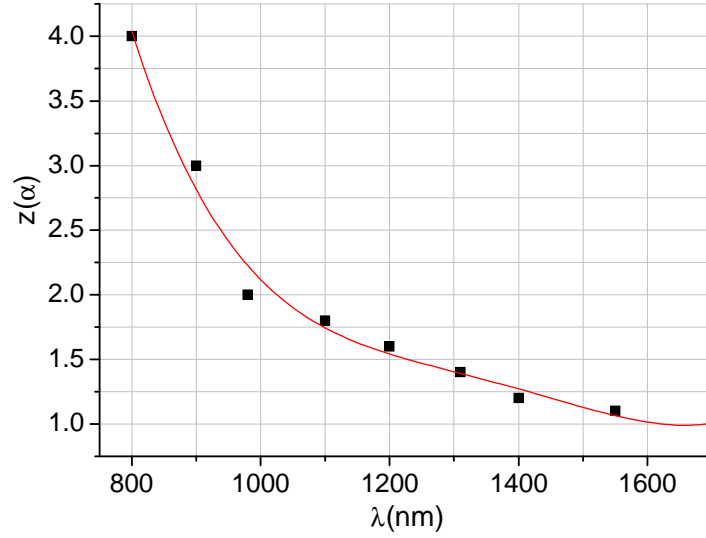


Figure5-4. Simulated variation of surface recombination parameter $z(\alpha)$ with incident wavelengths for the $\text{InP}/\text{In}_{0.47}\text{Ga}_{0.53}\text{As}$ HPT.

The InP-devices under investigation are lattice matched and, therefore, the intrinsic surface recombination will be lower compared to GaAs-based devices resulting in a slightly lower value of $z(\alpha)$. Noticeably, the variation of surface recombination parameter follows an exponential decay with higher wavelengths which is consistent with power absorption in semiconductors. This implies that the photocarrier generation mostly occurs at the surface for high energy photons and as the photon energy reduces with increasing wavelength, lower numbers of carriers are generated at the surface, resulting in lower values of surface recombination. The spectral response for the $\text{InP}/\text{In}_{0.47}\text{Ga}_{0.53}\text{As}$ devices for long wavelength detection is given in Figure 5-5.

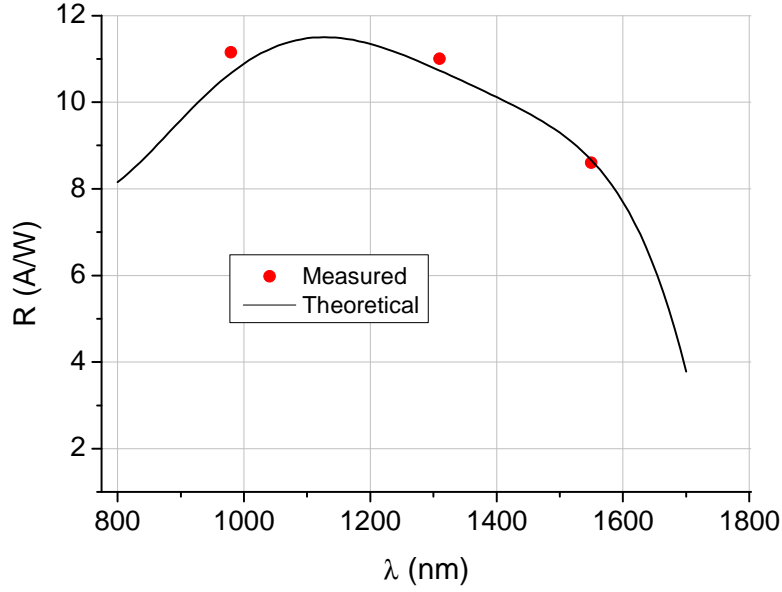


Figure 5-5. Measured and calculated spectral response of the InP/In_{0.47}Ga_{0.53}As HPT.

5.2.3 Base Width Variation Consideration

The analytical model described here highlights directly the critical device and material properties affecting the spectral response of heterojunction phototransistors and can be utilised to assess the performance of the device with variation of physical features such as base width. Base width variation can have a contradictory effect on the figures of merit for HPTs. Improved cut-off frequency due to reduced absorbing layer width in HPTs can be accompanied with lower collection efficiency which results in lower responsivity, particularly for surface-illuminated DHPTs. This issue will be discussed in detail in chapter 6. However, it is important to highlight the variation of responsivity with different base widths at various incident wavelengths.

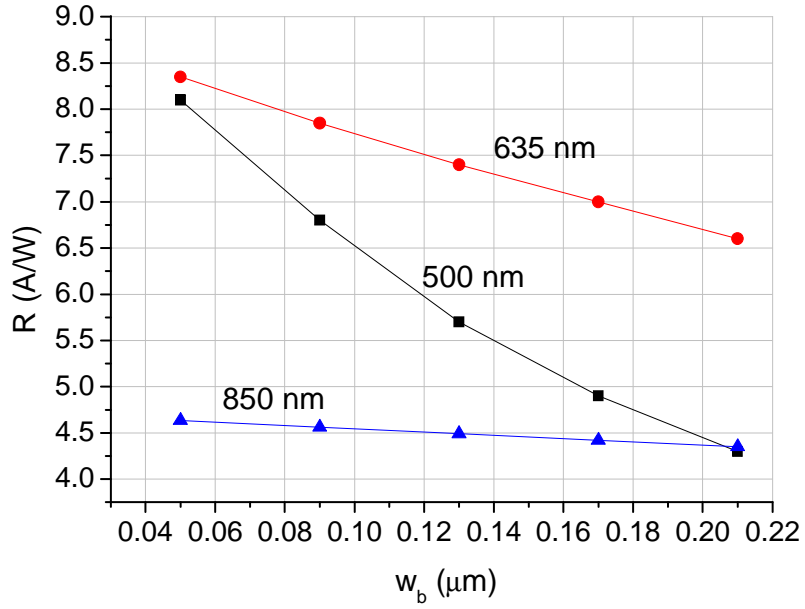


Figure 5-6. Simulated variation of Responsivity with base width for the $\text{Al}_{0.3}\text{Ga}_{0.7}\text{As}/\text{GaAs}$ HPT at various incident wavelengths.

It can be observed from Figure 5-6 that the responsivity shows a decreasing trend with the increase of base width. This data has been obtained by varying the base width in equations (5.46), (5.47) and (5.49) and updating the values of the corresponding currents in (5.51) for three different wavelengths. It is well known that the intrinsic gain of a transistor decreases with the increase in the base width due to increased recombination in the bulk region. However, different rates of decrease in the responsivity have been observed for three wavelengths in question, as seen in Figure 5-6. An increase in the base width is associated with an increase in bulk recombination as well as surface recombination because more carriers are being generated near the surface for high energy photons having smaller wavelengths. For the two wavelengths 635 nm and 500 nm, relatively more photocarriers are generated near the surface for 500 nm as compared to 635 nm and as the surface recombination parameter is larger for 500 nm, this results in a sharp drop in the responsivity at this wavelength. This trend should also be seen at 850 nm, however the increase in recombination is compensated, largely, by the increased number of photocarriers in the base region. Referring to the optical flux absorption profile (Figure 4-5), the collection efficiency will increase largely with increased base width and the magnitude of decrease in responsivity is low. The collection efficiency at 635 nm

and 500 nm is unity (as photo-absorption occurs in the active region only) and thus does not affect the responsivity with variation in the base layer width.

The variation in the responsivity for InP/In_{0.47}Ga_{0.53}As HPTs is shown in Figure 5-7 using the same mathematical analysis but with appropriate device physical parameters. The responsivity decreases with the increase in layer width, however, the rate of decrease varies for the three wavelengths under consideration. At 1550 nm, the rate of decrease is slightly higher which can be attributed to the low absorption coefficient in the base layer (0.85×10^4 /cm). The recombination increases with the increase in the base width but on the other hand the generation of photocarriers is limited by the low absorption coefficient resulting in a larger decrease in responsivity seen at this wavelength. Thus careful optimisation is required to design HPTs for wavelengths-specific applications.

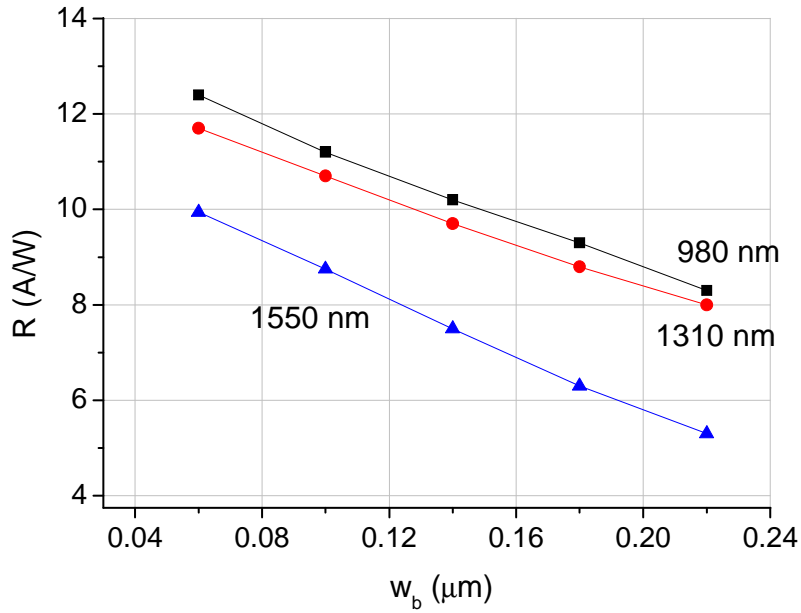


Figure 5-7. Simulation variation of responsivity with base width for the InP/In_{0.47}Ga_{0.53}As HPT at various incident wavelengths.

References

- [1] S. W. Choi, S. Furue, N. Hayama, K. Nishida, and M. Ogura, "Gain-enhanced InGaAs-InP iheterojunction phototransistor with Zn-doped mesa sidewall," *IEEE Photonics Technology Letters*, vol. 21, pp. 1187-1189, 2009.
- [2] Y. W. Byun, M. S. Park, Y. H. Park, Y. C. Cho, and J. H. Jang, "InGaP/GaAs heterojunction phototransistors for ultra-low optical power detection," presented at IEEE International Conference on Indium Phosphide and Related Materials, IPRM 2009, May 10, 2009 - May 14, 2009, Newport Beach, CA, United states, 2009.
- [3] H. Kamitsuna, Matsuoka Y., Yamahata S., Shigekawa, N., "Ultrahigh-speed InP/InGaAs DHPTs for OEMMICs," *IEEE Transactions on Microwave Theory and Techniques*, vol. 49, pp. 1921-1925, 2001.
- [4] R. F. Sridhara, S.M. Roenker, K.P. Pan, N. Elliott, J., "Performance enhancement of GaInP/GaAs heterojunction bipolar phototransistors using dc base bias," *Journal of Lightwave Technology*, vol. 16, pp. 1101-6, 1998.
- [5] H. A. Khan and A. A. Rezazadeh, "Analytical modeling of the spectral response of heterojunction phototransistors," *IEEE Electron Device Letters*, vol. 30, pp. 1158-1160, 2009.
- [6] D. Ritter, B. Sheinman, V. Sidorov, S. Cohen, A. Gavrilov, Y. Vered, G. Zohar, and J. Lasri, "Optimization of InP/GaInAs heterojunction bipolar transistors and phototransistors," presented at Proceedings of International Topical Meeting on Microwave Photonics (MWP2002), 5-8 Nov. 2002, Tokyo, Japan, 2002.
- [7] A. H. Leven, V. Kopf, R. Baeyens, Y. Chen, Y.-K., "InP-based double-heterostructure phototransistors with 135 GHz optical-gain cutoff frequency," *Electronics Letters*, vol. 40, pp. 833-834, 2004.
- [8] V. M. Samuel Dupont, Emmanuel Fendler, Philippe Jorge, Sophie Maricot, Jean-Pierre Vilcot, Joseph Harari, Didier Decoster, "Status on long-wavelength InP waveguide heterojunction phototransistors," presented at Diamond Congress (Invited paper), Budapest, Hungry, 2004.
- [9] A. Bilenca, J. Lasri, B. Sheinman, G. Eisenstein, and D. Ritter, "Millimeter-Wave Generation and Digital Modulation in an InGaAs-InP Heterojunction Phototransistor:Model and Experimental Characterization of Dynamics and Noise," *Journal of Lightwave Technology*, vol. 19, pp. 1340, 2001.

- [10] R. Decorby, R. Macdonald, M. Beaudoin, T. Pinnington, T. Tiedje, and F. Gouin, "Elimination of low frequency gain in InAlAs/InGaAs metal-semiconductor-metal photodetectors by silicon nitride passivation," *Journal of Electronic Materials*, vol. 26, pp. L25-L28, 1997.
- [11] J. H. Kim, H. T. Griem, R. A. Friedman, E. Y. Chan, and S. Ray, "High-performance back-illuminated InGaAs/InAlAs MSM photodetector with a record responsivity of 0.96 A/W," *Photonics Technology Letters, IEEE*, vol. 4, pp. 1241-1244, 1992.
- [12] K. H. Lee, "Al_{0.25}Ga_{0.75}N/GaN Schottky Barrier Photodetectors with an Al_{0.3}Ga_{0.7}N Intermediate Layer," *Journal of The Electrochemical Society*, vol. 156, pp. J199, 2009.
- [13] C.-S. Choi, "Phototransistors based on InP HEMTs and HBTs, and their applications to fiber-optic/millimeter-wave data transmission systems," PhD Thesis, Yonsei University, 2005.
- [14] J. Thuret, C. Gonzalez, J. L. Benchimol, M. Riet, and P. Berdager, "High-speed InP/InGaAs heterojunction phototransistor for millimetre-wave fibre radio communications," *Proceedings of the 1999 11th International Conference on Indium Phosphide and Related Materials (IPRM), May 16, 1999 - May 20, 1999*, pp. 389-392, 1999.
- [15] H. Kamitsuna, Y. Matsuoka, S. Yamahata, and K. Kurishima, "Monolithically integrated photoreceiver realized by InP/InGaAs double-heterostructure bipolar transistor technologies for optical/microwave interaction systems," presented at Proceedings of the 17th Annual IEEE Gallium Arsenide Integrated Circuit Symposium, Oct 29-Nov 1 1995, San Diego, CA, USA, 1995.
- [16] A. M. Bouhdada, R. Vigue, F. Faurie, J.-P., "Modeling of the spectral response of PIN photodetectors impact of exposed zone thickness, surface recombination velocity and trap concentration," *Microelectronics Reliability*, vol. 44, pp. 223-8, 2004.
- [17] M. B. Hanzaz, A. Monroy, E. Munoz, E. Gibart, P. Omnes, F., "Modeling of the spectral response of Al_xGa_{1-x}N p-n junction photodetectors," *European Physical Journal, Applied Physics*, vol. 11, pp. 29-34, 2000.

- [18] H. Zheng, K. Yong, T. Ying-Wen, L. Xue, and F. Jia-Xiong, "Study on the spectral response of the Schottky photodetector of GaN," *Chinese Physics*, vol. 15, pp. 1325-9, 2006.
- [19] J. A. R. Gonzalez-Cuevas, Tamer F. Abedin, M. Nurul Elsayed-Ali, Hani E., "Modeling of the temperature-dependent spectral response of $\text{In}_{1-x}\text{Ga}_x\text{Sb}$ infrared photodetectors," *Optical Engineering*, vol. 45, pp. 044001, 2006.
- [20] N. Chand, P. A. Houston, and P. N. Robson, "Gain of a Heterojunction Bipolar Phototransistor," *IEEE Transactions on Electron Devices*, vol. ED-32, pp. 622-627, 1985.
- [21] L. E. M. de Barros, Jr. Paolella, A. Frankel, M.Y. Romero, M.J. Herczfeld, P.R. Madjar, A., "Photoresponse of microwave transistors to high-frequency modulated lightwave carrier signal," *IEEE Transactions on Microwave Theory and Techniques*, vol. 45, pp. 1368-74, 1997.
- [22] S. A. Bashar and A. A. Rezazadeh, "Fabrication and spectral response analysis of AlGaAs/GaAs and InP/InGaAs HPTs with transparent ITO emitter contacts," *IEE Proceedings-Optoelectronics*, vol. 143, pp. 89-93, 1996.
- [23] S. A. Bashar, "Study of Indium Tin Oxide (ITO) for Novel Optoelectronic Devices," Ph.D thesis, King's College London, 1998.
- [24] H. A. Khan, A. A. Rezazadeh, and S. C. Subramaniam, "Spectral response modelling of heterojunction phototransistors for short wavelength transmission," presented at 2008 European Microwave Integrated Circuit Conference, EuMIC 2008, October 27, 2008 - October 31, 2008, Amsterdam, Netherlands, 2008.
- [25] S. M. Sze, *Physics of Semiconductor Devices*, 2nd ed. USA: John Wiley & Sons, 2001.
- [26] M. S. Tyagi, *Introduction to Semiconductor Materials and Devices*: John Wiley & Sons, 1991.
- [27] S. M. Sze, *Semiconductor Devices: Physics and Technology*: John Wiley & Sons, 1985.
- [28] C. Dharmasari, "Compact Semi-Physical Modelling for HBT Circuit Simulations," Ph.D thesis, The University of Manchester, 2006.
- [29] K. Brennan, *The Physics Of Semiconductors*: Cambridge university press, 1999.

- [30] W. Shockley and T. Reed, "Statistics of the recombination of holes and electrons," *Phys. Rev.* 87, pp. 835, 1952.
- [31] R. N. Hall, "Electron-hole recombination in Germanium," *Phys. Rev.* 87, pp. 387, 1952.
- [32] K. A. Stroud, *Engineering Mathematics*, 4th ed: Bath Press, 1995.
- [33] G. B. Lush, "Properties of GaAs," in *EMIS data review series*, 2nd ed: Inspec publications, 1990, pp. 513-528.
- [34] C. J. Hwang, "Doping dependence of hole lifetime in n-type GaAs," *Journal of Applied Physics*, vol. 42, pp. 4408-13, 1971.
- [35] D. E. Aspnes, "Recombination at semiconductor surfaces and interfaces," presented at Proceedings of the Second Trieste ICTP-IUPAP Semiconductor Symposium on Surfaces and Interfaces, Physics and Electronics, 30 Aug.-3 Sept. 1982, Netherlands.
- [36] G. A. Acket, W. Nijman, and H. t. Lam, "Electron Lifetime and diffusion constant in Germanium-doped Gallium Arsenide," *Journal of Applied Physics*, vol. 45, pp. 3033-3040, 1974.
- [37] H. C. J. Casey, D. D. Sell, and K. W. Wecht, "Concentration dependence of the absorption coefficient for n- and p-type GaAs between 1.3 and 1.6 eV.," *Journal of Applied Physics*, vol. 46, pp. 250-257, 1975.
- [38] H. Sheng, "Modelling, Fabrication and Characterisation of InP-HBTs for Future High-Speed, Low-Power Optical Telecommunications," Ph.D thesis, King's College London, 2000.
- [39] R. K. Ahrenkiel, R. Ellingson, S. Johnston, and M. Wanlass, "Recombination lifetime of In_{0.53}Ga_{0.47}As as a function of doping density," *Applied Physics Letters*, vol. 72, pp. 3470-3472, 1998.
- [40] I. Tonai, "InGaAs/InP type pin photodiodes." United States patent, 1991.
- [41] D. A. Humphreys, R. J. King, D. Jenkins, and A. J. Moseley, "Measurement of absorption coefficients of Ga_{0.47}In_{0.53}As over the wavelength range 1.0-1.7 μ m," *Electronics Letters*, vol. 21, pp. 1187-9, 1985.

Chapter 6

Photoresponse Modelling of DHPTs

Huge interest in high speed HPTs has been seen in the past decade for their use in ultra-fast photoreceivers [1-4]. Single-HPTs (sHPTs) have most commonly been employed in the front end of optical receivers as an alternative to pin photodiodes (for intrinsic gain) and avalanche photodiodes (for superior noise performance)[5-7]. However, the thick absorbing collector layer deteriorates the frequency performance of these phototransistors due to the generation of slow moving holes in the collector region for Npn design. Moreover, the low breakdown voltage due to narrow band gap collector (InGaAs/GaAs) makes it difficult to apply higher bias to the sHPTs for high speed applications [8].

Kamitsuana *et al.* [9] proposed a modified DHPT structure to mitigate these problems which was then used by Leven *et al.* [10] to develop DHPTs with cutoff a frequency in excess of 135 GHz for a surface-illuminated configuration. In such an orientation, HPTs have the same layer structure as HBTs which supports their monolithic integration in photoreceiver fabrication using the same epitaxial and processing steps, avoiding a regrowth process with its associated problems [11]. Edge-illuminated orientation, on the other hand, shows superior responsivity but the low coupling efficiency and relatively difficult fabrication process remains an issue for industrial manufacturing of photoreceivers.

The parameter evolution in the design of optical receivers can have contradictory effects on the different figures of merit for HPTs. For example, improved cut-off frequency due to a reduced absorbing layer width in HPTs can be accompanied by lower conversion/collection efficiency which results in low responsivity. In order to achieve efficient photoresponse and high speed operation of these devices, a detailed analysis of the device layer structure along with its modelling parameters is of paramount importance. The photoresponse for sHPTs has been discussed in the literature [12-14], however research on DHPTs has rather been limited. In this

chapter, the photoresponse of an $\text{In}_{0.49}\text{Ga}_{0.51}\text{P}/\text{GaAs}$ NpN DHBT is modelled and compared with the measured results. Good agreement has been seen for optical power at $10\text{ }\mu\text{W}$, which is then followed by analysis of intrinsic parameters with varying optical input.

6.1 Optical Absorption

The optical absorption in DHPTs differs to the absorption in sHPTs as there is an additional heterojunction between the base and collector regions. The optical flux, absorbed in the base region only, contributes towards the photoresponse while the signal absorbed in the collector and sub-collector regions does not contribute towards transistor action (gain). The photogenerated holes in the collector and sub-collector will not drift towards the base region due to the additional heterostructure (base-collector) in the DHBTs. The wide band gap emitter is considered transparent and the incident signal goes unattenuated through the emitter and the absorption starts from the base layer. A comparison between absorption in sHPTs and DHPTs is shown in Figure 6-1. The optical absorption in the base region requires investigation because the base width is relatively very small and subtle variations in the absorption phenomena can have a sizeable effect on the photoresponse. Unlike sHPTs, some flux is reflected in DHPTs from the interface of base and collector regions which adds to the useful flux absorbed in the base layer (Figure 6-1b).

For sHPTs, the flux absorbed in the active layers has already been given in Section 4-1. The flux absorbed in the base region of a DHPT after one reflection from $x = b$ (base-collector heterojunction) can be written as:

$$(\phi_{abs})_b = \phi_o (1 - \exp^{-\alpha_b x_b}) + \phi_o R_{f,b/c} \exp^{-\alpha_b x_b} (1 - \exp^{-\alpha_b x_b}) \quad (6.1)$$

$$(\phi_{abs})_b = \phi_o (1 - \exp^{-\alpha_b x_b}) (1 + R_{f,b/c} \exp^{-\alpha_b x_b}) \quad (6.2)$$

Another reflection from the emitter-base interface ($x = a$) will add to the flux absorbed which can be modeled by (6.3).

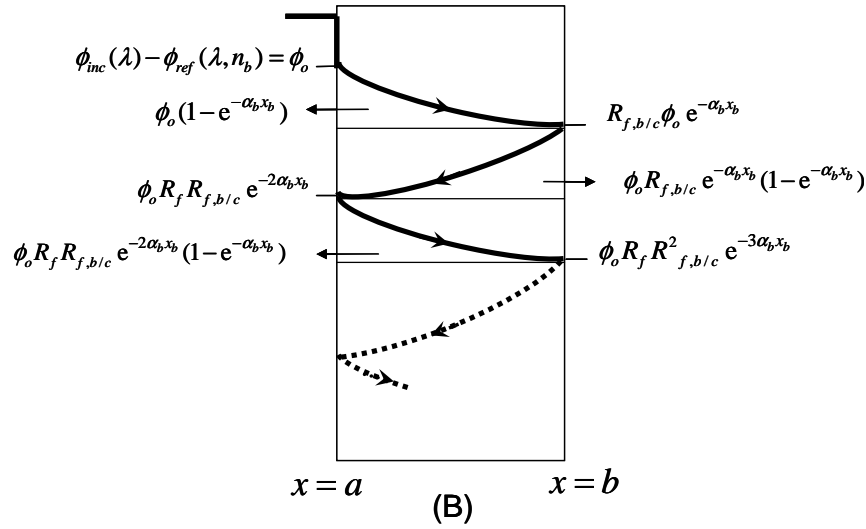
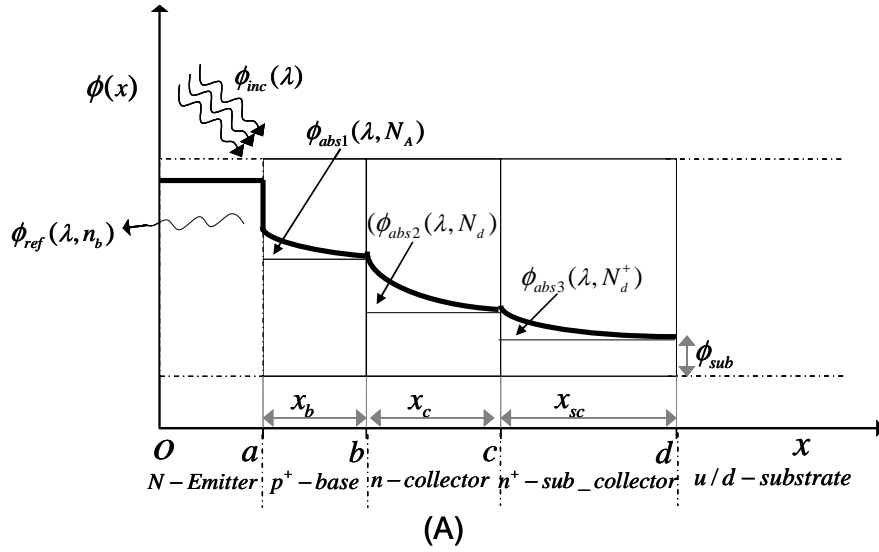


Figure 6-1. Schematic of optical flux absorption and propagation in various layers of sHPT (A) along with the flux reflections in the base layer of a DHPT (B).

$$\begin{aligned}
 (\phi_{abs})_b &= \phi_o (1 - \exp^{-\alpha_b x_b}) + \phi_o R_{f,b/c} \exp^{-\alpha_b x_b} (1 - \exp^{-\alpha_b x_b}) \\
 &\quad + \phi_o R_f R_{f,b/c} \exp^{-2\alpha_b x_b} (1 - \exp^{-\alpha_b x_b})
 \end{aligned} \tag{6.3}$$

$$(\phi_{abs})_b = \phi_o (1 - \exp^{-\alpha_b x_b}) (1 + R_{f,b/c} \exp^{-\alpha_b x_b} + R_f R_{f,b/c} \exp^{-2\alpha_b x_b}) \tag{6.4}$$

The second reflection from the base-collector junction ($x = b$) will result in an additional component which gives:

$$\begin{aligned}
 (\phi_{abs})_b &= \phi_o (1 - \exp^{-\alpha_b x_b}) (1 + R_{f,b/c} \exp^{-\alpha_b x_b} \\
 &\quad + R_f R_{f,b/c} \exp^{-2\alpha_b x_b} + R_f R_{f,b/c}^2 \exp^{-3\alpha_b x_b})
 \end{aligned} \tag{6.5}$$

Hence the total absorption in base region can be written as:

$$(\phi_{abs})_b = \phi_o (1 - \exp^{-\alpha_b x_b}) (1 + R_{f,b/c} \exp^{-\alpha_b x_b} + R_f R_{f,b/c} \exp^{-2\alpha_b x_b} + R_f R_{f,b/c}^2 \exp^{-3\alpha_b x_b} + R_f^2 R_{f,b/c}^2 \exp^{-4\alpha_b x_b} + \dots) \quad (6.6)$$

In order to move towards a closed form solution of (6.6), the infinite term can be rearranged to form a geometric series. Therefore we proceed by arranging terms in (6.7):

$$\frac{(\phi_{abs})_b}{\phi_o (1 - \exp^{-\alpha_b x_b})} = \left[\begin{array}{l} (1 + R_f R_{f,b/c} \exp^{-2\alpha_b x_b} + R_f^2 R_{f,b/c}^2 \exp^{-4\alpha_b x_b} + \dots) \\ + \\ R_{f,b/c} \exp^{-\alpha_b x_b} + R_f R_{f,b/c}^2 \exp^{-3\alpha_b x_b} + R_f^2 R_{f,b/c}^3 \exp^{-5\alpha_b x_b} + \dots \end{array} \right] \quad (6.7)$$

$$\frac{(\phi_{abs})_b}{\phi_o (1 - \exp^{-\alpha_b x_b}) (1 + R_{f,b/c} \exp^{-\alpha_b x_b})} = \left[\begin{array}{l} 1 + R_f R_{f,b/c} \exp^{-2\alpha_b x_b} \\ + \\ R_f^2 R_{f,b/c}^2 \exp^{-4\alpha_b x_b} + \dots \end{array} \right] \quad (6.8)$$

The RHS of (6.8) is an infinite geometric series and it can be summed as shown in (6.9) [15]:

$$(\phi_{abs})_b = \phi_o (1 - \exp^{-\alpha_b x_b}) (1 + R_{f,b/c} \exp^{-\alpha_b x_b}) \left[\sum_{M=0}^{M=\infty} \left[R_f R_{f,b/c} \exp^{-2\alpha_b x_b} \right]^M \right] \quad (6.9)$$

Assuming number of reflections is N , (6.9) can be simplified to (6.10).

$$(\phi_{abs})_{N-reflections} = \phi_o (1 - \exp^{-\alpha_b x_b}) (1 + R_{f,b/c} \exp^{-\alpha_b x_b}) \left[\frac{1 - \left[R_f R_{f,b/c} \exp^{-2\alpha_b x_b} \right]^{N+1}}{1 - \left[R_f R_{f,b/c} \exp^{-2\alpha_b x_b} \right]} \right] \quad (6.10)$$

The first two terms largely characterize the optical absorption behaviour i.e. $R_{f,bc}$ is considerably small and its product with R_f can be ignored for this analysis. However, if an additional layer is added between the base and collector regions to suppress the absorption in the collector and sub-collector, then this analysis will be required in order to model the absorption phenomenon. Now, (6.10) can be approximated as:

$$(\phi_{abs})_b \cong \phi_o (1 - \exp^{-\alpha_b x_b}) (1 + R_{f,b/c} \exp^{-\alpha_b x_b}) \quad (6.11)$$

Thus the total flux absorbed in the base region of a surface illuminated double heterojunction phototransistor is given by (6.11).

6.2 Photocurrent Generation in a DHPT

The time-(and frequency-) dependent photocurrent density generated in the base region can be calculated by first calculating the electron-hole generation rate which is conventionally given as [16]:

$$G(x) = \phi_o \alpha e^{-\alpha x} \quad (6.12)$$

However, if reflections from the base-collection interface are also taken into account then the generation rate can be modified to:

$$G(x) = \phi_o \alpha e^{-\alpha x} + R'_f \phi_o \alpha e^{-\alpha w_b} e^{-\alpha x} \quad (6.13)$$

$$G(x) = \phi_o \alpha e^{-\alpha x} (1 + R'_f e^{-\alpha w_b}) \quad (6.14)$$

The second term in (6.14) adds to the original flux absorbed by taking into account the value of flux at $x = b$ and the Fresnel reflection at base-collector junction. The photocurrent density generated in the base region can now be estimated from (6.15) [17]:

$$I_{ph} = -qA \int_0^{w_b} G(x) \cdot e^{jw(t-\frac{x}{v_s})} dx \quad (6.15)$$

where A is the area of base-emitter junction, w is harmonic frequency and v_s is the saturation velocity of electrons in the base region. Substituting (6.14) into (6.15) gives:

$$I_{ph} = -q \int_0^{w_b} \phi_o \alpha e^{-\alpha x} (1 + R'_f e^{-\alpha w_b}) \cdot e^{jw(t-\frac{x}{v_s})} dx \quad (6.16)$$

$$I_{ph} = -q \phi_o \alpha e^{jw t} (1 + R'_f e^{-\alpha w_b}) \int_0^{w_b} e^{-x(\alpha + \frac{jw}{v_s})} dx \quad (6.17)$$

$$I_{ph} = -q\phi_o e^{j\omega t} (1 + R_f' e^{-\alpha w_b}) \alpha_b W_b \left[\frac{1 - e^{-(\alpha_b W_b + j\omega\tau)}}{\alpha_b W_b + j\omega\tau} \right] \quad (6.18)$$

where τ is the transit time of electrons in the base. It can be seen that (6.18) is consistent with (6.11), as only one reflection from the base-collector surface is taken into consideration. This photocurrent will be represented by a current source in the $\text{In}_{0.49}\text{Ga}_{0.51}\text{P}/\text{GaAs}$ DHPT equivalent circuit given in Section 6-4.

6.3 Small-Signal Model

A small-signal model is useful in modelling device characteristics in terms of lumped components and is widely used in circuit simulations. The cross-sectional view (shown in Figure 6-2) of an NpN HBT along with its associated small-signal lumped-elements is helpful in interpreting the small-signal parameters. It shows a T-shaped equivalent circuit with three added parallel capacitances due to the contact pads. The distributed nature of the base resistance and the base-collector capacitance is modeled by dividing them into only two sub-elements; namely intrinsic and extrinsic parts.

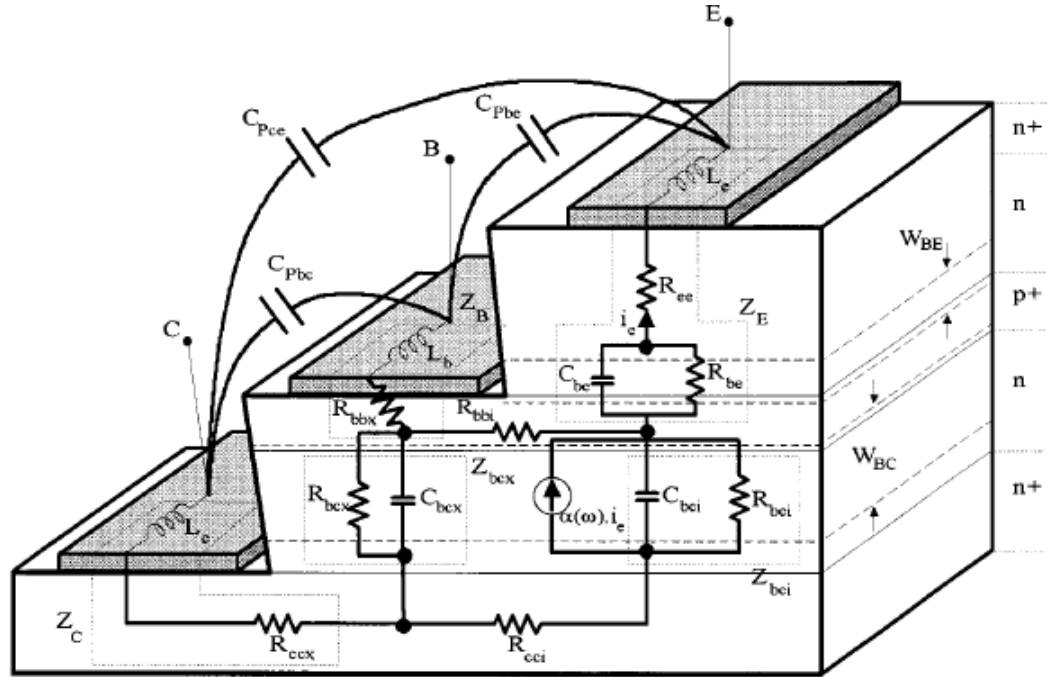


Figure 6-2. Schematic cross-section of a small-geometry npn HBT together with its lumped element T-shape small-signal equivalent circuit. After [18].

It should be noted that parameter extraction has not been performed in this work. However, the extracted modeled parameters have been used to investigate the effect of optical illumination. The lumped elements and the extracted values used in Figure 6-2 are summarized in Table 6-1 [18, 19].

Table 6.1: Extracted parameters for InGaP/GaAs DHBT (16x20 μm^2 BE area).
 $V_{ce} = 3\text{V}$, $V_{be} = 1.2\text{V}$, $I_c = 20\text{mA}$

Component	Description	Value
L_b	Parasitic base Inductance	51.7 pH
L_c	Parasitic collector inductance	75.8 pH
L_e	Parasitic emitter inductance	55.7 pH
τ_b	Base transit time	4.63 psec
τ_c	Collector transit time	2.75 psec
C_{pbe}	Parasitic BE capacitance	24.4 fF
C_{pbc}	Parasitic BC capacitance	5.85 fF
C_{pce}	Parasitic CE capacitance	38.9 fF
C_{bc}	BC junction capacitance	189.5 fF
C_{bci}	Intrinsic BC junction capacitance	$r^* C_{bc} = 108.01 \text{ fF}$
C_{bcx}	Extrinsic BC junction capacitance	$(1-r)^* C_{bc} = 81.49 \text{ fF}$
C_{be}	BE diffusion capacitance	3.39 pF
C_{jbe}	BE junction capacitance	0.563 pF
R_{ee}	Emitter resistance	8.56 Ω
R_{cc}	Collector resistance	17.02 Ω
R_{bbi}	Intrinsic series base resistance	31.02 Ω
R_{bbx}	Extrinsic series base resistance	1.19 Ω
R_{be}	BE junction resistance	1.36 Ω
R_{bc}	BC junction resistance	20.77 k Ω
R_{bci}	Intrinsic BC junction resistance	$R_{bc} / r = 36.43 \text{ k}\Omega$
R_{bcx}	Extrinsic BC junction resistance	$R_{bc} / (1-r) = 48.3 \text{ k}\Omega$

r	Ratio of BE area to BC area	16/26=0.61
---	-----------------------------	------------

6.4 Results and Discussion

It has been established that the optical signal propagates through the base of the device towards the collector and sub-collector regions; however, it will not contribute towards the photoresponse due to the existing energy gap between the base and the collector heterostructure. The photoabsorption in the base region will, nevertheless, affect the associated intrinsic capacitance and resistances which will influence the device characteristics. A careful analysis of this phenomenon along with detailed absorption analysis is important for accurate DHPT device modeling and this will be discussed in this section.

The significant modification in the small-signal modeling for surface-illuminated DHPTs as compared to that of sHBTs is the introduction of an optically-controlled current source between the base and the emitter of a device as shown in Figure 6-3. The parameters terminating with the subscript 'x' are extrinsic parameters which are bias independent or have no effect to incident optical signal. However, the parameters ending with 'i' are intrinsic and change with optical input.

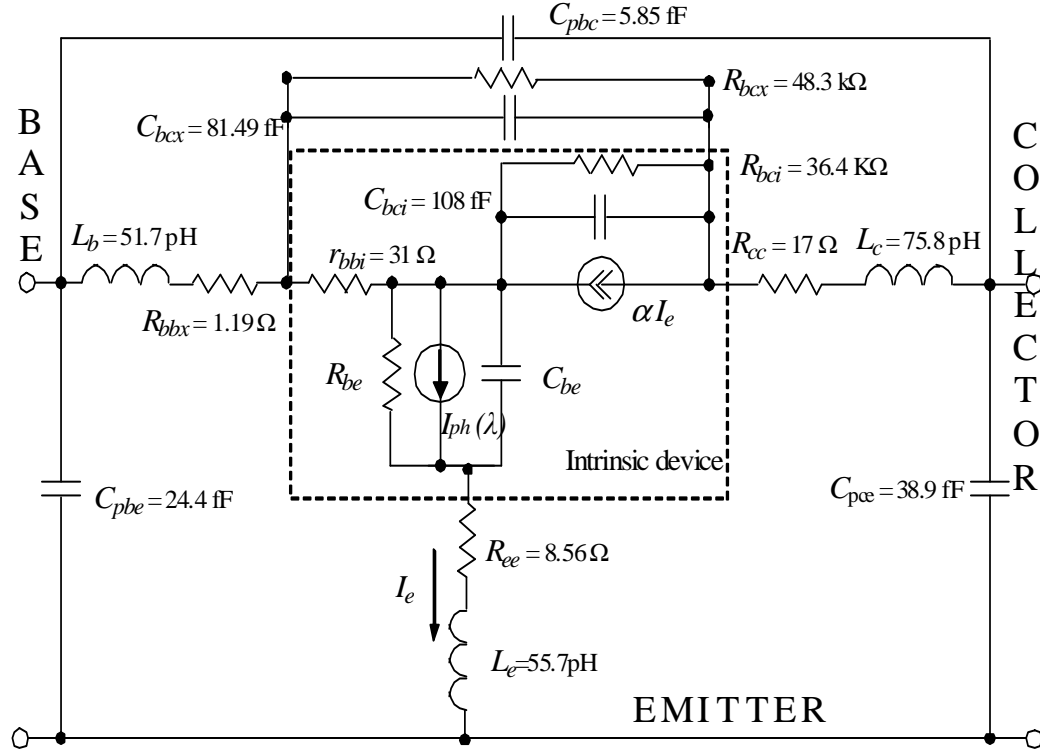


Figure 6-3. Small-signal equivalent of the $\text{In}_{0.49}\text{Ga}_{0.51}\text{P}/\text{GaAs}$ DHBT in common source mode indicating intrinsic and extrinsic parameters.

The base-collector depletion and sub-collector region ($\text{In}_{0.49}\text{Ga}_{0.51}\text{P}$ band gap of 1.90 eV [20, 21]) is transparent to an incident wavelength of 850 nm. The measured output characteristics of the $\text{In}_{0.49}\text{Ga}_{0.51}\text{P}/\text{GaAs}$ DHBT at $I_c = 20 \text{ mA}$ and $V_{be} = 1.2 \text{ V}$ along with the simulated photoresponse at $P_{inc} = 10.4 \text{ }\mu\text{W}$ is shown in Figure 6-4. The DC responsivity of the device has a maximum of 22 (A/W) and has been closely modelled through the small-signal elements shown in Figure 6-3.

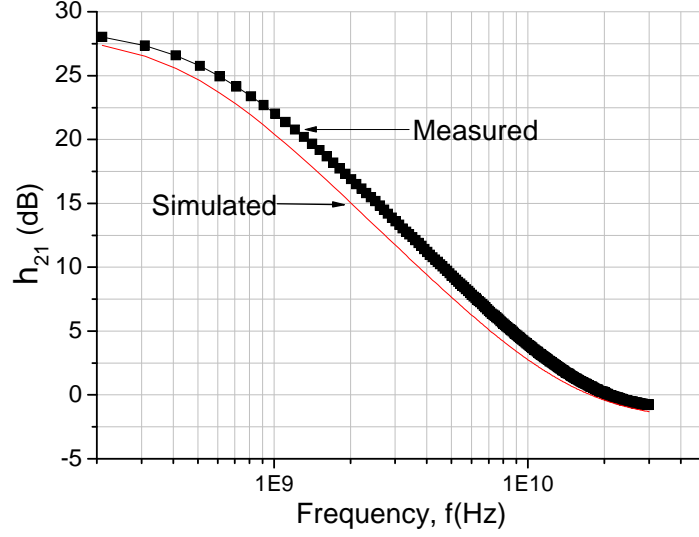


Figure 6-4. Measured and simulated h_{21} of the $\text{In}_{0.49}\text{Ga}_{0.51}\text{P}/\text{GaAs}$ DHBT, $V_{ce}=3\text{ V}$.

A variation in optical signal will modify the intrinsic elements of the device which in turn will affect the photoresponse. Since the collector of the device is $\text{In}_{0.49}\text{Ga}_{0.51}\text{P}$, which is largely transparent to incoming optical signal of 850 nm, the BC resistances and capacitances will remain unaffected. In the case of single-HPTs, these intrinsic parameters will also change, however this is out of the scope of this research. BE resistance and capacitance will nevertheless be affected with the change in the optical intensity which may affect the photoresponse and cut-off frequency variation of the device. The emitter base charging time (τ_{EB}) will also be directly be affected by C_{be} and changing optical power as observed from (6.20) [22, 23]:

$$\tau_{EB} = \frac{KThc}{q^2 \eta P_{inc} h_{FE}} (C_{be} + C_{bc}) \quad (6.20)$$

$$\text{where } R_{be} = \frac{KThc\gamma_1}{q^2 \eta P_{inc} h_{FE}} \quad (6.21)$$

C_{bc} will remain independent of incident signal variation, however C_{be} will be affected by the introduction of more carriers in the base region. This base-emitter capacitance, largely due to the diffusion of carriers, will increase if the incident signal intensity

increases. This increase in the capacitance should lower the h_{21} /photoresponse and the diffusion capacitance can be written as [24],

$$C_{be} = \frac{Aq^2 L_n n_{po} \gamma_2}{KT} \frac{I_{ph}}{I_s} \quad (6.22)$$

$$\text{and } I_s = \frac{AqD_n n_{po}}{L_n} \quad (6.23)$$

where I_s is the saturation current for the device and can be approximated by (6.23). Simulation parameters, γ_1 and γ_2 , have been included in (6.21) and (6.22) in order to match the extracted ones in Table 4-1.

The intrinsic base-emitter resistance, on the other hand, will be lowered by the increase in the photocarriers in the base region (R_{be} inversely proportional to P_{inc}). Thus, the increase in the diffusion capacitance is accompanied by the reduction of intrinsic resistance. This variation along with the capacitance variation, with optical power is seen in Figure 6-5.

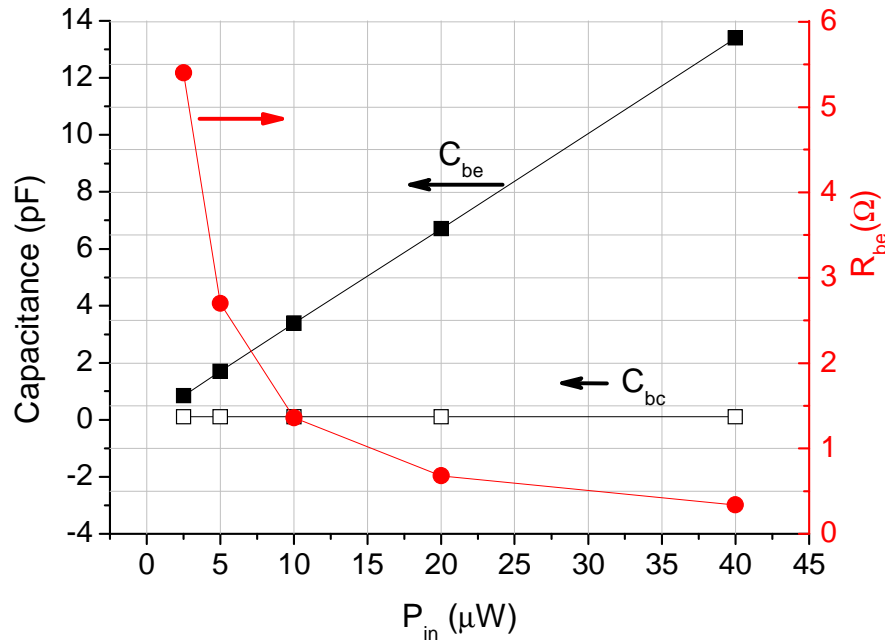


Figure 6-5. Variation of base emitter capacitance and resistance and base collector capacitance with input optical power, $In_{0.49}Ga_{0.51}P/GaAs$ DHPT.

The variation of intrinsic base-collector resistance is negligible as photoabsorption in the collector is nominal. However, a sizeable variation in the intrinsic series base resistance R_{bbi} can be expected. Circuit simulation for small signal model of $\text{In}_{0.49}\text{Ga}_{0.51}\text{P}/\text{GaAs}$ DHPT shows that the variation of h_{21} is minimal with variation of R_{bbi} and the result is summarised in Figure 6-6. The value of h_{21} ranges from 7.1 dB to 7.2 dB and therefore it can be inferred that any variation in R_{bbi} does not have any significant effect on the h_{21} variation with incident power variation.

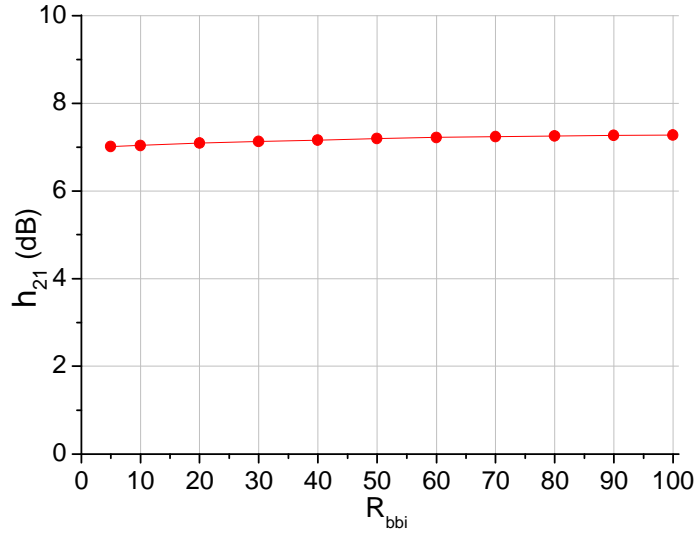


Figure 6-6. Variation of the photoresponse with intrinsic base resistance at 4 GHz for the $\text{In}_{0.49}\text{Ga}_{0.51}\text{P}/\text{GaAs}$ DHPT.

The photoresponse due to the variation of intrinsic capacitances and resistance is shown in Figure 6-7. The change in the photoresponse with R_{bbi} is rather minute suggesting that the two major parameters (R_{be} and C_{be}) balance each other out. Nevertheless, a small increase in the photoresponse has been observed with the increase in power suggesting that the lower resistance should be the focus for the design of HPTs. Lower base and BE resistance is achieved by using multifinger contacts (mostly for extrinsic BE resistance), high carrier concentration in the base and a relatively large base-emitter area [25-27].

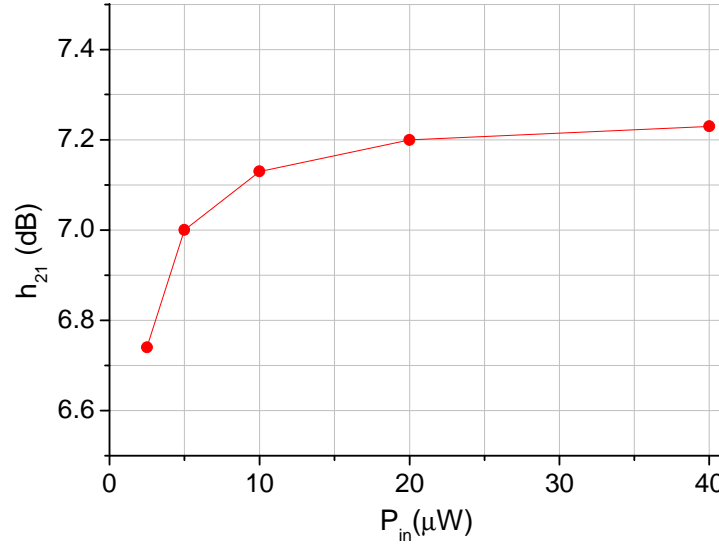


Figure 6-7. Photoresponse variation with input optical power for the $In_{0.49}Ga_{0.51}P/GaAs$ DHPT at 4 GHz.

This analysis has been performed for DHPTs and it is worth mentioning that the analysis of sHPTs will differ as the intrinsic part of C_{bc} varies with the optical signal intensity, thus affecting the photoresponse. It should also be noted that the magnitude of photogenerated current will increase as absorbing layer includes base, collector and sub-collector regions. However, the carrier transit times will also increase resulting in the deterioration of the frequency response. All of these parameters should be carefully analysed for sHPT modeling.

References

- [1] J. P. Helme, P. A. Houston, and C. H. Tan, "Large-signal charge control modeling of photoreceivers for applications up to 40 Gb/s," *IEEE Journal of Quantum Electronics*, vol. 45, pp. 833-839, 2009.
- [2] M. Muller, S. Withitsoonthorn, M. Riet, J.-L. Benchimol, and C. Gonzalez, "Millimeter-Wave InP/InGaAs Photo-HBT and Its Application to Optoelectronic Integrated Circuits," *IEICE Transactions on Electronics*, vol. E86-C, pp. 1299-1310, 2003.
- [3] Z. Pei, C. S. Liang, L. S. Lai, Y. T. Tseng, Y. M. Hsu, P. S. Chen, S. C. Lu, C. M. Liu, M.-J. Tsai, and C. W. Liu, "High efficient 850 nm and 1,310 nm multiple quantum well SiGe/Si heterojunction phototransistors with 1.25 Plus GHz bandwidth (850 nm)," presented at 2002 IEEE International Devices Meeting (IEDM), December 8, 2002 - December 11, 2002, San Francisco, CA, United states, 2002.
- [4] D. Ritter, B. Sheinman, V. Sidorov, S. Cohen, A. Gavrilov, Y. Vered, G. Zohar, and J. Lasri, "Optimization of InP/GaInAs heterojunction bipolar transistors and phototransistors," presented at Proceedings of International Topical Meeting on Microwave Photonics (MWP2002), 5-8 Nov. 2002, Tokyo, Japan, 2002.
- [5] M. N. R. Abedin, Tamer F. Sulima, Oleg V. Singh, Upendra N., "AlGaAsSb-InGaAsSb HPTs with high optical gain and wide dynamic range," *IEEE Transactions on Electron Devices*, vol. 51, pp. 2013-2018, 2004.
- [6] S. Chandrasekhar, M. K. Hoppe, A. G. Dentai, C. H. Joyner, and G. J. Qua, "Demonstration of enhanced performance of an InP/InGaAs heterojunction phototransistor with a base terminal," *IEEE Electron Device Letters*, vol. 12, pp. 550-2, 1991.
- [7] P. A. Chakrabarti, N.K. Kalra, P. Agrawal, S. Gupta, G., "Noise modeling of an InP/InGaAs heterojunction bipolar phototransistor," *Optical Engineering*, vol. 42, pp. 939-47, 2003.
- [8] J. Kim, W. B. Johnson, S. Kanakaraju, and C. H. Lee, "Lateral InP/InGaAs double heterojunction phototransistor over a trenching interdigitated finger structure," *Solid-State Electronics*, vol. 51, pp. 1023-1028, 2007.

- [9] H. Kamitsuna, Matsuoka Y., Yamahata S., Shigekawa, N., "Ultrahigh-speed InP/InGaAs DHPTs for OEMMICs," *IEEE Transactions on Microwave Theory and Techniques*, vol. 49, pp. 1921-1925, 2001.
- [10] A. H. Leven, V. Kopf, R. Baeyens, Y. Chen, Y.-K., "InP-based double-heterostructure phototransistors with 135 GHz optical-gain cutoff frequency," *Electronics Letters*, vol. 40, pp. 833-834, 2004.
- [11] C. Gonzales, "InP based phototransistors and comparison of performance to those of PIN and UTC photodiodes," presented at International symposium on microwave photonics (Invited paper), Budapest, Hungary, 2003.
- [12] C. Gonzalez, J. Thuret, J. L. Benchimol, and M. Riet, "Optoelectronic up-converter to millimetre-wave band using an heterojunction bipolar phototransistor," presented at Proceedings of the 1998 24th European Conference on Optical Communication, ECOC. Part 1 (of 3), September 20, 1998 - September 24, 1998, Madrid, Spain, 1998.
- [13] J. Thuret, C. Gonzalez, J. L. Benchimol, M. Riet, and P. Berdagner, "High-speed InP/InGaAs heterojunction phototransistor for millimetre-wave fibre radio communications," *Proceedings of the 1999 11th International Conference on Indium Phosphide and Related Materials (IPRM)*, May 16, 1999 - May 20, 1999, pp. 389-392, 1999.
- [14] J. Thuret, C. Gonzalez, M. Riet, and J. L. Benchimol, "Enhanced performance of InP/InGaAs HBT phototransistor with an improved base contact design," 1998.
- [15] K. A. Stroud, *Engineering Mathematics*, 4th ed: Bath Press, 1995.
- [16] A. A. de Salles, A. S. Hackbart, and L. N. Spalding, "A simple model for the GaAs HBT high-frequency performance under optical illumination," *Microwave and Optical Technology Letters*, vol. 7, pp. 392-5, 1994.
- [17] W. Gartner, "Depletion-Layer Photoeffects in Semiconductors," *Physics Review*, vol. 116, pp. 84-87, 1959.
- [18] M. Sotoodeh, L. Sozzi, A. Vinay, A. H. Khalid, Z. Hu, A. H. A. Rezazadeh, and R. Menozzi, "Stepping toward standard methods of small-signal parameter extraction for HBT's," *IEEE Transactions on Electron Devices*, vol. 47, pp. 1139-1151, 2000.
- [19] S. Chitrashekaraiah, V. T. Vo, and A. A. Rezazadeh, "Linear temperature dependent small signal model for InGaP/GaAs DHBTs using IC-CAP,"

- presented at 2006 IEEE MTT-S International Microwave Symposium Digest, June 11, 2006 - June 16, 2006, San Francisco, CA, United states, 2006.
- [20] J. Novak, S. Hasenohrl, M. I. Alonso, and M. Garriga, "Influence of tensile and compressive strain on the band gap energy of ordered InGaP," *Applied Physics Letters*, vol. 79, pp. 2758, 2001.
 - [21] J. Novak, S. Hasenohrl, R. Kudela, M. Kucera, M. I. Alonso, and M. Garriga, "Effect of strain and ordering on the band-gap energy of InGaP," 2002.
 - [22] R. A. Milano, P. D. Dapkus, G. E. Stillman, and G. E. Stillman, "An analysis of the performance of heterojunction phototransistors for fiber optic communications," *IEEE Transactions on Electron Devices*, vol. ED-29, pp. 266-74, 1982.
 - [23] S. M. Sze, *Physics of Semiconductor Devices*, 2nd ed. USA: John Wiley & Sons, 2001.
 - [24] S. M. Sze, *Semiconductor Devices: Physics and Technology*: John Wiley & Sons, 1985.
 - [25] A. A. Rezazadeh, M. Sotoodeh, and N. Dharmasiri, "Base-collector design optimisation of InGaP/GaAs DHBTs," presented at 8th IEEE International Symposium on High Performance Electron Devices for Microwave and Optoelectronic Applications (EDMO 2000), November 13, 2000 - November 14, 2000, Glasgow, United kingdom, 2000.
 - [26] K. L. Koon, Z. Hu, A. A. Rezazadeh, and S. Marsh, "Design optimisation of HBT broadband distributed amplifiers," presented at 2001 International Symposium on Electron Devices for Microwave and Optoelectronic Applications, November 15, 2001 - November 16, 2001, Vienna, Austria, 2001.
 - [27] J. J. Liou and A. A. Rezazadeh, "Base current instability of AlGaAs/GaAs HBTs operated at low voltages," presented at 1999 IEEE Hong Kong Electron Devices Meeting (HKEDM99), June 26, 1999 - June 26, 1999, Shatin, Hong Kong, 1999.

Chapter 7

Conclusions and Further Work

7.1 Summary and Conclusions

In order to model the spectral response of heterojunction phototransistors, various aspects of these devices from the material and structural point of view have been analysed and discussed in this work. The responsivity of a phototransistor depends on several inherent factors including the material absorption coefficient, refractive index, device structure, doping and temperature of operation along with external factors such as bias voltage and the energy of incident radiation. Optical gain depends on coupling efficiency, collection efficiency and the internal gain of the transistor. A thorough understanding of these parameters is vital in the design optimisation of future phototransistors.

The absorption model presented in this thesis provides an insight into spectral response modelling of GaAs-based HPTs for short-wavelength detection. It was shown that the optical collection efficiency, being strictly geometry- and wavelength-dependent, should not be considered unity across short-wavelength spectra. A decrease in the collection efficiency for the $\text{Al}_{0.3}\text{Ga}_{0.7}\text{As}/\text{GaAs}$ HPT was observed for wavelengths beyond 700 nm which resulted in smaller values of responsivity. This decrease in the collection efficiency has been attributed to an increased photo-absorption in the substrate which does not contribute towards the photoresponse.

For accurate spectral response modelling, it is shown that variations in the absorption coefficient with changes in the band gap (due to doping) should also be incorporated for the construction of the optical absorption profile. Optical absorption, at wavelengths close to the band gap of a semiconductor material, was shown to be a layer-dependent phenomena and the generalisation of optical flux absorption profile as a single exponential has been highly plausible for GaAs-based HPTs. This was evident from the absorption pattern in the $\text{Al}_{0.3}\text{Ga}_{0.7}\text{As}/\text{GaAs}$ HPT at 850 nm and to

some extent at 780 nm. The detailed absorption model and the critical analysis of several important parameters for GaAs-HPTs thus become inevitable for efficient device modelling.

InP-based devices have also been investigated for medium and long wavelength detection. The absorption model developed was also valid for the accurate modelling of the spectral response of lattice matched InP/In_{0.47}Ga_{0.53}As HPTs. The variation of collection efficiency at various incident wavelengths was also evident in this material system and should always be incorporated in the modelling. However, the variation of absorption coefficient with doping at 1310 nm and 1550 nm is rather minimal which makes absorption in the InGaAs collector and sub-collector largely exponential.

The absolute spectral response and optical characteristics of HPTs have been predicted with the aid of this modified model and prior knowledge of device electrical characteristics. Therefore the knowledge of the current gain of the device has been a prerequisite for this analysis. This limited the utility of this work and therefore further work on analytical modelling of the SR was carried out. The analytical model developed in this work directly highlights the critical device and material properties affecting the spectral response of heterojunction phototransistors.

The analytical spectral response model in this work has been based on the analysis of excess minority photocarrier generation, diffusion and recombination by applying semiconductor continuity equations. Accurate boundary conditions, for active regions of a phototransistor, were described in the theoretical model for efficient device performance. These were modelled by incorporating a wavelength dependent surface recombination parameter $z(\alpha)$. $z(\alpha)$ modelled the surface recombination at lower wavelengths as more photocarriers were generated near the surface. The variation of $z(\alpha)$ for both Al_{0.3}Ga_{0.7}As/GaAs HPTs and InP/In_{0.47}Ga_{0.53}As HPTs followed a near exponential decay with increasing wavelengths which has been consistent with power absorption in semiconductors. Higher values of $z(\alpha)$ at lower wavelengths implied that a considerable amount of photogenerated carriers, in the surface vicinity, would be lost due to recombination. Thus, these recombined carriers would not participate in the photocurrent.

Furthermore the variation of the base width of the device affecting the responsivity for both material systems has been investigated. For $\text{Al}_{0.3}\text{Ga}_{0.7}\text{As}/\text{GaAs}$ HPTs, an increase in the base width resulted in an increase in the bulk and surface recombination. A Larger amount of photocarriers was generated near the surface for a wavelength of 500 nm as compared to 635 nm and therefore the surface recombination parameter is larger for the 500 nm case, resulting in a sharp drop in the responsivity at this wavelength. At 850 nm, an increase in recombination has been compensated by the increased number of photocarriers in the base region. Considering the case for $\text{InP}/\text{In}_{0.47}\text{Ga}_{0.53}\text{As}$ HPTs, the responsivity generally decreased with the increase in base layer width, but at 1550 nm the rate of decrease was slightly higher, which has been associated with the low absorption coefficient in the base layer ($0.85 \times 10^4 / \text{cm}$).

Photoabsorption in DHPTs has also been investigated in this work. It has been shown that the absorption in sHPTs differs to that in DHPTs and a modified model for absorption in DHPTs has therefore been presented. The optical flux absorbed in the base region only contributed towards the photoresponse. The optical power absorbed in the collector and sub-collector region did not contribute towards the photoresponse due to the existence of an additional heterostructure at the base-collector junction of DHPTs.

A detailed analysis performed on a modified small-signal model of DHPTs gave insightful information about the variation of various intrinsic parameters with the incident optical signal. It has been observed that the variation of intrinsic base-collector resistance is negligible since photoabsorption in the collector region is nominal. The base-emitter capacitance, on the other hand, was largely due to the diffusion of carriers which increased with the increase in signal intensity. The intrinsic base-emitter resistance was lowered by the increase in the photocarriers in the base region as it is inversely proportional to the signal intensity. The variation in the photoresponse of DHPTs with variation in intrinsic series base resistance is minimal. Hence observations, in addition to the detailed photoabsorption model, can be used in optimizing the device frequency response for optimal performance.

In summary, a detailed analysis of heterojunction bipolar phototransistors has been presented in this thesis with the emphasis on InP- and GaAs-based devices. The analytical expressions for responsivity of these devices and the critical analysis of several important parameters for HPTs presented here can be utilised for performance enhancement through device optimisation for sensors, photoreceivers in optical networks and remote sensing applications employing integrated circuits.

7.2 Further Work

This thesis has provided a solid foundation for the modelling of heterojunction bipolar phototransistors, however, further investigation is required to attain a complete semi-physical compact model. This short section will introduce a number of new possible upgrades to the existing model presented in this thesis.

- The experimental set-up may be modified to measure the responsivity of GaAs-based devices for wavelengths below 600 nm.
- The InP- and GaAs-based material systems have been mainly discussed and investigated in this work and analysis on the optical absorption of other relevant materials such as Si and GaAsSb might also be performed.
- The responsivity analysis for sHPTs should be compared with DHPTs with similar layer structures.
- Further investigation of HPT responsivity with variation in doping, temperature and material should be carried out.
- For completeness of the model, the impact of several physical effects such as base push-out and extreme forward biasing of the base-emitter junction may be investigated along with the sensitivity analysis and low bias operation of HPTs.
- The analytical model should be incorporated with the high-speed response of the HPTs and the RF response of the devices could also be modelled.
- The formulae developed in the analytical model should be incorporated into a graphical user interface to create a user friendly environment.
- A study on transparent emitter contacts for microwave geometry devices could also be looked at for the purpose of high coupling efficiency.

- The development of the temperature-dependent empirical formulae for device parameters, such as lifetimes, is required for the quantitative study of temperature behaviour of various HPTs.
- Edge-illuminated HPTs might be analysed for a comparison with the surface illuminated DHPTs described in this work.

Appendices

Appendix A: Matlab code for generation of flux absorption profile for GaAs-based HPT.

```
% wavelength = 635 nm (COMMENTS SHOWN IN GREEN COLOR)
clc
clear
close all
for Po=100e-6:100e-6:100e-6;
alphaB=3.46;
alphaC=3.46;
alphaSC=3.46;
Lb=0:.03:.09
Lc=0:.1:.5
Lsc=0:.1:1
Rf=(3.826-1)/(4.826);
Rf=Rf^2;

Pt=0.512*Po*(1-Rf)/1.6e-19;
%pt is input flux and pt=po/E;
Pb=Pt*exp(-alphaB*Lb)
magPb=Pt*(1-exp(-alphaB*.09));
Pc=(Pt-magPb)*exp(-alphaC*Lc)
magPc=(Pt-magPb)*(1-exp(-alphaC*.5));
Psc=Pc(length(Lc))*exp(-alphaSC*Lsc)
magPsc=(Pt-magPb-magPc)*(1-exp(-alphaSC*1));
Psub=Pt-(magPb+magPc+magPsc);
Pabs=Pt-Psub;

xxx(round(Po/100e-6)) = Pabs;
bbb(round(Po/100e-6)) = magPb;
ccc(round(Po/100e-6)) = magPc;
sc(round(Po/100e-6))= magPsc;
sub(round(Po/100e-6)) = Psub;
%SUBPLOT(121)
plot(100e-6:100e-6:1000e-6,Pabs)
Lt=0:.1e-6:1e-6;
asd=plot(Lc+.09,Pc,'-o');
hold on
asdf=plot(Lb,Pb,'.-');
hold on
asdfg=plot(Lsc+.59,Psc,'-*');
hold on
end
grid on
legend([asdf,asd,asdfg], 'base', 'collector', 'sub-collector')
YLABEL('Flux absorption profile (photons/second)')
XLABEL('Distance (um)')
%.....

for Po=100e-6:100e-6:100e-6;
alphaB=0.65;%for 850nm
alphaC=.86;
alphaSC=.1;
% alphaB=0.53; for 840nm
% alphaC=1;
```

```

% alphaSC=.15;
Lb=0:.03:.09;
Lc=0:.1:.5;
Lsc=0:.1:1;
Rf=(3.63-1)/(4.63);
Rf=Rf^2;
Pt=0.685*Po*(1-Rf)/1.6e-19;%850nm and .675 for 840nm

Pb=Pt*exp(-alphaB*Lb);
magPb=Pt*(1-exp(-alphaB*.09))
Pc=Pb(4)*exp(-alphaC*Lc)
magPc=(Pt-magPb)*(1-exp(-alphaC*.5));
Psc=Pc(length(Lc))*exp(-alphaSC*Lsc);
magPsc=(Pt-magPb-magPc)*(1-exp(-alphaSC*1));
Psub=Pt-(magPb+magPc+magPsc)
Pabs=Pt-Psub
%SUBPLOT(122)
asd=plot(Lc+.09,Pc,'-o')
hold on
asdf=plot(Lb,Pb,'.-')
hold on
asdfg=plot(Lsc+.59,Psc,'-*')
hold on
end
legend([asdf,asd,asdfg],'base','collector','sub-collector')
grid on
YLABEL('Flux absorption profile (photons/second)')
XLABEL('Distance (um)')
hold on
%.

for Po=100e-6:100e-6:100e-6;
alphaB=1;%for 800nm
alphaC=1.49;
alphaSC=.94
Lb=0:.03:.09
Lc=0:.1:.5
Lsc=0:.1:1
Rf=(3.67-1)/(4.67);
Rf=Rf^2;

Pt=0.629*Po*(1-Rf)/1.6e-19;
Pb=Pt*exp(-alphaB*Lb)
magPb=Pt*(1-exp(-alphaB*.09));
Pc=(Pt-magPb)*exp(-alphaC*Lc)
magPc=(Pt-magPb)*(1-exp(-alphaC*.5));
Psc=Pc(length(Lc))*exp(-alphaSC*Lsc)
magPsc=(Pt-magPb-magPc)*(1-exp(-alphaSC*1));
Psub=Pt-(magPb+magPc+magPsc);
Pabs=Pt-Psub;

xxx(round(Po/100e-6)) = Pabs;
bbb(round(Po/100e-6)) = magPb;
ccc(round(Po/100e-6)) = magPc;
sc(round(Po/100e-6))= magPsc;
sub(round(Po/100e-6)) = Psub;
%SUBPLOT(121)
plot(100e-6:100e-6:1000e-6,Pabs)
Lt=0:.1e-6:1e-6;
asd=plot(Lc+.09,Pc,'-o');

```

```

hold on
asdf=plot(Lb,Pb,'.-');
hold on
asdfg=plot(Lsc+.59,Psc,'-*');
hold on
end
grid on
legend([asdf,asd,asdfg],'base','collector','sub-collector')
YLABEL('Flux absorption profile (photons/second)')
XLABEL('Distance (um)')
hold on
%.

for Po=100e-6:100e-6:100e-6;
alphaB=2.74;%for 700nm
alphaC=2.74;
alphaSC=2.74;
Lb=0:.03:.09
Lc=0:.1:.5
Lsc=0:.1:1
Rf=(3.78-1)/(4.78);
Rf=Rf^2;
Pt=0.564*Po*(1-Rf)/1.6e-19;
Pb=Pt*exp(-alphaB*Lb)
magPb=Pt*(1-exp(-alphaB*.09));
Pc=(Pt-magPb)*exp(-alphaC*Lc)
magPc=(Pt-magPb)*(1-exp(-alphaC*.5));
Psc=Pc(length(Lc))*exp(-alphaSC*Lsc)
magPsc=(Pt-magPb-magPc)*(1-exp(-alphaSC*1));
Psub=Pt-(magPb+magPc+magPsc);
Pabs=Pt-Psub;

xxx(round(Po/100e-6)) = Pabs;
bbb(round(Po/100e-6)) = magPb;
ccc(round(Po/100e-6)) = magPc;
sc(round(Po/100e-6))= magPsc;
sub(round(Po/100e-6)) = Psub;
%SUBPLOT(121)
plot(100e-6:100e-6:1000e-6,Pabs)
Lt=0:.1e-6:1e-6;
asd=plot(Lc+.09,Pc,'-o');
hold on
asdf=plot(Lb,Pb,'.-');
hold on
asdfg=plot(Lsc+.59,Psc,'-*');
hold on
end
grid on
legend([asdf,asd,asdfg],'base','collector','sub-collector')
YLABEL('Flux absorption profile (photons/second)')
XLABEL('Distance (um)')
hold on
%.

for Po=100e-6:100e-6:100e-6;
alphaB=11.7;%for 500nm
alphaC=11.7;
alphaSC=11.7;
Lb=0:.03:.09
Lc=0:.1:.5
Lsc=0:.1:1

```

```

Rf=(4.333-1)/(5.333);
Rf=Rf^2;
Pt=0.403*Po*(1-Rf)/1.6e-19;
Pb=Pt*exp(-alphaB*Lb)
magPb=Pt*(1-exp(-alphaB*.09));
Pc=(Pt-magPb)*exp(-alphaC*Lc)
magPc=(Pt-magPb)*(1-exp(-alphaC*.5));
Psc=Pc(length(Lc))*exp(-alphaSC*Lsc)
magPsc=(Pt-magPb-magPc)*(1-exp(-alphaSC*1));
Psub=Pt-(magPb+magPc+magPsc);
Pabs=Pt-Psub;

xxx(round(Po/100e-6)) = Pabs;
bbb(round(Po/100e-6)) = magPb;
ccc(round(Po/100e-6)) = magPc;
sc(round(Po/100e-6))= magPsc;
sub(round(Po/100e-6)) = Psub;
%SUBPLOT(121)
plot(100e-6:100e-6:1000e-6,Pabs)
Lt=0:.1e-6:1e-6;
asd=plot(Lc+.09,Pc,'-o');
hold on
asdf=plot(Lb,Pb,'.-');
hold on
asdfg=plot(Lsc+.59,Psc,'-*');
hold on
end
grid on
legend([asdf,asd,asdfg],'base','collector','sub-collector')
YLABEL('Flux absorption profile (photons/second)')
XLABEL('Distance (um)')
hold on

```

Appendix B: Photogenerated current in various layers of GaAs-based HPT

```
% wavelength = 850 nm
clc
clear
close all
for Po=100e-6:100e-6:400e-6;
alphaB=0.50;%for 850nm
alphaC=.86;
alphaSC=.02
Lb=0:.01:.09;
Lc=.1:.01:.6;
Lsc=0.61:.01:1.61;
Rf=(3.64-1)/(4.64);
Rf=Rf^2;

Pt=0.685*Po*(1-Rf);%/1.6e-19;%850nm

Pb=Pt*exp(-alphaB*Lb);
magPb=Pt*(1-exp(-alphaB*.09))
Pc=Pb(1)*exp(-alphaC*Lc);
magPc=(Pt-magPb)*(1-exp(-alphaC*.5))
Psc=Pc(length(Lc)-8)*exp(-alphaSC*Lsc);
magPsc=(Pt-magPb-magPc)*.84*(1.18-exp(-alphaSC*1));
Psub=Pt-(magPb+magPc+magPsc)
Pabs=Pt-Psub

xxx(round(Po/100e-6)) = Pabs
bbb(round(Po/100e-6)) = magPb
ccc(round(Po/100e-6)) = magPc
sc(round(Po/100e-6))= magPsc
sub(round(Po/100e-6)) = Psub
plot(100e-6:100e-6:1000e-6,Pabs)
Lt=0:.1e-6:1e-6;
end
Figure
SUBPLOT(223)
plot(1000*[100e-6:100e-6:400e-6],xxx./[100e-6:100e-6:400e-6],'-*');
hold on
plot(1000*[100e-6:100e-6:400e-6],bbb./[100e-6:100e-6:400e-6],'-p');
hold on
plot(1000*[100e-6:100e-6:400e-6],ccc./[100e-6:100e-6:400e-6],'-');
hold on
plot(1000*[100e-6:100e-6:400e-6],sc./[100e-6:100e-6:400e-6],'-o');
hold on
plot(1000*[100e-6:100e-6:400e-6],sub./[100e-6:100e-6:400e-6],'-rs')
AXIS([0.05 .45 0 0.35])
XLABEL('Input power(mW) [\lambda=840nm]')
YLABEL('Responsivity (mA/mW) ')
hold on
Figure
SUBPLOT(224)
plot(1000*[100e-6:100e-6:400e-6],1000000*xxx,'-*')
hold on
plot(1000*[100e-6:100e-6:400e-6],1000000*bbb,'-p')
hold on
plot(1000*[100e-6:100e-6:400e-6],1000000*ccc,'-')
hold on
```

```

plot(1000*[100e-6:100e-6:400e-6],1000000*sc,'-o')
hold on
plot(1000*[100e-6:100e-6:400e-6],1000000*sub,'-rs')
AXIS([0.05 .45 0 100])
XLABEL('Input power(mW) [ $\lambda$ =840nm]')
YLABEL('Photogenerated current ( $\mu$ A) ')
hold on
for Po=100e-6:100e-6:400e-6;
alphaB=3.46;
alphaC=3.46;
alphaSC=3.46;
Lb=0:.01:.09;
Lc=.1:.01:.6;
Lsc=0.61:.01:1.61;
Rf=(3.826-1)/(4.826);
Rf=Rf^2;

Pt=0.523*Po*(1-Rf);

Pb=Pt*exp(-alphaB*Lb);
magPb=Pt*(1-exp(-alphaB*.09))
Pc=Pb*(1)*exp(-alphaC*Lc);
magPc=(Pt-magPb)*(1-exp(-alphaC*.5))
Psc=Pc*(length(Lc)-8)*exp(-alphaSC*Lsc);
magPsc=(Pt-magPb-magPc)*(1-exp(-alphaSC*1));
Psub=Pt-(magPb+magPc+magPsc)
Pabs=Pt-Psub

xxx(round(Po/100e-6)) = Pabs
bbb(round(Po/100e-6)) = magPb
ccc(round(Po/100e-6)) = magPc
sc(round(Po/100e-6))= magPsc
sub(round(Po/100e-6)) = Psub
plot(100e-6:100e-6:1000e-6,Pabs)
end
%Figure
SUBPLOT(221)
plot(1000*[100e-6:100e-6:400e-6],xxx./[100e-6:100e-6:400e-6],'-*')
hold on
plot(1000*[100e-6:100e-6:400e-6],bbb./[100e-6:100e-6:400e-6],'-p')
hold on
plot(1000*[100e-6:100e-6:400e-6],ccc./[100e-6:100e-6:400e-6],'-')
hold on
plot(1000*[100e-6:100e-6:400e-6],sc./[100e-6:100e-6:400e-6],'-o')
hold on
plot(1000*[100e-6:100e-6:400e-6],sub./[100e-6:100e-6:400e-6],'-rs')
AXIS([0.05 .45 0 0.4])
XLABEL('Input power(mW) [ $\lambda$  =635nm]')
YLABEL('Responsivity (mA/mW) ')
hold on
%Figure
SUBPLOT(222)
asd=plot(1000*[100e-6:100e-6:400e-6],1000000*xxx,'-*')
hold on
asdf=plot(1000*[100e-6:100e-6:400e-6],1000000*bbb,'-p')
hold on
asdfg=plot(1000*[100e-6:100e-6:400e-6],1000000*ccc,'-')
hold on
asdfgh=plot(1000*[100e-6:100e-6:400e-6],1000000*sc,'-o')
hold on
asdfghj=plot(1000*[100e-6:100e-6:400e-6],1000000*sub,'-rs')

```

```
AXIS([0.05 .45 0 150])
XLABEL('Input power(mW) [ $\lambda$  =635nm]')
YLABEL('Photogenerated current ( $\mu$ A) ')
hold on
legend([asd,asdf,asdfg,asdfgh,asdfghj], 'R(total)', 'R(base)', 'R(colle  
ctor)', 'R(sub-collector)', 'R(sub)')
grid on
```

Appendix C: Matlab code for Responsivity, Collection efficiency and Quantum efficiency of InP/InGaAs HPT

```
%1550nm
alphaB=.85e4;
alphaC=.68e4;
alphaSC=.68e4;
clc
Lp=30e-4;
B=15;
q=1.6e-19;
lamda=1550e-9;
Eph=6.63e-34*3e8/lamda;
XX=5.3e14;
YY=4.9e14;
ZZ=3.6e14;
magb=(1-exp(-alphaB*.1e-4));
magc=YY/XX*(1-exp(-alphaC*.4e-4));
magsc=ZZ/XX*(1-(exp(-alphaSC*.4e-4)));
aa=1-(exp(-alphaSC*1e-4));
aaa=B*q/Eph;
Rspec1550=B*q/Eph*(magb+magc+magsc)
QE1550=Rspec1550*Eph/q/B
```

```
%1300nm

alphaB=1.55e4;
alphaC=1.16e4;
alphaSC=1.16e4;
Lp=30e-4;
B=15;
q=1.6e-19;
lamda=1300e-9;
Eph=6.63e-34*3e8/lamda;
XX=4.5e14;
YY=3.8e14;
ZZ=2.4e14;
magb=(1-exp(-alphaB*.1e-4));
magc=YY/XX*(1-exp(-alphaC*.4e-4));
magsc=ZZ/XX*(1-(exp(-alphaSC*.4e-4)));
aa=1-(exp(-alphaSC*1e-4));
aaa=B*q/Eph;
Rspec1300=B*q/Eph*(magb+magc+magsc)
QE1300=Rspec1300*Eph/q/B
```

```
%980nm

alphaB=3e4;
alphaC=3e4;
alphaSC=3e4;
Lp=30e-4;
B=15;
q=1.6e-19;
lamda=980e-9;
Eph=6.63e-34*3e8/lamda;
XX=3.2e14;
YY=2.5e14;
ZZ=.75e14;
```



```

magb=(1-exp(-alphaB*.1e-4));
magc=YY/XX*(1-exp(-alphaC*.4e-4));
magsc=ZZ/XX*(1-(exp(-alphaSC*.4e-4)));
aa=1-(exp(-alphaSC*1e-4));
aaa=B*q/Eph;
Rspec980=B*q/Eph*(magb+magc+magsc)
QE980=Rspec980*Eph/q/B

```

%800nm

```

alphaB=6e4;
alphaC=6e4;
alphaSC=6e4;
Lp=30e-4;
B=15;
q=1.6e-19;
lamda=800e-9;
Eph=6.63e-34*3e8/lamda;
XX=2.7e14;
YY=1.5e14;
ZZ=.14e14;
magb=(1-exp(-alphaB*.1e-4));
magc=YY/XX*(1-exp(-alphaC*.4e-4));
magsc=ZZ/XX*(1-(exp(-alphaSC*.4e-4)));
aa=1-(exp(-alphaSC*1e-4));
aaa=B*q/Eph;
Rspec800=B*q/Eph*(magb+magc+magsc)
QE800=Rspec800*Eph/q/B

```

%900nm

```

alphaB=4e4;
alphaC=4e4;
alphaSC=4e4;
Lp=30e-4;
B=15;
q=1.6e-19;
lamda=900e-9;
Eph=6.63e-34*3e8/lamda;
XX=3.1e14;
YY=2.1e14;
ZZ=.42e14;
magb=(1-exp(-alphaB*.1e-4));
magc=YY/XX*(1-exp(-alphaC*.4e-4));
magsc=ZZ/XX*(1-(exp(-alphaSC*.4e-4)));
aa=1-(exp(-alphaSC*1e-4));
aaa=B*q/Eph;
Rspec900=B*q/Eph*(magb+magc+magsc)
QE900=Rspec900*Eph/q/B

```

%1000nm

```

alphaB=3e4;
alphaC=3e4;
alphaSC=3e4;
Lp=30e-4;
B=15;
q=1.6e-19;
lamda=1000e-9;
Eph=6.63e-34*3e8/lamda;
XX=3.4e14;

```

```

YY=2.5e14;
ZZ=.75e14;
magb=(1-exp(-alphaB*.1e-4));
magc=YY/XX*(1-exp(-alphaC*.4e-4));
magsc=ZZ/XX*(1-(exp(-alphaSC*.4e-4)));
aa=1-(exp(-alphaSC*1e-4));
aaa=B*q/Eph;
Rspec1000=B*q/Eph*(magb+magc+magsc)
QE1000=Rspec1000*Eph/q/B

```

%1100nm

```

alphaB=2.3e4;
alphaC=2.3e4;
alphaSC=2.3e4;
Lp=30e-4;
B=15;
q=1.6e-19;
lamda=1100e-9;
Eph=6.63e-34*3e8/lamda;
XX=3.8e14;
YY=3e14;
ZZ=1.2e14;
magb=(1-exp(-alphaB*.1e-4));
magc=YY/XX*(1-exp(-alphaC*.4e-4));
magsc=ZZ/XX*(1-(exp(-alphaSC*.4e-4)));
aa=1-(exp(-alphaSC*1e-4));
aaa=B*q/Eph;
Rspec1100=B*q/Eph*(magb+magc+magsc)
QE1100=Rspec1100*Eph/q/B

```

%1200nm

```

alphaB=2e4;
alphaC=2e4;
alphaSC=2e4;
Lp=30e-4;
B=15;
q=1.6e-19;
lamda=1200e-9;
Eph=6.63e-34*3e8/lamda;
XX=4.1e14;
YY=3.4e14;
ZZ=1.5e14;
magb=(1-exp(-alphaB*.1e-4));
magc=YY/XX*(1-exp(-alphaC*.4e-4));
magsc=ZZ/XX*(1-(exp(-alphaSC*.4e-4)));
aa=1-(exp(-alphaSC*1e-4));
aaa=B*q/Eph;
Rspec1200=B*q/Eph*(magb+magc+magsc)
QE1200=Rspec1200*Eph/q/B

```

%1400nm

```

alphaB=1.1e4;
alphaC=1.1e4;
alphaSC=1.1e4;
Lp=30e-4;
B=15;
q=1.6e-19;
lamda=1400e-9;

```

```

Eph=6.63e-34*3e8/lamda;
XX=4.8e14;
YY=4.3e14;
ZZ=2.8e14;
magb=(1-exp(-alphaB*.1e-4));
magc=YY/XX*(1-exp(-alphaC*.4e-4));
magsc=ZZ/XX*(1-(exp(-alphaSC*.4e-4)));
aa=1-(exp(-alphaSC*1e-4));
aaa=B*q/Eph;
Rspec1400=B*q/Eph*(magb+magc+magsc)
QE1400=Rspec1400*Eph/q/B

```

%1700nm

```

alphaB=.06e4;
alphaC=.06e4;
alphaSC=.06e4;
Lp=30e-4;
B=15;
q=1.6e-19;
lamda=1700e-9;
Eph=6.63e-34*3e8/lamda;
XX=5.9e14;
YY=5.8e14;
ZZ=5.7e14;
magb=(1-exp(-alphaB*.1e-4));
magc=YY/XX*(1-exp(-alphaC*.4e-4));
magsc=ZZ/XX*(1-(exp(-alphaSC*.4e-4)));
aa=1-(exp(-alphaSC*1e-4));
aaa=B*q/Eph;
Rspec1700=B*q/Eph*(magb+magc+magsc)
QE1700=Rspec1700*Eph/q/B

```

Appendix D: Matlab code for Optical characteristics of GaAs based HPT.

```
file = load ('IVcharafor635nm.txt')
Ic1=file(:,2)';
Ic1=Ic1(1:3:length(Ic1));
Ic2=file(:,3)';
Ic2=Ic2(1:3:length(Ic2));
Ic3=file(:,4)';
Ic3=Ic3(1:3:length(Ic3));
Ic4=file(:,5)';
Ic4=Ic4(1:3:length(Ic4));
Ic5=file(:,6)';
Ic5=Ic5(1:3:length(Ic5));
Vc=file(:,1)';
Vc=Vc(1:3:length(Vc));
%.....635nm.....
%SUBPLOT(121)
plot(Vc,1000*Ic1,'-.')%10uW
hold on
asdf=plot(Vc,1000*Ic2,'-.')%50uW
plot(Vc,1000*Ic3,'-.')%100uW
plot(Vc,1000*Ic4,'-.')%150uW
%plot(Vc,1000*Ic5)%200uW
YLABEL('Iphoto (mA) ')
XLABEL('Vce (V)')
%AXIS([0 3 -1 6])
% %.....840nm.....Ib=50uA
file = load ('IVcharafor635nmelec.txt')
Ie1=file(:,2)';
Ve1=file(:,1)';
asd=plot(Ve1,1000*Ie1,'-.')%150uW;
plot(Ve1,1000*Ie1,'-.')%100
plot(Ve1,1000*Ie1,'-.')%50
plot(Ve1,1000*Ie1,'-.')%10
grid on
AXIS([0 3 -.5 2.5])
legend([asdf,asd], 'measured', 'predicted')
%title('(b)  $\lambda=840\text{nm}$ ')
```

Appendix E: Analytical Spectral response for GaAs-based HPT

```

A                = 2.3e4;
phi_b            =[2.51 2.76 3.02 3.27 3.52 3.7 4.024 4.48 4.5];
n                =[4.333 4.06 3.89 3.82 3.77 3.72 3.68 3.634 3.6];
Rf=(n()-1)./(n()+1);
Rf=Rf.^2;

phi_b            =phi_b*1e14.*(1-Rf());
theeta_o         = phi_b./A;
alpha            = 1e4.*[11.1 6.8 4.5 3.45 2.5 1.8 1.4 .56 .021];
w                = .05e-4;
D_p              = 45;%25
Lp               = 2.2e-4;
T_p              = Lp*Lp/D_p;

S2=D_p/T_p;
S1=S2^.5;
S1=[6.3 5.2 4 3 2 1.5 1.3 1.3 1]*3.1e4;
%T_p=2e-9;
w_b              = w;
Pn_o             = 2.2e-7 ;
Pn_at_0          = theeta_o./S1;

x = (theeta_o .*alpha  * T_p)./((alpha* Lp).^2 -1);

res = x.*( sinh(w/Lp)*alpha.*exp(-alpha.*w_b)
+(1/Lp).*cosh(w/Lp).*exp(-alpha.*w) - (1/Lp) )+ ...
Pn_at_0 .* ( (1/Lp).*cosh(w/Lp)*exp(-alpha.*w) - (1/Lp) )+
(1/Lp)*Pn_o;
a = res*1/sinh(w/Lp);
In=-1.6e-19*D_p*a*A;
% grid on
% plot(450:50:850,x)
% Figure
% plot(450:50:850,res)
% Figure
% plot(450:50:850,a)
% Figure
% plot(450:50:850,In)
% % plot (In, '-')
% % hold on
% % grid on
% Figure
% %Iph
Ac                = 2.3e-3;
phi_cc            =[2.51 2.76 3.02 3.27 3.52 3.77 4.024 4.28 4.5];
w_b              = .09e-4;
alpha            = 1e4.*[8.1 6 4 3 2 1.6 1.2 1.1 .07];
phi_c             =phi_cc.*.63e14.*exp(-w_b*alpha);
theeta_o          = phi_c./Ac;
wc                =.5e-4;
Iph=1.6e-19*phi_c.*(1-exp(-alpha*wc));

% Ip

```

```

A          =2.3e-3;
theeta_o   = phi_c.*exp(-wc*alpha);
alpha      = 0.02e4;
w          = 1e-4;
D_p        = 4;
Lp         = 1.2e-4; %*3;
T_p        = Lp*Lp/D_p;
w_b        = w;
Pn_o       = 8.82e-7 ;
Pn_at_0    = theeta_o/S1;
A          =2.3e-3;
x = (theeta_o .* alpha * T_p)./((alpha* Lp).^2 -1);

res = x.*( sinh(w/Lp)*alpha.*exp(-alpha.*w_b) +
(1/Lp).*cosh(w/Lp).*exp(-alpha.*w) - (1/Lp) )+...
Pn_at_0 .* ( (1/Lp).*cosh(w/Lp)*exp(-alpha.*w) - (1/Lp) )+
(1/Lp)*Pn_o;
a = res*1/sinh(w/Lp);
Ip=1.6e-19*D_p*a*A;
It=Ip+In+Iph;
R=It./((1-Rf()).*100e-6)

%R

xx=abs (R);
plot(500:50:900,xx, ' -* ' )
hold on

```

Appendix F: Analytical Spectral response for InP/InGaAs HPT

```

A = 1.5e-3;
% starting with 800nm 900 980 1100 1200 1310 1400 1550 1700
phi_b = 1e14*[2.7 3.1 3.4 3.8 4.1 4.5 4.8 5.3 5.9];
n = [3.7 3.7 3.65 3.65 3.6 3.6 3.6 3.6 3.5];
Rf=(n()-1)./(n()+1);
Rf=Rf.^2;
theeta_o = phi_b./A;
alpha = 1e4.*[6 4 3 2.3 2 1.5 1.2 .9 .051]%chck at 850
w = .1e-4;
D_p = 36.25;%for electron
Lp = .45e-4;% calculating from 4e-11s lifetime
T_p = Lp*Lp/D_p;
%T_p=2e-9;
S2=D_p/T_p
S1=.5*S2^.5
S1=[4 3 2 1.8 1.6 1.4 1.2 1.1 1]*3.2e4;
w_b = w;
Pn_o = 2.2e4 ;
Pn_at_0 = theeta_o./S1;

x = (theeta_o .*alpha * T_p)./((alpha* Lp).^2 -1);

res = x.*( sinh(w/Lp)*alpha.*exp(-alpha.*w_b)
+(1/Lp).*cosh(w/Lp).*exp(-alpha.*w) - (1/Lp) )+ ...
Pn_at_0 .* ( (1/Lp).*cosh(w/Lp)*exp(-alpha.*w) - (1/Lp) )+
(1/Lp)*Pn_o;
a = res*1/sinh(w/Lp);
In=-1.6e-19*D_p*a*A
% grid on
% %Iph
Ac = 1.5e-3;
phi_cc = [1.5 2.1 2.5 3 3.4 3.8 4.3 4.9 5.8 ];
alpha = 1e4.*[6 4 3 2.3 2 1.5 1.1 .75 .05];
phi_c =phi_cc.*1e14.*exp(-w_b*alpha);
theeta_o = phi_c./Ac;
wc = .4e-4;
Iph=1.6e-19*phi_c.*(1-exp(-alpha*wc));

% Ip
A = 2.3e-3;
alpha = 1e4.*[6 4 3 2.3 2 1.5 1.1 .75 .05];
phi_c =1e14* [.14 .42 .75 1.2 1.5 2.4 2.8 3.6 5.7];
theeta_o = phi_c./A
alpha = 1e4.*[6 4 3 2.3 2 1.5 1.1 .75 .05];
w = .4e-4;
D_p = 2;
Lp = 8.9e-5;%*3;
T_p = Lp*Lp/D_p;
w_b = w;
Pn_o = 8.82e-7 ;
Pn_at_0 = theeta_o./S1;
A = 1.5e-3;
x = (theeta_o .* alpha * T_p)./((alpha* Lp).^2 -1);

```

```

res = x.*( sinh(w/Lp)*alpha.*exp(-alpha.*w_b) +
(1/Lp).*cosh(w/Lp).*exp(-alpha.*w) - (1/Lp) )+...
Pn_at_0 .* ( (1/Lp).*cosh(w/Lp)*exp(-alpha.*w) - (1/Lp) )+
(1/Lp)*Pn_o;
a = res*1/sinh(w/Lp);
Ip=-1.6e-19*D_p*a*A;
It=Ip+In+Iph;
R=It./((1-Rf()).*100e-6)
xx=abs (R);
plot([800 900 980 1100 1200 1310 1400 1550 1700],xx, 'b*')

```


Appendix G: Absorption coefficient and monolayer detection calculations of GaAs and InP materials

```
%GaAs
mo=9.11e-31;
mn=0.067*mo;
c=3e8;
lamda= [200e-9:10e-9:874e-9];
h=6.626068e-34;

a=3*(mn/mo)^1.5;
a1=a*lamda.*( (c*h./lamda - 1.42*1.6e-19).^0.5 )/(h*2*3.142*c)
plot(lamda,a1)
semilogy(lamda, a1)

hold on

%InP
mo=9.11e-31;
mn=0.041*mo;
c=3e8;
lamda= [200e-9:10e-9:1650e-9];
h=6.626068e-34;

a=3*(mn/mo)^1.5;
a1=a*lamda.*( (c*h./lamda - .74*1.6e-19).^0.5 )/(h*2*3.142*c)
semilogy(lamda, a1)

% monolayer detection
% function [inp,gas]=spectral(a,b)
hold on
plot(875,.022, 's')
plot(835,.004, 's')
plot(900,.034, 's')

a=3e-6%1e-6;
b=13e-6;

file = load ('data.txt')
E=file(:,1)';
K=file(:,3)';
n=file(:,2)';

lamda=1.240e-6./E;
alpha=4*pi*K./lamda;
Rf=(n-1)./(n+1);
flux=(1-Rf).*( exp(-1*a*alpha) - exp(-1*b*alpha) );
inp=plot(1e9*lamda,flux,'*-');
AXIS([750 1200 0 0.25])
hold on
%plot(lamda,n)
%.....
file = load ('gaas.txt')
E=file(:,1)';
K=file(:,3)';
n=file(:,2)';
```

```

lamda=1.240e-6./E;
alpha=4*pi*K./lamda;
Rf=(n-1)./(n+1);
flux=(1-Rf).*( exp(-1*a*alpha) - exp(-1*b*alpha) );
gas=plot(1e9*lamda,flux,'--rs')
YLABEL('FRACTION OF FLUX ABSORBED ')
XLABEL('Wavelength (nm)')

%plot(lamda,alpha)
hold on
%plot(lamda,n)
legend([inp,gas], 'InP', 'GaAs')
grid on

```